

OPTICAL DIPOLE TRAPPING, NARROW-LINE COOLING, AND  
SINGLE ATOM OBSERVATION OF HOLMIUM ATOMS

by

Christopher Yip

A dissertation submitted in partial fulfillment of  
the requirements for the degree of

Doctor of Philosophy

(Physics)

at the

UNIVERSITY OF WISCONSIN-MADISON

2021

Date of final oral examination: 01/20/2021

The dissertation is approved by the following members of the Final Oral Committee:

Mark Saffman, Professor, Physics

Thad Walker, Professor, Physics

James Lawler, Professor, Physics

Randall Goldsmith, Professor, Chemistry

© Copyright by Christopher Yip 2021  
All Rights Reserved

To my family.

## ACKNOWLEDGMENTS

If I were to thank everyone who has given me any form of support, be it physical and psychological health, or financial support, or even just general life advice, this section would probably be as long as my actual dissertation. I will try my best to keep it relatively brief.

Of course, the very first person I need to thank is my advisor, Dr. Mark Saffman. He has given me tons of advice over the years and has made sure to keep me pointed in the right direction for my research. Holmium has been an amazing experiment to work on, as it has kept me challenged and taught me so many things over the course of my Ph.D.

There is no way I could have ever reached this point in my education without everything my parents have done for me. They have continually supported me throughout my entire life, even considering that I have taken an entirely different career path than my more business-oriented brothers. Not once have I ever felt coerced towards certain fields in my education by them, and that is something for which I am extremely grateful.

I cannot have done any of this without all my predecessors on the Holmium experiment. Jinlu Miao laid out the foundation of the whole experiment, which set the ball rolling on a lot of interesting scientific questions. James Hostetter and Donald Booth taught me all I needed to know to about working in an AMO lab, from simpler skills such as cleaning optics, to more complex tasks like producing cold clouds of holmium atoms, and everything in between. I am also very thankful for all of the help from Will Milner and Huaxia Zhou have given through concurrent work on different parts of the experiment during their undergraduate senior thesis work.

I have so many other people to thank in the Saffman Lab as well, and while everyone in the group has contributed to my improvement as a researcher over the years, a few people have been particularly helpful to me. Laura Fleming patiently worked with me on all the idiosyncrasies on our equipment, and helped me improve in many skills crucial to AMO research which do not involve optics. Josh Isaacs and Trent Graham have given me lots of practical advice on how to work with general AMO equipment over the years, including some instances of pointing out how I may be having trouble because the previous set up

had a few problems of which I was entirely unaware. Juan Bohorquez and Cody Poole have always been around to lend me a helping hand (many times literally) on my research, as well as offering the occasional thought-provoking discussion about how our research fits into the broader picture of scientific knowledge.

My physics professors in my undergraduate studies did wonders in nurturing a growing interest in the world of physics, and they were ultimately who led me to consider graduate school. Dr. Daniel Sheehan's style of teaching, where he heavily emphasized back-of-the-envelope calculations and entirely forbade the use of calculators in class made me realize just how versatile physics knowledge can be even in everyday life. And my undergraduate advisor Dr. Greg Severn was always around and willing to discuss even the silliest of questions I had about physics, connections between free will and quantum mechanics, or even just general life advice.

I have numerous stories and experiences I am thankful for with all my friends I have made in Madison over the years, from the first few months when we were all struggling to get our bearings, to the occasional camping trip that served as a sanity break from the stresses of research. Being able to spend time with people who share similar academic interests as me and are at the same stage of life has really made me a better person overall.

And lastly, I want to thank the online incremental games community. My involvement in that area has helped me find many others who have been able to support and console me on certain issues which I did not feel comfortable discussing with close family and friends. I made many friends online who have helped me remain sane throughout the course of my Ph.D by filling in those final gaps I needed for positive mental health, especially in a pandemic where going outside to meet people is not an option. They all helped me remain grounded by reminding me that progress towards a goal is gradual, and it is only upon looking back over long periods that we realize that how far we have come through consistent effort and because we stand on the shoulders of giants.

# TABLE OF CONTENTS

	Page
<b>LIST OF TABLES . . . . .</b>	<b>vi</b>
<b>LIST OF FIGURES . . . . .</b>	<b>viii</b>
<b>Abstract . . . . .</b>	<b>xvi</b>
<b>1 Introduction . . . . .</b>	<b>1</b>
1.1 Quantum Computing Overview . . . . .	1
1.2 Quantum Computing with Neutral Atoms . . . . .	2
1.3 Ensemble Quantum Computing . . . . .	3
1.3.1 Encoding schemes . . . . .	3
1.3.2 Advantages of Ensemble Encoding . . . . .	6
1.3.3 Disadvantages of Ensemble Encoding . . . . .	8
1.4 Holmium . . . . .	9
<b>2 Experiment Setup . . . . .</b>	<b>13</b>
2.1 Holmium Source . . . . .	13
2.2 Chiller System . . . . .	15
2.3 Trapping Region . . . . .	16
2.4 Laser Systems . . . . .	17
2.4.1 410.5 nm Ti:Sa . . . . .	17
2.4.2 412 nm Breadboard Setup . . . . .	19
2.4.3 532 nm ODT Diode Laser . . . . .	20
2.5 Reference Cavities . . . . .	21
2.5.1 ULE Cavity . . . . .	21
2.5.2 Quantaser Etalon . . . . .	22
2.6 Imaging setup . . . . .	23
2.7 Control System . . . . .	25
2.8 Conclusion . . . . .	26
<b>3 Holmium Dipole Trap . . . . .</b>	<b>27</b>
3.1 Broad-line Magneto-Optical Trap . . . . .	27
3.2 Trap Loading . . . . .	28

3.3	532 nm Trap . . . . .	28
3.3.1	Atomic Polarizability . . . . .	29
3.3.2	Calculating Holmium's Polarizability . . . . .	32
3.3.3	Trap Depth . . . . .	33
3.3.4	Photon Scattering Rate . . . . .	35
3.4	AC Stark Shift . . . . .	36
3.5	Trap Frequency Measurements . . . . .	40
3.5.1	FORT Trap Frequency . . . . .	40
3.5.2	Parametric Heating Model . . . . .	41
3.5.3	Radial and Longitudinal Trap Frequencies . . . . .	44
3.5.4	Tensor Shift Effects . . . . .	44
3.6	Atom Loss Mechanisms . . . . .	45
3.6.1	Atom Temperature . . . . .	45
3.6.2	Dependence on Trap Power . . . . .	46
3.7	Conclusion . . . . .	49
<b>4</b>	<b>Narrow Line Transition . . . . .</b>	<b>50</b>
4.1	Hyperfine Structure . . . . .	51
4.1.1	Mathematical model . . . . .	51
4.1.2	Constructing an analytic function to fit . . . . .	53
4.2	Saturated Absorption Spectroscopy . . . . .	54
4.3	Fitting Hyperfine Constants . . . . .	56
4.4	Narrow-line Cooling . . . . .	60
4.4.1	Advantages . . . . .	60
4.4.2	Disadvantages . . . . .	61
4.4.3	Two-stage Cooling . . . . .	63
4.5	Conclusion . . . . .	63
<b>5</b>	<b>Single Atom Imaging . . . . .</b>	<b>64</b>
5.1	Introduction . . . . .	64
5.2	Photon Scattering Rate . . . . .	65
5.3	Experimental Factors . . . . .	65
5.4	Camera Noise Statistics . . . . .	67
5.4.1	Dark Current . . . . .	67
5.4.2	Read Noise . . . . .	67
5.4.3	Non-Ideal Gain Characteristics . . . . .	68
5.4.4	CCD Active Bias . . . . .	70
5.4.5	External Noise Factors . . . . .	70
5.4.6	Overall Signal-to-Noise Ratio . . . . .	73
5.5	Measurement Process . . . . .	73
5.6	Ideal Histograms . . . . .	75

5.7	Single Atom Attempts for Holmium . . . . .	76
5.8	Explanation for low SNR on single atom signal . . . . .	77
5.8.1	Imaging Loss . . . . .	77
5.8.2	Optical Setup . . . . .	78
5.8.3	Experimental Issues . . . . .	79
5.9	Conclusion . . . . .	80
<b>6</b>	<b>Magnetic Trapping</b> . . . . .	81
6.1	Magnetic Moment of Holmium . . . . .	81
6.2	Magnetic Trapping . . . . .	82
6.3	Trapping in a Quadrupole Gradient . . . . .	84
6.3.1	MOT Coil Configuration . . . . .	85
6.4	Magnetic Trap Lifetime . . . . .	85
6.5	Magnetic Trap Array . . . . .	86
6.5.1	Wire Material . . . . .	88
6.5.2	Potential Energy Structure . . . . .	89
6.5.3	Disadvantages . . . . .	90
6.6	Conclusion . . . . .	91
<b>7</b>	<b>Future Directions</b> . . . . .	92
7.1	Magnetic State Dressing . . . . .	92
7.1.1	Magic Field Conditions . . . . .	92
7.1.2	Approximation from Floquet Theory . . . . .	95
7.1.3	State Dressing Results . . . . .	97
7.2	Qudits . . . . .	98
7.3	Conclusion . . . . .	100
<b>8</b>	<b>Concluding Statements</b> . . . . .	101
<b>REFERENCES</b>	. . . . .	106
<b>APPENDIX</b>		
<b>A</b>	<b>Aligning optics for combined trapping and imaging</b> . . . . .	107
<b>B</b>	<b>Locking to a ULE Sideband</b> . . . . .	109
<b>C</b>	<b>Atom Temperature Measurements</b> . . . . .	111
<b>D</b>	<b>Narrow-line Frequency References</b> . . . . .	114

# LIST OF TABLES

1.1	Atomic properties of the ground state of all the rare earths which have been trapped in a MOT. Holmium has the advantage of having a single isotope as well as the largest number of available hyperfine states. . . . .	10
3.1	Polarizability and photon scattering rate for optical dipole traps at our three candidate wavelengths. Note that the values for 445 nm may be inaccurate due to a transition of unknown linewidth at 444.9 nm. Scattering rates were calculated using figures from our current trap - 640 mW power and 4.6 micron spot radius. . . . .	29
3.2	Table of fitted values for loss coefficients in the loss models we considered. . . . .	49
4.1	Measured and fitted frequencies for the different hyperfine transitions on the 412 nm line. Linewidths were fitted by closely measuring each peak individually, and thus deviate slightly from the expected ratios based on matrix elements. . . . .	60
5.1	Dark counts per second for various analog gain settings. EM gain also linearly amplifies noise from dark current, so the maximum expected dark count rate can be as high as a factor of 1000 larger. . . . .	67
5.2	Noise electron counts for the Hamamatsu C9100-13 camera at various readout speeds. Reading the images out slower vastly decreases the spurious electrons generated from CIC noise. . . . .	68

5.3	Data showing the noise contributions from the lasers and atoms in various conditions for the ProEM camera. To take these measurements, the atoms were controlled via the gate valve in the vacuum chamber and the laser beams were controlled by a beam block farther upstream so no leakage from the AOMs would reach the camera. These were taken with a 4.5 ms exposure time. . . . .	71
5.4	Noise counts from the Hamamatsu C9100-13 camera, taken with the same conditions as in Figure 5.3. The read noise is generally higher, likely lending to a difference in the internal camera electronics, but the gain characteristics of the Hamatsu were generally more stable than the ProEM 512 over longer time spans. The higher variance in counts shows up primarily in the exponential tail of CIC noise. . . . .	72
6.1	Magnetic moments for the ground states of select atoms used in various atomic physics experiments. . . . .	82
7.1	List of magic magnetic field conditions for states connected by single-photon transitions, up to 1500 Gauss. The sensitivity of the states at the magic field condition is also noted. . . . .	94

# LIST OF FIGURES

1.1	Energy levels of two-atom Rydberg states as a function of their separation distance, showing the distance dependence of the dipolar interactions leading to the Rydberg blockade effect. . . . .	3
1.2	Three different methods for encoding the state $ 01\dots001\rangle$ within a K-state quantum system. a) A relatively standard array of single qubits. b) With Fock states in a single ensemble. c) With pairs of states within an ensemble to give better resilience to error. Reproduced from [15]. . . . .	4
1.3	Single and two-qubit gates for collective encoding schemes. a) Rotations between $ 0_i\rangle$ and $ 1_i\rangle$ can be mediated through a Rydberg state. b) A controlled-phase gate mediated by a Rydberg blockade, similarly to single-atom qubits. Reproduced from [15]. . . . .	5
1.4	One possible way of pairing holmium's 128 hyperfine states in a way that produces 60 easily accessible qubits within a single ensemble. . . . .	6
1.5	Grotian diagram showing other easily-accessible fine structure states from the ground state using visible light. . . . .	11
2.1	Velocity distribution of holmium atoms out of the oven, with and without the slowing beam present, for the experimental parameters on our experiment. This particular histogram was generated for slowing with $I/I_{sat} = 10$ and a detuning of -440 MHz, with $10^5$ trials. . . . .	15

2.2	Physical layout of the vacuum system where we produce the optical dipole trap. Reproduced from [34], but is however slightly outdated as our MOT coils have since been removed and installed inside the chamber. . . . .	16
2.3	Usage of all the ports of the spherical octagon for the trapping region. The slower beam and its opposite port are in-vacuum paths, while the rest are transparent viewports. . . . .	17
2.4	Images of the experimental setup of the trapping region, showing the in-vacuum MOT coils (left). Also shown is the periscope for the slower beam and the Andor camera pointed downward into the chamber (right). . . . .	18
2.5	Laser Setup for generating 410.5 nm light . . . . .	19
2.6	Example of frequency shifts made by the AOMs in our setup, in order to generate light at the requisite frequencies relative to the MOT transition . . . . .	20
2.7	Schematic of the home-built setup used for generating 412 nm light. Details of the locking setup are not included here as we have used different reference cavities for different situations. The optical isolators are required to prevent backreflections from causing undesired feedback to the ECDL and TA. . . . .	21
2.8	Image of the Quantaser Etalon inside of its temperature-controlled enclosure (tempo- rarily opened for this image). The steel enclosure is connected to its mounting posts via nylon screws with an O-ring as a spacer in order to keep it mechanically stable but thermally isolated from the optical table. This part of the experimental setup is also inside of a large plexiglass box which was intended to block excess scatter resulting from the optics described in section 2.4.1, incidentally providing another layer of thermal stability. . . . .	22
2.9	Optical path for combined trapping and imaging. The location of the EMCCD camera in the diagram is reserved for either the Princeton Instruments ProEM 512+ or the Hamamatsu C9100-13. The NA of the collection lens is 0.202. . . . .	24

2.10 Picture of the cage rod-mounted optics for the combined trap and image setup, with the shroud pulled back. The main purpose of the shroud is to block excess scatter from the trapping light; in Chapter 5 we note that noise from background light sources is negligible. . . . .	24
2.11 Image of the US Air Force resolution chart as imaged on the ProEM 512 (left) and Hamamatsu C9100-13 (right) cameras. . . . .	25
2.12 Inset image of the smallest resolvable elements on the USAF resolution chart, using the ProEM 512 camera. The slots indicated in this figure range in width from $3.90\mu m$ to $2.19\mu m$ wide. . . . .	26
3.1 Pulse diagram of the experimental sequence we used to load our FORT. . . . .	28
3.2 Plot of holmium's polarizability over most of the visible light range. The total polarizability farther away from transitions is primarily determined by the scalar and tensor components. . . . .	34
3.3 Atomic polarizability of holmium near 445 nm, 532 nm, and 1064 nm. Each set plot is a family of curves corresponding to the polarizability of each separate $m_F$ state within the $F = 11$ states. All of these states have slightly different polarizabilities in general due to a nonzero $\alpha_2$ . . . . .	35
3.4 Scattering rates of light at 445 nm, 532 nm, and 1064 nm. The difference in magnitude between the different wavelengths compared to their respective differences in polarizability comes from the $1/\Delta^2$ dependence. Calculated using a 640 mW beam with a 4.6 micron focus. . . . .	36
3.5 False-color image of the "hole" in the MOT caused by the trapping beam. . . . .	37
3.6 Scaling of the AC Stark shift as a function of the trap beam power. The solid line is not a linear fit to the data, but rather an expected trend based on the calculated polarizability and treating the transition as an ideal two-level system. . . . .	39

3.7	Measured power of the MOT (blue) and FORT (red) beams from pick-off photodiodes during the chopping sequence. The finite rise time of the switching AOMs limits how quickly we can chop the beams. . . . .	40
3.8	Plots showing results of our simulations for our square-wave trap modulation. Blue cells correspond to the atom staying in the trap, and red cells correspond to atoms being lost from the trap after the modulation. Atoms appear to be lost more readily at modulation frequencies which are less than the theoretical factor of 2 larger than the trap frequency. . . . .	43
3.9	Atom loss from the trap when modulated at various frequencies, with an overlay of calculated trap frequencies for separate $m_F$ levels in the $F = 11$ set of states. . . .	45
3.10	Trap population decay over time for various trap powers. The shallower, low-power traps start out with less atoms, but the atoms have a longer decay time. . . . .	46
3.11	Trap population decay over time for various trap powers after some experimental improvements. . . . .	47
3.12	Loss curves from the dipole trap with different trap power settings. The blue curves are a single-body loss model which is a simple exponential decay, while the red curve is the two-body loss model. The data indicate that the two-body loss seems to be higher at lower power. . . . .	49
4.1	Energy gaps between successive hyperfine states (left) for the ground state and excited states for the 412 nm line. The relative gaps between states based on a set of $F \rightarrow F' = F + 1$ transitions is also shown (right), showing the nontrivial mapping between the order of the spectroscopy peaks and the hyperfine states. The ground state values were calculated from previous literature [54] while the excited state values are our measurements. . . . .	51
4.2	Schematic of the optical setup we used for measuring the 412 nm spectrum. . . .	55

4.3	Sample data set where we indicate the peak indexing for our data table containing measured transition frequencies. The blue trace is the raw data from a single sweep, and the orange trace is an average of 13 separate sweeps after some data filtering which rejects scans with signs of clear laser instability. . . . .	57
4.4	Plot of an average of a few hundred scans of the spectrum (black), with measured reference frequencies (blue) overlaid. The nonlinear relationship between the voltage sent to the laser and the actual frequency results in the blue lines not coinciding with where the black peaks are. The red curve is a theoretically calculated spectrum based on the fit to the blue frequencies, which we expect are more free of systematic errors than the black trace. This figure also shows that the predicted heights based on relative matrix elements are approximately correct as well. . . . .	58
4.5	Value of the least-squares error metric near the fitted hyperfine constants. The cited errors are the values of the hyperfine constants at which the error increases to quadruple of its minimal value. . . . .	61
4.6	Energy level diagram examining potential self-repumping on the broad and narrow transitions, not necessarily to scale. The narrow transition is only half as far away from resonance in terms of absolute frequency, but is seven times farther away in terms of linewidths. . . . .	62
5.1	A sample of a few images taken from the camera with the shutter closed, so no ambient light reaches the CCD. With ideal readout these images would all be identical and uniform, but what we are left with is any additional measurement artifacts related to the readout electronics. The random brighter pixels are due to CIC noise, while the nonuniform background color comes from other sources of readout noise.	69
5.2	A histogram generated from all the pixel values read out over a few thousand distinct images. As the extent of the noise is only apparent on a logarithmic scale, this is only an issue for very weak signals. . . . .	69

5.3	Plot of the expected signal-to-noise ratio for single atom measurements, given our noise model and measurements. The optimal exposure time for our setup is 1 ms in order to maximize our SNR. If the trap is spread across too many pixels, the SNR is marginal at best and may result in the single atom signal not being seen. . . . .	74
5.4	Two theoretical histograms of single atom data, based on our noise model. The left plot is with a mean atom count of 0.4 and SNR of 4, leading to several spatially well-separated peaks. The right plot has a mean atom count of 1.2 and SNR of 2, showing the Poissonian shape of the relative peak heights and the poorer peak separation. . . . .	76
5.5	An image of the trap (left) and a histogram (right) generated by summing the counts in the black box indicated on the trap image. The red curve is a fitted theoretical single atom signal. This data consists of 5000 separate frames. . . . .	77
5.6	Images and plots of the measured beam widths of our trap beam, fitted to the principal axes of the beam. The fitted waists are 4.11 and 4.14 microns, with the focal planes of the two axes being 6.0 microns apart. . . . .	79
6.1	Diagram showing magnetically trappable states for Rb, Cs, and Ho. Due to the placement of the states, the alkalis require multiple photons to transition between trappable states. . . . .	83
6.2	Image of the in-vacuum MOT coils . . . . .	84
6.3	Potential energy structure near the center of the MOT coils, compared to our current optical dipole trap. Note the difference in both scales, which is significant enough that they cannot be meaningfully plot together on the same set of axes. . .	86
6.4	Old data of magnetic trapping of holmium within the quadrupole gradient field from the MOT coils. The population falls quickly and then loads from the dark magnetically-trapped states. . . . .	87
6.5	Layout for a unit cell of the magnetic trap array . . . . .	87
6.6	View of the overall structure of the magnetic trap array . . . . .	88

6.7	Two equipotentials for the magnetic trapping potential, one at one tenth of the total trap depth (right) and one of the highest energy which remains trapped, showing shape distortion when examining a larger scale. Note the factor of ten difference in the length scales. . . . .	90
7.1	Image showing the location of nonzero elements in the Zeeman Hamiltonian. The elements are very sparse, allowing the usage of more efficient sparse matrix diagonalization methods. This sparseness property still holds true for the Floquet matrix as well. . . . .	93
7.2	Block matrix structure of the Floquet matrix to diagonalize. <b>H</b> represents the 128x128 matrix for the hyperfine and Zeeman interactions and <b>C</b> represents the off-diagonal microwave coupling Hamiltonian (Equation 7.1) but without the time dependent $\cos(\omega t)$ . . . . .	97
7.3	Some states within holmium's ground state which have the indicated magic field conditions between them when a dressing field detuned 30 MHz from the $F = 6$ to 7 gap is applied. . . . .	98
7.4	Magnetic field sensitivities for states in one of the sets shown in 7.3. $ 6, 4\rangle$ and $ 7, 4\rangle$ have an avoided crossing which causes the presence of the magic conditions in the first place, but the avoided crossing means these magic conditions are not useful for quantum information. . . . .	99
7.5	7-state qudit within holmium's hyperfine states, showing the positioning of the states (red) with arrows (blue) showing transitions which could be used for state dressing in a way that lets us independently tune out each state's magnetic sensitivity.	99
B.1	Schematic for the RF electronics we used for the ULE sideband lock . . . . .	110

C.1	Sample data for a MOT temperature measurement, showing images of the MOT expanding over time and curves corresponding to fitted widths on the two different horizontal axes. This particular dataset corresponds to a kinetic temperature of roughly $230 \mu K$ . In our experiment these values are typically approximately the same, although in other rare earths the temperature has sometimes been observed to be highly anisotropic [25]. . . . .	112
C.2	MOT expansion and drop-recapture population curves as a function of the scaled time $\tilde{t} = t/\sqrt{mw_0^2/(4k_B T)}$ . The MOT width during free expansion asymptotically approaches a linear time-dependence, but the recapture curve does not have simple asymptotic behavior. . . . .	113
D.1	Sample data demonstrating how data sets are combined together. The two data sets with error bars are the saturated absorption transmission peaks for the two nearly-degenerate peaks taken under identical conditions. Each individual data set consisted of approximately 50000 raw data points; the error bars indicate the standard deviation of sets of 500 consecutive points being binned together. The sharper peaks are the transmission peaks of the ULE cavity. The two data sets were taken with the ULE sideband tuned to 355 MHz and 360 MHz, which allows the horizontal axis to be properly scaled for the spectroscopy data. . . . .	115

# Abstract

## Optical Dipole Trapping, Narrow-Line Cooling, and Single Atom observation of Holmium Atoms

*Christopher Yip*

*Under the supervision of Professor Mark Saffman*

*At the University of Wisconsin - Madison*

This thesis focuses on progress towards using ensembles of neutral holmium atoms for use in quantum information. The Rydberg blockade, a switchable interaction between neutral atoms, would allow quantum gates to be implemented in these collective ensemble qubits. Holmium is particularly suited for this approach as it has 128 ground hyperfine states, the most out of any stable neutral atom. Holmium is a rare earth element which is largely unstudied and presents many experimental challenges owing to its complicated electron structure, short wavelength transitions, and very low vapor pressure at room temperature.

We show progress towards overcoming some of these challenges. We produced the first holmium dipole trap and made progress towards detecting single holmium atoms within our dipole trap. Additionally, we provide precise measurements of another transition to be used for narrow-line cooling in a two-stage MOT. We then examine many theoretical aspects of future work, such as magnetically trapping holmium in an array of magnetic traps and using microwave fields to reduce the magnetic sensitivity of the hyperfine states. This thesis gives many potential future directions for work on holmium to continue towards.

# Chapter One

## Introduction

### 1.1 Quantum Computing Overview

Computers are the backbone of modern society, as many of the operations of the modern world rely on the ubiquity of computing power. As the world's technology improves, the requirements for processing power also steadily increase. This is reflected in Moore's Law, which is the empirical observation that transistor density on chips doubles roughly every two years. However, the exponential growth from Moore's Law has been slowing down gradually over the last decade. As of 2020, transistor size has reached 7 nm - small enough that quantum-mechanical effects start to interfere with their typical operation. To that end, quantum computing is a paradigm shift for computing which will allow for massive speedups in certain applications.

In a classical computer the fundamental unit of information is the bit, which is simply the on or off state of a transistor and can be described by a 0 or 1. However, in a quantum computer the fundamental unit of information is the qubit. Qubits are different from classical bits since they are not limited to just two states. Instead, qubits can be in a superposition state of both  $|0\rangle$  and  $|1\rangle$ , characterized by an amplitude and relative phase.

When multiple qubits are used together in the same system, the whole system then is also in a superposition of multiple states as opposed to a classical computer being limited to only one state. This results in a potentially exponential speedup for how quickly the information space can be explored and how quickly the desired solution can be found, provided some mathematical cleverness is employed. Some examples which have been theorized and

then experimentally realized are Grover's quantum search algorithm and Shor's prime factorization algorithm. Quantum computers also show promise in effectively modeling other quantum systems as a quantum simulator - something which becomes infeasible for classical supercomputers at only tens of quantum particles.

Since a qubit is simply just a two-level system governed by the laws of quantum mechanics, there are numerous candidates for possible implementations [1]. For the past twenty years, steady experimental progress has been made in various approaches for physical implementations of qubits using photons [2], ions [3], quantum dot spins [4], superconductors [5], nitrogen-vacancy centers in diamond [6], and neutral atoms [7]. As all of these approaches have benefits and drawbacks, research has also gone toward hybrid systems which attempt to combine different systems in order to mitigate the drawbacks [8].

## 1.2 Quantum Computing with Neutral Atoms

The goal for the work in this thesis is to make progress towards manipulating qubit states within neutral holmium atoms. Neutral atoms have a highly switchable interaction strength [7] which allows strong interactions when desired for gate operations and very weak interactions with each other or the environment otherwise. This interaction is controlled via a process called a Rydberg blockade. By exciting a single atom into a Rydberg state, the excited atom causes very strong dipolar interactions with the nearby atoms. The interaction, in turn, causes the same Rydberg state to be Stark-shifted for all nearby atoms within a certain radius. This radius is called the blockade radius, and it effectively prevents more than one Rydberg atom from existing within a certain volume without requiring a change in the energy of the excitation laser. The Rydberg blockade allows for quantum gates between neutral atom qubits [9].

Progress on quantum information with neutral atoms using the Rydberg blockade has been demonstrated with alkali atoms. Fast phase gates have been demonstrated [10] as well as the two-qubit controlled-Z and controlled-NOT gates [11] [12], which together form a universal gate set. So far these experiments have been primarily on alkali atoms due to their simpler electronic structure, using the approach of a 2D [13] or 3D [14] array of single-atom

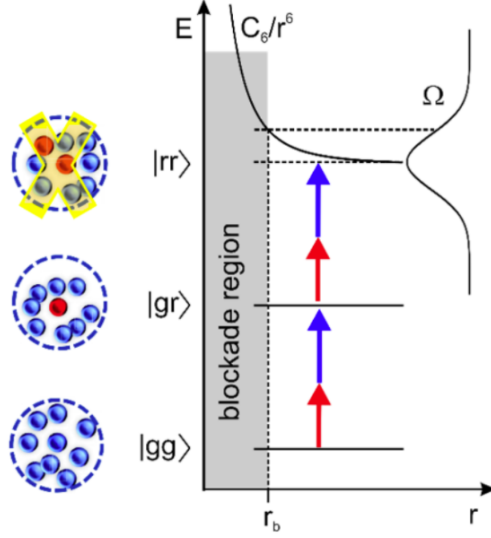


**Figure 1.1** Energy levels of two-atom Rydberg states as a function of their separation distance, showing the distance dependence of the dipolar interactions leading to the Rydberg blockade effect.

qubits. The qubit states chosen for the arrays are the  $m_F = 0$  clock states in order to be magnetically insensitive. Qubit operations are then carried out by spatially selecting out certain array sites with laser pulses.

## 1.3 Ensemble Quantum Computing

### 1.3.1 Encoding schemes

Collective encoding is a different approach to quantum information which has its own advantages and disadvantages compared to single-atom neutral qubits [15]. Holmium has atomic properties which make it particularly suitable to this framework over other more commonly-used elements, which will be discussed in more detail in the next section.

Ensemble quantum computing works by having a qubit's state be distributed amongst an entire atomic ensemble as opposed to being tied to the state of a single atom. This is different from most other methods of qubit encoding, as typically different qubits are encoded in distinct and often spatially-separated two-level systems. As the name suggests,

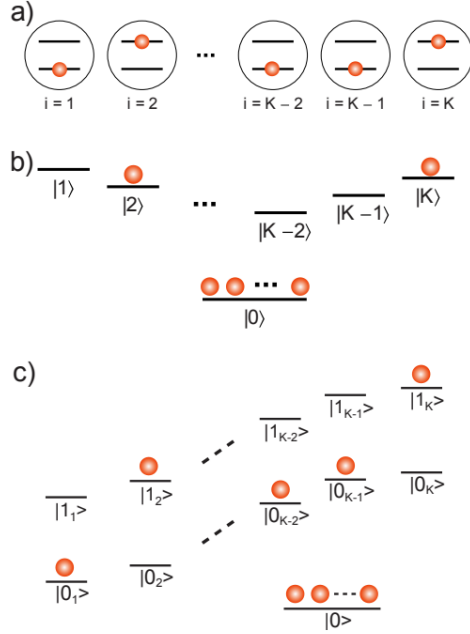


**Figure 1.2** Three different methods for encoding the state  $|01\dots001\rangle$  within a  $K$ -state quantum system. a) A relatively standard array of single qubits. b) With Fock states in a single ensemble. c) With pairs of states within an ensemble to give better resilience to error. Reproduced from [15].

with ensemble encoding multiple qubits can occupy the same physical space within the same atomic ensemble. There are two ways this can be done, as outlined in [15] and shown in Figure 1.2, and both involve defining qubits based on the occupancy of hyperfine states.

The first method is to designate each individual hyperfine state to be a single qubit, which is  $|0\rangle$  or  $|1\rangle$  based on the presence or absence of an atom in that state. Since all of the atoms in the ensemble must be within the same hyperfine manifold, we must use one of the hyperfine states as a "reservoir state" wherein the atoms of the rest of the ensemble can reside. Thus if we want to manipulate a system with  $K$  qubits, we require an atom with  $K+1$  hyperfine states, and furthermore the atomic ensemble must contain at least  $K$  atoms.

To initialize a quantum state with this encoding scheme, we would first optically pump all of the atoms in the ensemble into the reservoir state, creating the state  $|00\dots00\rangle$ . A magnetic field is then applied to lift the degeneracy between the different states via the Zeeman effect. From this  $|00\dots00\rangle$  state, any other state in the computational basis can

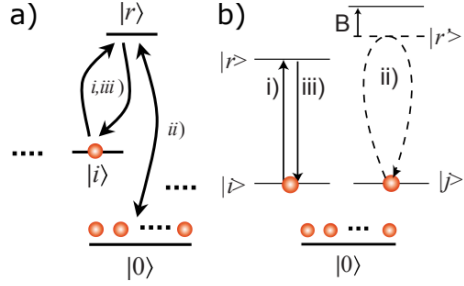


**Figure 1.3** Single and two-qubit gates for collective encoding schemes. a) Rotations between  $|0_i\rangle$  and  $|1_i\rangle$  can be mediated through a Rydberg state. b) A controlled-phase gate mediated by a Rydberg blockade, similarly to single-atom qubits. Reproduced from [15].

be prepared via single-qubit rotations through an intermediate Rydberg state as shown in Figure 1.3. Individual qubits states can be read out by driving transitions between the qubit state and the reservoir state, again coupling via a higher intermediate state, with the presence or absence indicating which state that particular qubit was in.

A major problem with this encoding scheme is that the absence of fluorescence does not distinguish between a  $|0\rangle$  state and an atom in the  $|1\rangle$  state which is lost between qubit operations and read out. One way we can modify our encoding scheme to allow for proper error detection is to instead use pairs of hyperfine states for each qubit instead of single qubits. This allows for redundancy and better detection of errors by making each qubit be composed of the superposition of two distinct  $|0\rangle$  and  $|1\rangle$  states which are both within the hyperfine manifold.

State preparation would be similar to the other encoding scheme, except there would be additional overhead since even  $|0\rangle$  states would require rotating the state through an intermediate, high-lying state. Additionally, approximately only half as many qubits could be made in the same hyperfine manifold, as  $K$  qubits would require a minimum of  $2K + 1$  available hyperfine states.

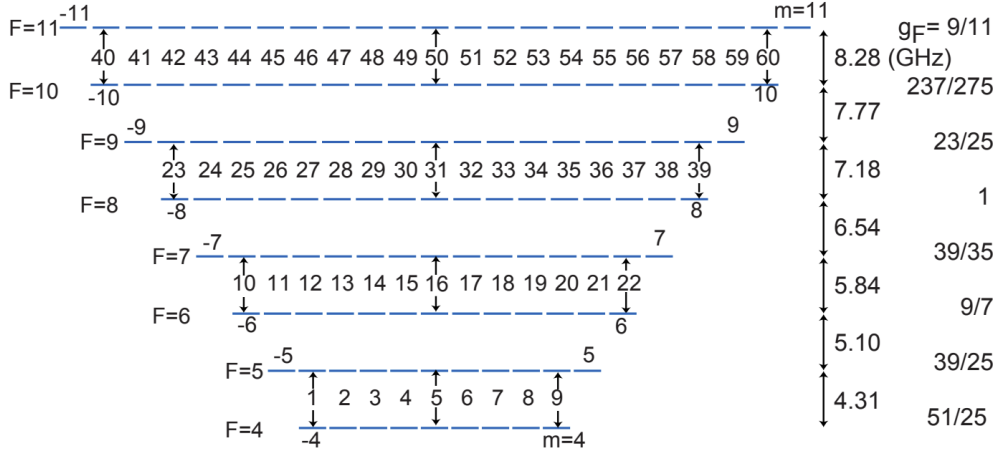


**Figure 1.4** One possible way of pairing holmium’s 128 hyperfine states in a way that produces 60 easily accessible qubits within a single ensemble.

### 1.3.2 Advantages of Ensemble Encoding

With neutral atoms, preparing ensembles of atoms within optical traps is experimentally simpler than preparing single atoms within traps [16]. Additionally, encoding qubits within an ensemble means that a large number of qubits can be stored in the same spatial location, potentially leading to large gains in qubits per volume. Holmium’s ground state has the largest number of hyperfine states of any stable atom at 128, which leads to a potential 127-qubit or 63-qubit register per ensemble depending on the chosen encoding scheme. This suggests that if ensemble encoding can be effectively realized, that reaching a large number of qubits would be easier with an array of ensembles. In fact, with 60-qubit ensembles (see Figure 1.4), it has been estimated that an array of ensembles with all-to-all connectivity via Rydberg blockades could contain 1000 qubits [15].

Ensemble qubits also have the advantage of allowing multiple qubits to be addressed with the same laser, only needing frequency tuning without any required spatial adjustment. Transitions to Rydberg states require multiple photons due to the large energy gaps involved, which means that such spatial adjustments need to be possible with photons of potentially very different wavelengths. Experimental configurations exist which allow for this using specifically fabricated acousto-optic deflectors (AODs), but are also nontrivial and cannot be done with off-the-shelf components without additional undesired diffraction spots [17].

There is also reduced crosstalk between different qubits, as the Rydberg blockade prevents multiple atoms in a single ensemble from entering the Rydberg state simultaneously. Thus, crosstalk between qubits within a single ensemble is inherently suppressed. In an array of qubits, manipulating a specific site is prone to strongly affecting neighboring sites without additional methods such as quantum interference techniques to focus to subwavelength resolution [18], selecting particular sites using an external field [19], or using an additional Stark-shifting beam [20].

The Rabi frequency for the transition between a Rydberg state and the ground state is enhanced by a factor  $\sqrt{N}$  for an  $N$ -atom ensemble, indicative of a much stronger coupling between the states. This can be seen by noting that the Rabi frequency is proportional to the dipole matrix element coupling the states together:

$$\Omega_N \propto \langle r_N | \mathbf{r} | g_N \rangle = \frac{1}{\sqrt{N}} \sum_{i=1}^N \langle r_i | \mathbf{r} | g \rangle = \frac{1}{\sqrt{N}} (N \langle r_i | \mathbf{r} | g \rangle) = \sqrt{N} \langle r_i | \mathbf{r} | g \rangle$$

The stronger coupling and higher Rabi frequency allows for faster single-qubit operations. This  $\sqrt{N}$  enhancement does not apply to two-qubit gates however, as only the reservoir state actually contains more than one atom to provide the stronger coupling.

Finally, encoding qubit states within an entire ensemble means that the qubit state is effectively encoded across all of the atoms as all the atoms within the ensemble are indistinguishable. This actually results in qubit states which are maximally insensitive to atom loss [21]. Consider an uninitialized ensemble of  $N$  qubits with all of the atoms in the reservoir state as  $|g_1 g_2 g_3 \dots g_N\rangle$ . If we initialize an atom into the state  $|0\rangle$ , then the resulting state of the ensemble is a symmetric superposition of every single atom in the ensemble being individually excited to  $|0\rangle$ :

$$|0_N\rangle = \sqrt{\frac{1}{N}} \left( |0_1 g_2 g_3 \dots g_N\rangle + |g_1 0_2 g_3 \dots g_N\rangle + \dots + |g_1 g_2 0_3 \dots g_N\rangle \right)$$

Without loss of generality, let us examine what happens if the first qubit is lost from the ensemble. We can separate out the first state from the rest of the ensemble as follows:

$$|0_N\rangle = \sqrt{\frac{1}{N}} \left( |0\rangle \otimes |g_{N-1}\rangle \right) + \sqrt{\frac{N-1}{N}} \left( |g\rangle \otimes |0_{N-1}\rangle \right)$$

Now, if the first atom is lost, the ensemble's state becomes

$$|0_N\rangle = \sqrt{\frac{1}{N}}|g_{N-1}\rangle + \sqrt{\frac{N-1}{N}}|0_{N-1}\rangle$$

where the first term indicates loss of the information contained in the qubit while the second term is a state where all the remaining atoms are in their expected state. For large  $N$ , as one would expect in an ensemble qubits, the state after losing an atom is approximately unchanged. This is a stark contrast from qubits encoded in single-atom qubits, where the loss of any single atom means that an entire qubit's information is lost.

### 1.3.3 Disadvantages of Ensemble Encoding

The primary concern with ensemble qubits which is not present in single-atom qubits is atom loss from the ensemble due to collisional interactions. In addition to atom loss, collisions between atoms also have the potential for atoms to exchange angular momentum within an ensemble. This would lead to errors in two qubits simultaneously, as these collisions cause  $\Delta m_F = \pm 1$  and the total  $m_F$  is still conserved in this interaction. A possible solution to reduce these undesired collisions is to superimpose a small-period optical lattice for each ensemble such that the ensemble atoms become separated into different trapping sites while the whole lattice fits within the Rydberg blockade radius [15].

Ensemble encoding also has potential problems inherent to the way the encoding scheme works. Additional errors may occur in the form of invalid qubit states; for example, with the paired-state encoding, having an atom in both states is as detrimental to the computation as having atoms in neither state. In both cases, the information in that qubit is effectively lost and needs to be re-initialized from the reservoir. This kind of error can occur due to the aforementioned collisional interactions.

To first order, the variation in the difference between energy levels varies linearly with respect to the field magnitude for the Zeeman effect:

$$\Delta U_Z = \mu_B g_F m_F |B|$$

Noise in the magnetic field is in practice irrelevant for arrays of single-atom qubits since

they use the so-called clock states which have  $m_F = 0$  and are thus insensitive to first order. Ensemble encoding which properly leverages a large number of states would necessarily have to use numerous states which do not have that property. An additional problem with the ensemble approach is that the different hyperfine levels have different  $g_F$  factors; in holmium (see Figure 1.4) they vary by a factor of about 2.5 between  $F = 4$  and  $F = 11$ . To quickly address qubits in both sets of hyperfine states, magnetic field control would also need to be quick and low-noise.

The Rabi frequency providing a stronger coupling between the ground and Rydberg state may allow for faster gates, but the strength of the increased coupling depends on the actual atom count in the ensemble. This can be problematic without a way to deterministically load the same number of atoms into the ensemble every time or reliably detect the atom count *in situ*, as the proper gate time would vary between different experimental trials.

## 1.4 Holmium

Holmium is an ideal element to use for this ensemble encoding scheme. Holmium is a rare earth element in the Lanthanide series, a set of elements which are characterized by having a closed  $6s$  electron shell which shields partially-filled  $4f$  and  $5d$  shells. This results in an electronic configuration with many unpaired electrons and a very complicated energy level structure. Holmium in particular lends itself to being particularly useful for ensemble encoding.  $^{165}\text{Ho}$ , its only stable isotope, has a nuclear angular momentum of  $I = 7/2$  and electron angular momentum of  $J = 15/2$  in its ground state, producing a total angular momentum of  $F = 4\ldots 11$  and a total of 128 Zeeman states available within a single ensemble.

Due to their complex electronic structure, rare earths lack strong closed cycling transitions to be used for a magneto-optical trap (MOT). As a result, the first MOT with a rare earth element was more than a decade after the first MOTs with alkali metals [22]. To date, MOTs with rare earth elements have been made with ytterbium [23], erbium [24], dysprosium [25], thulium [26], and holmium [27]. Many rare earth MOTs have been formed without a repumper despite the MOT transitions not being closed, which has been largely attributed to a combination of the transitions having favorable branching ratios making them "nearly

Element	Electron Config.	Isotope	I	J	F	Hyperfine states
Dysprosium	$4f^{10}6s^2$	$^{156}_{66}\text{Dy}$	0	8	8	17
		$^{158}_{66}\text{Dy}$				
		$^{160}_{66}\text{Dy}$				
		$^{162}_{66}\text{Dy}$	5/2	11/2 ... 21/2	11/2 ... 21/2	102
		$^{164}_{66}\text{Dy}$				
		$^{161}_{66}\text{Dy}$				
Holmium	$4f^{11}6s^2$	$^{163}_{66}\text{Dy}$				
		$^{165}_{67}\text{Ho}$	7/2	15/2	4 ... 11	128
Erbium	$4f^{12}6s^2$	$^{162}_{68}\text{Er}$	0	6	6	13
		$^{164}_{68}\text{Er}$				
		$^{166}_{68}\text{Er}$				
		$^{168}_{68}\text{Er}$	7/2	5/2 ... 19/2	5/2 ... 19/2	104
		$^{170}_{68}\text{Er}$				
		$^{167}_{68}\text{Er}$				
Thulium	$4f^{13}6s^2$	$^{169}_{69}\text{Tm}$	1/2	7/2	3 ... 4	16
Ytterbium	$4f^{14}6s^2$	$^{168}_{70}\text{Yb}$	0	0	0	1
		$^{170}_{70}\text{Yb}$				
		$^{172}_{70}\text{Yb}$				
		$^{174}_{70}\text{Yb}$	1/2	1/2	1/2	2
		$^{176}_{70}\text{Yb}$				
		$^{171}_{70}\text{Yb}$	5/2	5/2	5/2	6
		$^{173}_{70}\text{Yb}$				

**Table 1.1** Atomic properties of the ground state of all the rare earths which have been trapped in a MOT. Holmium has the advantage of having a single isotope as well as the largest number of available hyperfine states.

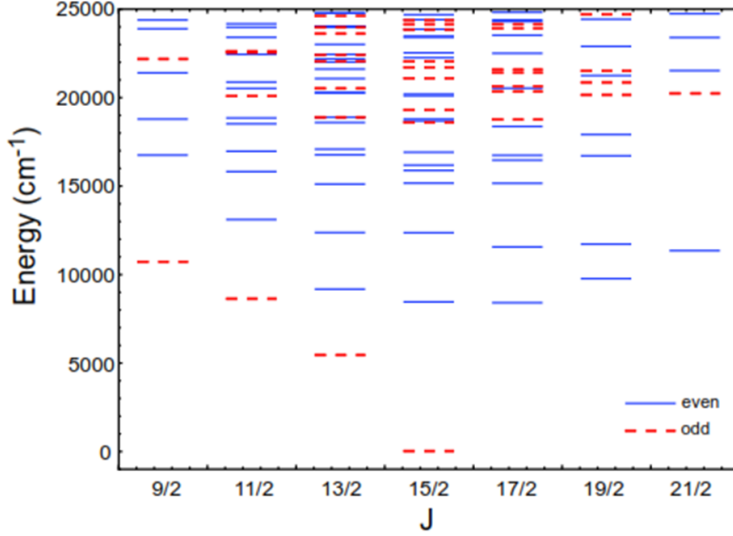


**Figure 1.5** Grotrian diagram showing other easily-accessible fine structure states from the ground state using visible light.

closed" and off-resonant repumping rates being large enough to replace any lost atoms. Additionally, since rare earths are some of the most magnetic elements in the periodic table, in some cases atoms lost from the main cycling transition decay into metastable magnetically-trapped states which eventually decay back into the ground state again [24].

Creating a MOT with rare earth atoms is the first step towards doing interesting physics, and rare earths in particular have been used for studying strongly anisotropic atomic interactions [25], dipolar Bose-Einstein Condensates [28], and highly-correlated states of cold atomic matter [29]. There is also the future prospect of using rare earths for permanent EDM measurements [30], testing for variations in the fine structure constant [31], and quantum memory.

Holmium is, despite all of the other research done in rare earths, still relatively unexplored. While there are many known atomic transitions for holmium [32], there are still more which have not been noted and have turned out to be stumbling blocks for us on our initial attempts at an optical dipole trap. Furthermore, transitions between excited states are almost completely unknown. Previous work on this experiment has examined the properties of the first holmium MOT and characterized the Rydberg spectrum in preparation for qubit gate operations. In this thesis, we present the first successful holmium optical dipole

trap and spectroscopy of another transition to use for narrow-line cooling. Additionally, we present progress towards imaging single holmium atoms and calculations using microwave fields to dress the Zeeman states within the ground state in order to produce magnetically insensitive state pairs for qubits.

Chapter 2 goes over the experimental setup which has been maintained for these experiments. It primarily discusses the layout of the vacuum system and our various laser setups.

Chapter 3 describes the process of producing a Ho optical dipole trap and notes various experimental parameters we used to produce the trap. Additionally, it contains some characterization of the trap's properties as well and measurements of the polarizability of the ground state.

Chapter 4 contains results from spectroscopy a nearby narrower 412 nm line. It shows how we measured the excited-state hyperfine constants using saturated absorption spectroscopy. We then examine the prospect of using this 412 nm transition near to our broad-line MOT in order to further cool the atoms.

Chapter 5 outlines the process we followed to observe single holmium atoms. It also contains an in-depth characterization of our EMCCD camera, necessary in order to quantify our noise sources to compare them to the atom signal.

Chapter 6 explores some of the implications of holmium's very high magnetic moment, which allows it to be used in place of other atoms without needing very strong magnetic fields.

Chapter 7 examines a few theoretical ideas which were planned but have yet to be experimentally realized. In particular we examine the prospect of using microwave fields in order to tune magic B-field conditions, and the prospect of using the stretched states of the hyperfine manifold as a 7-state qudit.

Chapter 8 concludes this thesis, discussing the current status of the project and potential future directions.

# Chapter Two

## Experiment Setup

This chapter outlines a broad overview of the experimental equipment in use on the holmium experiment.

### 2.1 Holmium Source

Due to holmium's high melting point of 1472 °C, it has a very low vapor pressure at room temperature. Using the Clausius-Clapeyron relations in the case of a state transition between a solid and gaseous state, there is a Pressure-Temperature dependence of the form

$$\log P = -\frac{A}{T} + B$$

where  $A = 1.5137 \times 10^4$  K and  $B = 8.426$  for the solid holmium in our setup [33].

At room temperature the vapor pressure is very low, on the order of  $10^{-44}$  Torr compared to the more commonly used  $\approx 10^{-7}$  Torr for rubidium and  $\approx 10^{-6}$  Torr for cesium. In commonly-used UHV conditions, where the pressure of background atoms is  $\approx 10^{-11} - 10^{-9}$  Torr, the vapor pressures of rubidium and cesium at room temperature are more than enough to produce a high atomic flux for experiments. For holmium, reaching the same vapor pressure requires a temperature of at least 700 °C. Additionally, the construction of our vacuum system requires us to heat up the holmium to much higher temperatures in order to have sufficient atom flux in the other parts of the chamber.

Our setup uses a E-Science EC-010-450-1000-HL-L-S high-temperature effusion cell, which hosts a tantalum crucible holding small pieces of solid holmium. The crucible sits inside of

a set of heating coils which heat up the crucible to 1130 °C to produce a strong atomic flux of free holmium atoms, which is then collimated into an atomic beam as it passes through a pinhole.

We use a slowing laser detuned at -440 MHz ( $\approx 13.7$  linewidths) from the MOT transition, aligned to be counter-propagating with the atomic beam, in order to cool down the atoms enough to be captured into our MOT. The root-mean-square speed of atoms at 1130 °C is 470 m/s, corresponding to a Doppler shift of 1.1 GHz at our MOT transition. As a result, the slower beam largely does not interact with the hot atoms from the source, and instead takes a small fraction of the thermal distribution which is already somewhat slow and of a certain velocity range and slows it down even further.

We computationally checked the effect of the slowing beam on the hot atoms using a Monte Carlo method. Atoms are generated with velocities randomly chosen in such a way that results in a speed distribution of

$$f(v) dv = \left( \frac{m}{2\pi kT} \right)^{3/2} 4\pi v^2 e^{-mv^2/2\pi kT},$$

which can be done in a straightforward way by selecting from three independent Gaussian functions with width  $kT/m$  and taking the magnitude of the resulting vector. For each atom, we simulated the process of the atom repeatedly absorbing a Doppler-shifted photon and re-emitting it in a random direction (thereby getting two changes of velocity and changing its observed Doppler shift) until it reached the center of the MOT coils, a distance of 44.3 cm away from the source. The recoil from a single photon is simply  $F = \hbar k$  and the time between scattering events is given by the scattering rate

$$r = \frac{\gamma}{2} \frac{I/I_s}{1 + I/I_s + (2\Delta/\gamma)^2}$$

where in this case  $\Delta$  is the Doppler-shifted detuning from resonance on the 410.5 nm line and  $\gamma$  is its linewidth of 32.5 MHz. The code used for the simulation is available online at <https://github.com/cyip92/slower-beam-simulation> and <https://github.com/QuantumQuadrature/HolmiumCode>.

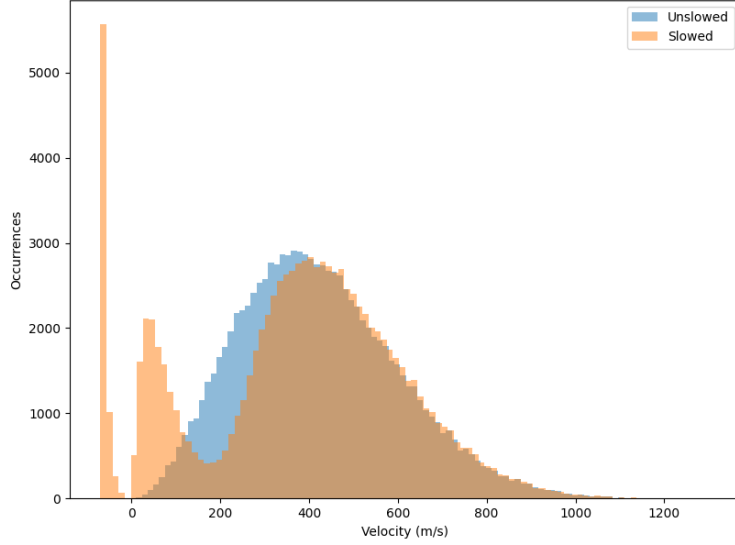


**Figure 2.1** Velocity distribution of holmium atoms out of the oven, with and without the slowing beam present, for the experimental parameters on our experiment. This particular histogram was generated for slowing with  $I/I_{sat} = 10$  and a detuning of -440 MHz, with  $10^5$  trials.

## 2.2 Chiller System

The oven requires active cooling in order to maintain a stable temperature. This is done through a closed-loop liquid cooling system which carries a mixture of 5% ethanol and 95% distilled water back and forth between the oven and a ThermoTek Rack-mount RC22A500-50R0-FSC chiller unit, which is located in a different room than the main experiment to reduce acoustic noise on the lasers from the chiller. If the chiller shuts off for any reason, the oven can potentially heat up beyond its temperature set point as it does not contain any active cooling elements on its own. Therefore to prevent damage to the system, the oven is configured to automatically ramp its set point down to room temperature if the chiller turns off, which is sensed via an interlock circuit.

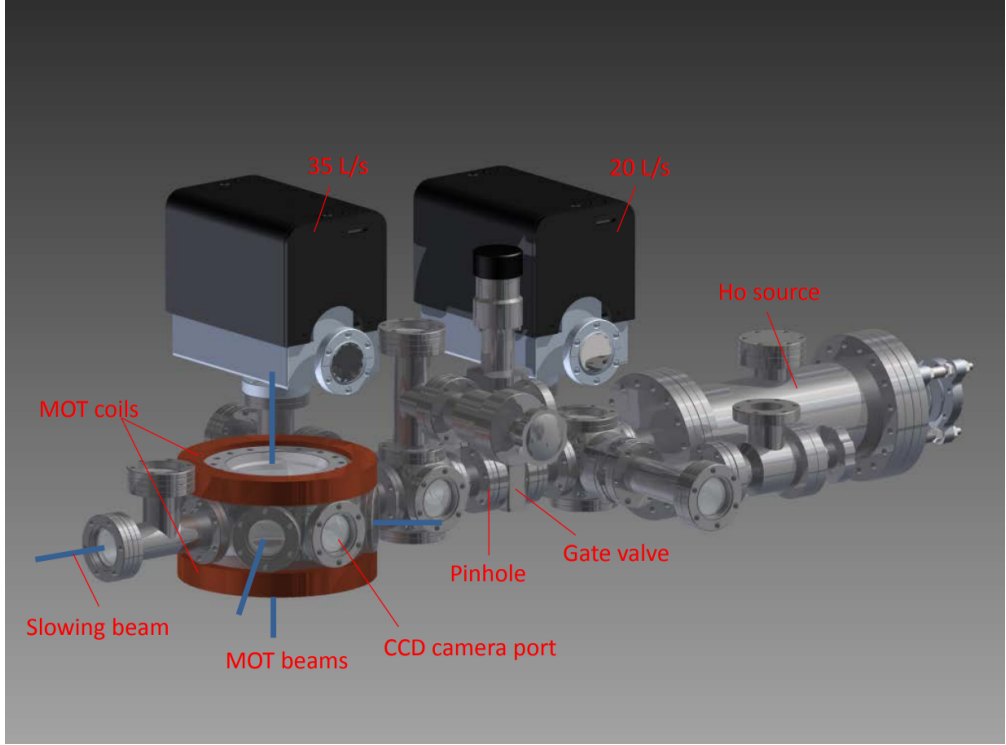


**Figure 2.2** Physical layout of the vacuum system where we produce the optical dipole trap. Reproduced from [34], but is however slightly outdated as our MOT coils have since been removed and installed inside the chamber.

## 2.3 Trapping Region

The vacuum chamber for the holmium experiment consists of two primary sections, the holmium source region (described above) and the trapping region where the MOT and dipole trap are formed. Both sections are fitted with ion pumps for continuous pumping and are separated by a gate valve. Precise details of the construction of the vacuum chamber in general are described in [34] and shown roughly in Figure 2.2.

Most of our experiments take place farther downstream of the atomic beam, within a spherical octagon which permits outside-of-vacuum optical access from the top and bottom faces and six of the eight horizontal windows (See Figure 2.3). The slower beam enters the chamber after being reflected off of a mirror installed within the vacuum chamber, as the previous configuration without the mirror resulted in holmium atoms gradually coating the chamber window which the slower beam passed through. The vertical windows and four of

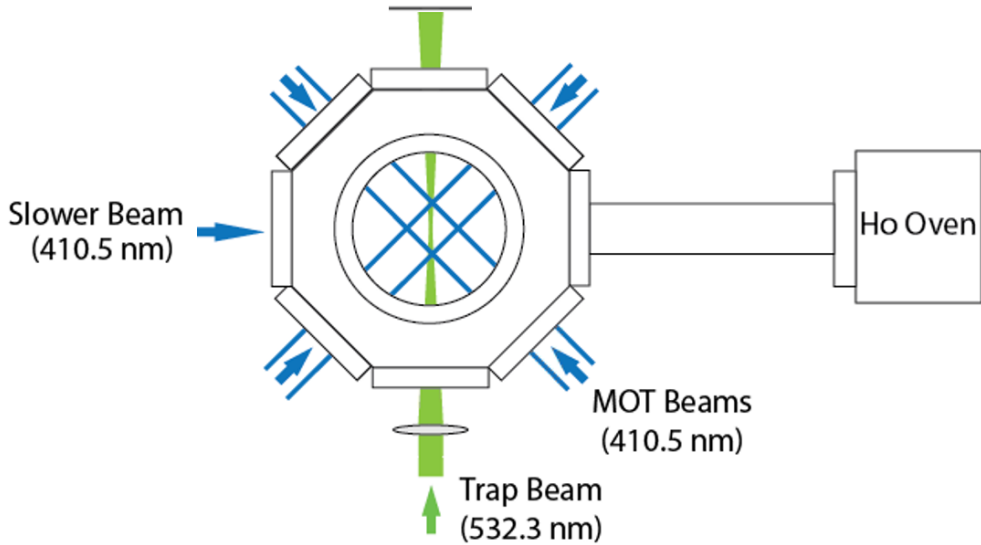


**Figure 2.3** Usage of all the ports of the spherical octagon for the trapping region. The slower beam and its opposite port are in-vacuum paths, while the rest are transparent viewports.

the horizontal windows are used for our MOT beams, one of the remaining windows is used for our combined trapping/imaging setup, and the last window has a beam block installed to safely dump the power from the trapping beam. The vertical faces are large enough to permit the installation of an Andor Luca DL-604M camera looking through the chamber at a slight angle, primarily to assist alignment for the MOT optics.

## 2.4 Laser Systems

### 2.4.1 410.5 nm Ti:Sa

To produce the high-power beams for our setup, we use a 16 W 532 nm Sprout laser from Lighthouse Photonics as our primary pump laser. The Sprout pumps a M Squared SolsTiS laser with a ECDX frequency-doubling module. This laser has three degrees of available tuning - coarse tuning via a bi-refringent filter, medium tuning through an etalon, and fine tuning via a piezoelectric stack. The first two are controlled by M Squared software, and the last is controlled via an analog voltage input. The analog voltage is produced by a Pound-

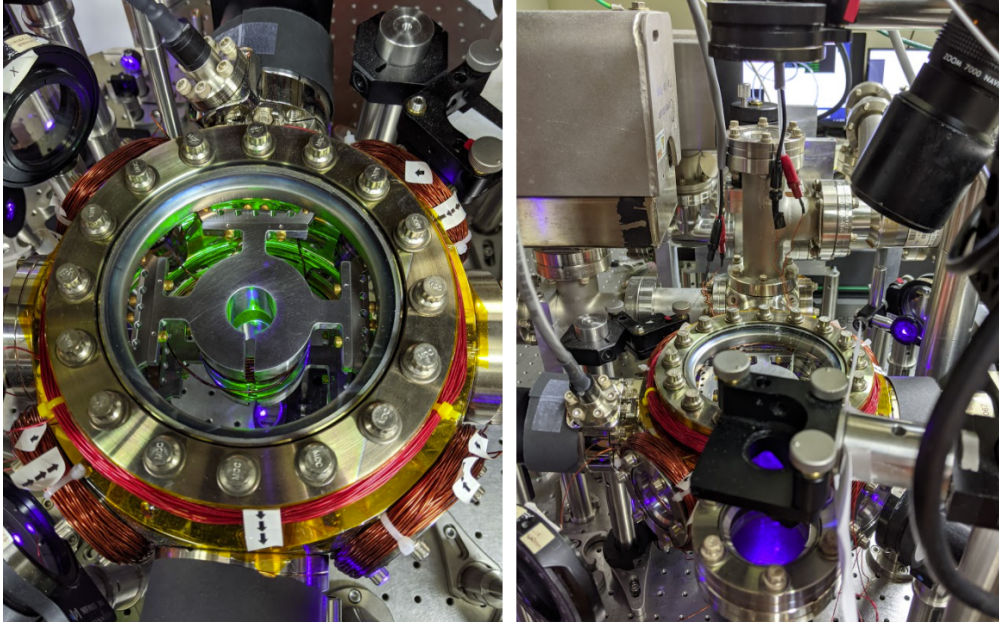


**Figure 2.4** Images of the experimental setup of the trapping region, showing the in-vacuum MOT coils (left). Also shown is the periscope for the slower beam and the Andor camera pointed downward into the chamber (right).

Drever-Hall lock which keeps the laser frequency-stabilized relative to the transmission peaks of a ULE cavity, with a tunable offset sideband (see Appendix B).

This laser is primarily used to produce the experiment's MOT, slower, and imaging light. In this configuration it is tuned to produce light at 821 nm, frequency-doubled to 410.5 nm. At this wavelength, we have observed a maximum 5.1 W of 821 nm light, which corresponds to 2.5 W of 410.5 nm light after the ECDX module. We have also used this laser for our narrow-line spectroscopy, where it was tuned to 824 nm (doubled to 412 nm) and kept at lower power to prolong the lifetime of the pump laser.

We use a HighFinesse WS6-600 wavemeter in order to tune the absolute frequency of the Ti:Sa, good to within 100 MHz. When the Ti:Sa is locked to the ULE cavity peak near 365.1580 THz, it is within about 1 GHz of the MOT transition. Through a combination of tuning the ULE sideband and the Acousto-Optic Modulators, we can tune the slowing beam to be 440 MHz red-detuned of the transition and MOT beams 100 MHz red-detuned (approximately 13 and 3 linewidths, respectively). The AOM for the MOT beams is double-

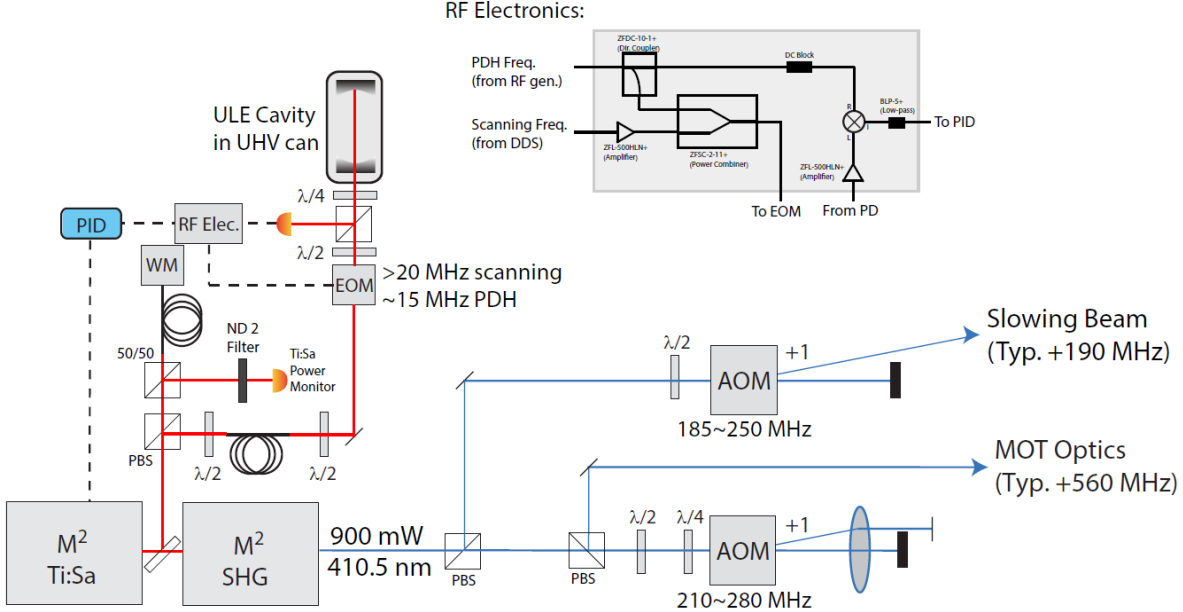


**Figure 2.5** Laser Setup for generating 410.5 nm light

passed, allowing for tuning of the MOT beam frequency independently of the slower without affecting beam alignments.

#### 2.4.2 412 nm Breadboard Setup

We produce 412 nm light for the narrow transition using a system we built in-house. It uses a Sanyo DL8142-201 830 nm laser diode in a Littman–Metcalf ECDL configuration [35], which can generate up to 150 mW at its center frequency. When tuned to 824 nm, it generates roughly 80 mW.

40 mW of the laser's output is split off and coupled into two fibers for locking (normally to our ULE cavity, but the fiber coupling allows us to easily change the reference cavity) and wavelength measurement (using the same wavemeter mentioned above). The rest of the light seeds a Toptica TA-0830-1000-4 1 W Tapered Amplifier, which amplifies the IR power to roughly 600 mW.

The amplified IR light goes through some beam-shaping optics, and then to a bowtie cavity with an LBO (Lithium Triborate) crystal for cavity-enhanced second harmonic generation. The cavity itself is stabilized via a Hansch-Couillaud method [36], and further

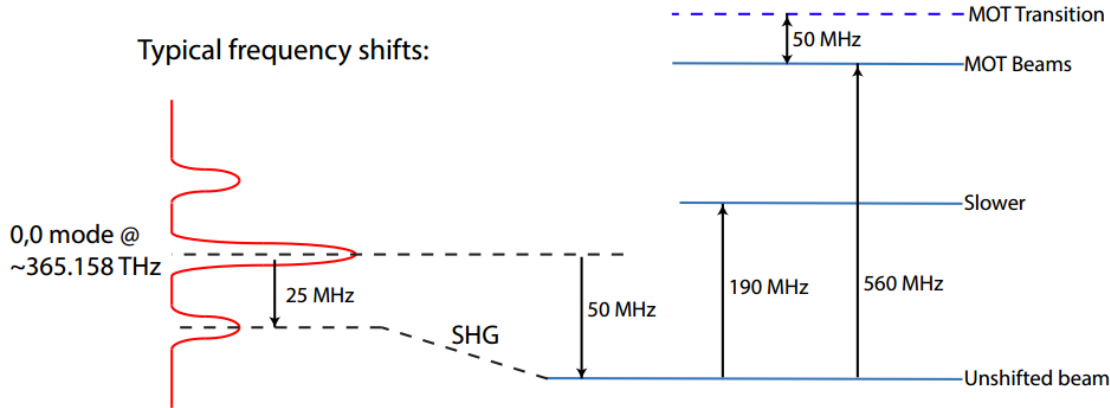


**Figure 2.6** Example of frequency shifts made by the AOMs in our setup, in order to generate light at the requisite frequencies relative to the MOT transition

details about the crystal's properties and the cavity's physical construction can be found in [37].

The output light from the SHG cavity is then directed towards the optics for the MOT through alignment of optics in free space. Our configuration is marginal on power and using a fiber to decouple the alignments between the MOT and the breadboard would result in an unacceptable power loss.

### 2.4.3 532 nm ODT Diode Laser

Our Trapping laser is a Verdi-V5 532 nm diode laser capable of outputting 5W with a linewidth of 0.1 nm. The beam goes through a Gooch & Housego MFS050-3S4B9-5-5W-20BW Acousto-optic Modulator in order to be able to switch it on and off at a maximum rate of about 250 kHz. The +1 diffraction order of the AOM is coupled into a fiber which leads to our combined cage rod-mounted trap/imaging system, described in more detail in Section 2.6.

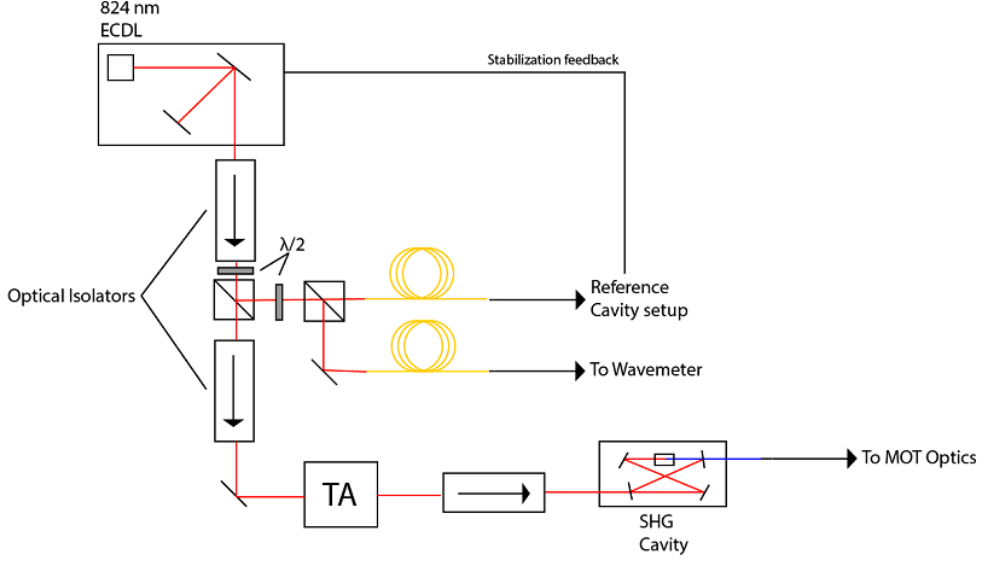


**Figure 2.7** Schematic of the home-built setup used for generating 412 nm light. Details of the locking setup are not included here as we have used different reference cavities for different situations. The optical isolators are required to prevent backreflections from causing undesired feedback to the ECDL and TA.

## 2.5 Reference Cavities

### 2.5.1 ULE Cavity

ULE glass is a proprietary material made by Corning with a coefficient of thermal expansion of  $10^{-8} K^{-1}$ . This extremely low coefficient of thermal expansion makes it a good material for applications where having a constant reference length despite changing ambient conditions is extremely important.

Our ULE reference cavity was made by Advanced Thin Films, model ATF-6020-4. It consists of two mirrors (reflectivity  $R = 0.999984$ ) separated by a 10 cm ULE spacer, in a slightly offset hemispherical configuration to give a FSR of 1.5 GHz and transverse mode spacing of 220 MHz. The transmission peaks of the ULE cavity have a linewidth of 7.6 kHz.

It is kept under UHV at a pressure of  $\approx 10^{-8}$  Torr, and temperature-controlled to  $\pm 4 mK$  with heater tape monitored by an Arroyo TECSource 5240 [38]. This results in an absolute frequency stability of about 14.5 kHz at the frequencies we are using.



**Figure 2.8** Image of the Quantaser Etalon inside of its temperature-controlled enclosure (temporarily opened for this image). The steel enclosure is connected to its mounting posts via nylon screws with an O-ring as a spacer in order to keep it mechanically stable but thermally isolated from the optical table. This part of the experimental setup is also inside of a large plexiglass box which was intended to block excess scatter resulting from the optics described in section 2.4.1, incidentally providing another layer of thermal stability.

### 2.5.2 Quantaser Etalon

The linewidth of the transition we form our broad MOT on is 32 MHz, which is a few orders of magnitude wider than the linewidth of the ULE cavity. Because of this, using the ULE cavity as a reference for the broad MOT would result in a much tighter stability than what is required. Strictly speaking, there is nothing wrong with a tighter frequency reference, but in practice very high finesse cavities are harder to set up and maintain due to stricter requirements on the feedback electronics. Therefore, we additionally have a lower-finesse cavity for referencing the broad transition.

The low-finesse cavity we used is a Quantaser FPE002D Fabry-Perot Etalon, with coatings intended for use at 750 nm to 850 nm. This particular etalon came with a temperature controller, also from Quantaser, which has PID control to control the temperature of the etalon to within 1 mK. The frequency at which the peaks of the etalon occur are tuned via the temperature, with a shift of 2.83 MHz per mK on its set point and a separate shift of  $\approx$  7 MHz per K of the ambient temperature.

We can expect the controlled part of the peak center to be within 2.83 MHz of its target, as noted above, but the ambient temperature of the room also plays a role in the peak location. However we also expect long-term variations of up to 2 K over the course of weeks according to long-term data logging our lab has for room temperatures, which corresponds to an unacceptably large variation of 14 MHz in the peak location. To address this issue, we set up a machined, stainless steel enclosure in which we installed the Etalon, and then externally affixed some thermoelectric coolers and heat sinks controlled by an Arroyo TECSOURCE 5240. Effectively this created a smaller, thermally controlled "room" when a much more stable ambient temperature.

## 2.6 Imaging setup

Due to limited optical access into the vacuum chamber itself, we combine our dipole trapping laser with our atom imaging path using a Thorlabs DMLP425 Long-Pass Dichroic. On the combined path, the beams are focused through a pinhole for spatial filtering, followed by a specifically-designed high-NA compound lens system with an effective focal length of 11.5 cm [39]. The compound lens system allows for both maximal light collection from the atom fluorescence and for the spot size of the trap to be focused down to a radius of 4  $\mu\text{m}$ . Towards the camera there is a pair of bandpass filters, a Thorlabs FB410/10 and Semrock FF01-415/10, both of which act to filter out any light which has a wavelength other than the atom fluorescence (primarily the trap beam). Finally, the atom fluorescence goes through a Thorlabs AC254-150 achromat to be focused down onto the CCD of our EMCCD camera which is outlined in more detail in Chapter 5.

There is a coupling between the alignments of the 532 nm trap light and the 410.5 nm

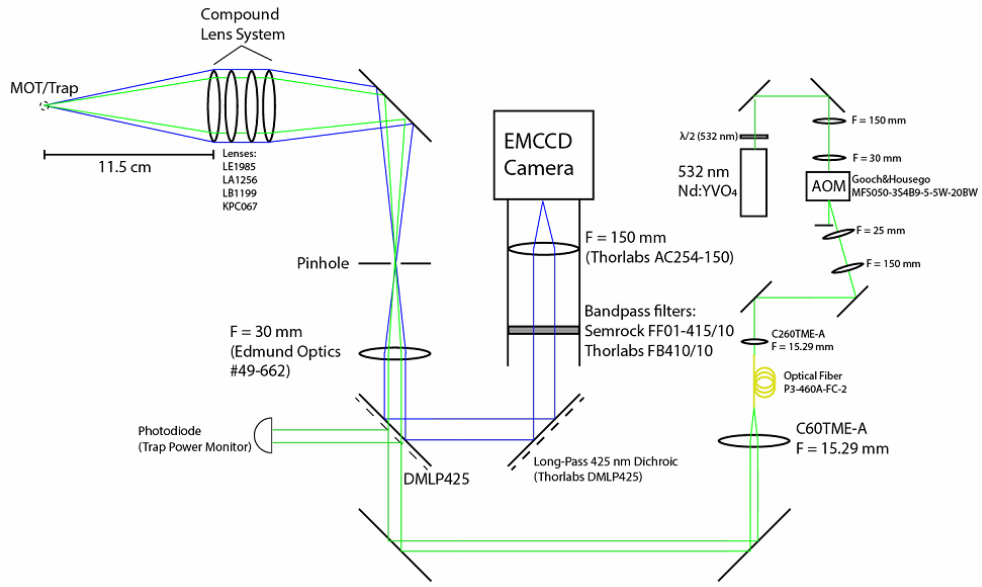


**Figure 2.9** Optical path for combined trapping and imaging. The location of the EMCCD camera in the diagram is reserved for either the Princeton Instruments ProEM 512+ or the Hamamatsu C9100-13. The NA of the collection lens is 0.202.

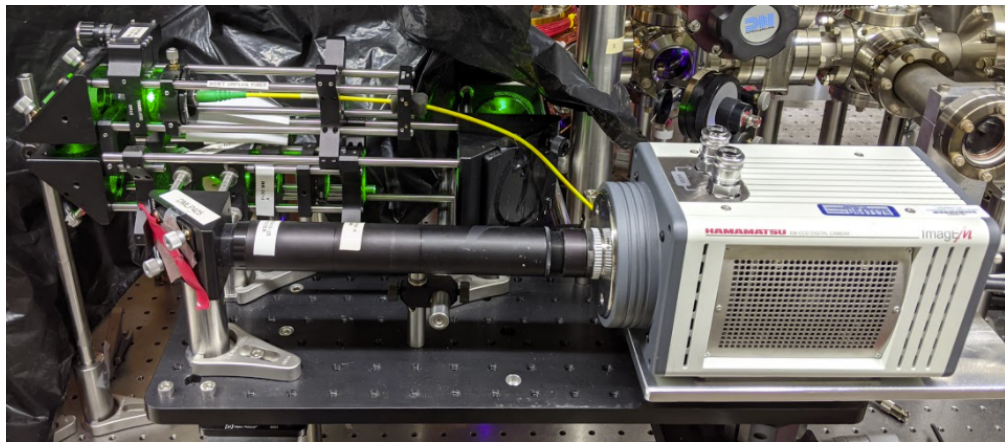


**Figure 2.10** Picture of the cage rod-mounted optics for the combined trap and image setup, with the shroud pulled back. The main purpose of the shroud is to block excess scatter from the trapping light; in Chapter 5 we note that noise from background light sources is negligible.

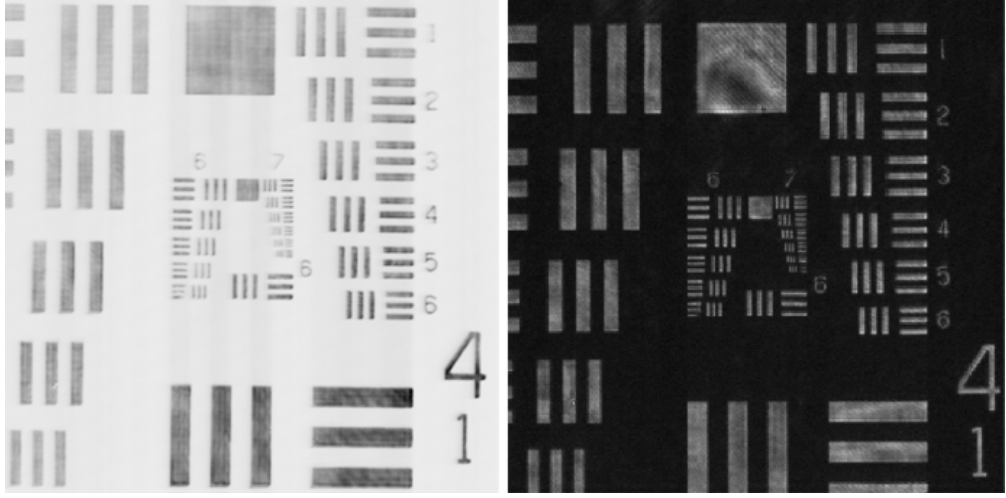


**Figure 2.11** Image of the US Air Force resolution chart as imaged on the ProEM 512 (left) and Hamamatsu C9100-13 (right) cameras.

fluorescence from the atoms, which we have carefully characterized and aligned so that their focal planes are in the same location. This alignment process is outlined in Appendix A.

We used the 1951 USAF resolution test chart (Figure 2.11) in order to measure a calibration factor for the pixel size in each image, as well as to diagnose what the smallest resolvable features (Figure 2.12) in the camera images are. Since we are using the camera to image light at 410.5 nm, we produced images of the resolution test chart which were backlit by a large collimated 410.5 nm laser beam. The result was  $1.501 \mu\text{m}/\text{pixel}$ , with the smallest clearly resolvable element without any significant blurring being  $3.11 \mu\text{m}$  in size. The physical pixel size of the two cameras we used differ by a small enough amount that the USAF reference images taken with either camera installed are mostly indistinguishable in scale, so the calibration factor was primarily a characteristic of the optical setup.

## 2.7 Control System

The experiment is controlled by the software originally described in [40], and is undergoing active development (as of 2020) by various people in Saffman Lab. The code can be found at <https://github.com/QuantumQuadrature/CsPyController>.

The control hardware is a National Instruments SMB2163 [41] to provide fast, precisely-



**Figure 2.12** Inset image of the smallest resolvable elements on the USAF resolution chart, using the ProEM 512 camera. The slots indicated in this figure range in width from  $3.90\mu m$  to  $2.19\mu m$  wide.

timed TTL pulses, a National Instruments BNC2090A [42] to provide analog input and output channels for our magnetic fields and spectroscopy data, and a DDS generator [43]. The software control for our DDS generator was also designed within our research group, which allows it to act as a programmable multiple-channel RF source for our AOMs. All of these devices individually interface with the CsPy software running on a dedicated lab computer for the Holmium experiment, which allows for precise synchronization of timing across the whole experiment.

## 2.8 Conclusion

In this chapter, we have described the layout of our experiments which we use to produce a cold ensemble of holmium atoms, as well as the basic calibration done on each individual part. This provides the basic setup of equipment we use for the dipole trap, narrow-line cooling, and single atom measurements.

# Chapter Three

## Holmium Dipole Trap

To produce a cold cloud of holmium atoms, we first produce a Magneto-Optical Trap (MOT) of holmium, and then load the cold atoms from this MOT into a Far Off-Resonance Trap (FORT).

### 3.1 Broad-line Magneto-Optical Trap

To make our MOT, we cool -70 MHz detuned from the strong  $4f^{11}(4I^{\circ})6s^2, F = 11$  to  $4f^{11}(4I_{15/2}^{\circ})6s6p(^1P_1^{\circ}), F' = 12$  transition at 410.5 nm [27]. This transition has a natural linewidth of  $\gamma/2\pi = 32.5$  MHz, corresponding to a Doppler cooling limit of  $780 \mu K$ .

The MOT does not require a repumper due to the depumping rate (less than  $100 s^{-1}$  due to favorable branching ratios) being much less than the repumping rate for the Raman process  $F_g = 10 \rightarrow F_e = 11 \rightarrow F_g = 11$ , estimated to be  $2.4 \times 10^7 s^{-1}$  on resonance [27]. This comes from a combination of a fortuitous arrangement of the ground and excited hyperfine separations and the broadness of the MOT transition which causes a high off-resonant repumping rate. When loading the MOT at our detuning of -70 MHz, this same light is -680 MHz detuned from the repumping transition as well - this results in an off-resonant repumping rate of  $2.5 \times 10^5 s^{-1}$ . Thus the cooling light effectively acts as its own repumper.

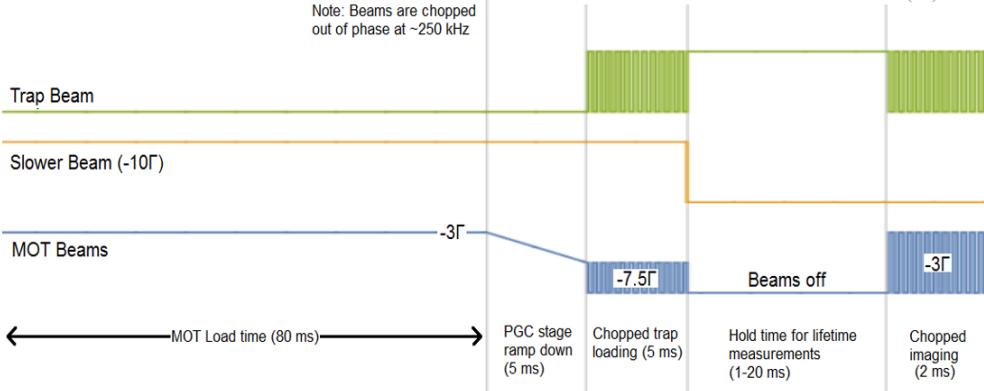


**Figure 3.1** Pulse diagram of the experimental sequence we used to load our FORT.

## 3.2 Trap Loading

We load our FORT by first loading the MOT for 80 ms, followed by a brief period of polarization gradient cooling [44], then a period of trap loading where we chop the beams out of phase with each other (described in more detail later in Section 3.4). At this point the atoms have been loaded into the FORT and we can further manipulate them as needed for various purposes.

## 3.3 532 nm Trap

For our holmium trap, we considered three possible candidates for wavelengths - 445 nm, 532 nm, and 1064 nm. Our initial attempt was with 445 nm, which was produced by a very inexpensive laser purchased on eBay. It later conspired that there was a transition from the ground state at 444.9 nm which we did not know about, and the laser's linewidth of multiple nm made it entirely infeasible for use as a trapping laser. We tried 532 nm next and were able to produce a trap with it, without needing to attempt using 1064 nm. 1064 nm is slightly less desirable as it would require much more power to produce a trap with the same parameters at 532 nm. Additionally, experimental setup and alignment is more difficult as 1064 nm is well outside the visible range of wavelengths and also requires optics with less commonly used coatings.

Holmium has good properties at 532 nm, and large amounts of 532 nm light is commer-

Wavelength (nm)	Polarizability (Å)	Scattering rate (s <sup>-1</sup> )
445	138.35*	199.06*
532	46.50	23.86
1064	23.90	3.22

**Table 3.1** Polarizability and photon scattering rate for optical dipole traps at our three candidate wavelengths. Note that the values for 445 nm may be inaccurate due to a transition of unknown linewidth at 444.9 nm. Scattering rates were calculated using figures from our current trap - 640 mW power and 4.6 micron spot radius.

cially available for a relatively low cost compared to most other wavelengths. The figures of merit for determining how good an optical dipole trap is at a given wavelength are the atomic polarizability and the photon scattering rate, which depend on a combination of available laser power and internal atomic properties [45].

### 3.3.1 Atomic Polarizability

The atomic polarizability is a quantum mechanical property of atoms which is named analogously to the behavior of a classical electric dipole within an oscillating electric field. This can be calculated fairly directly from equating the energy shift according to second-order perturbation theory to the energy shift of an electric dipole in an oscillating electric field [45]. The Hamiltonian for such an interaction is given by a dot product between the atom's dipole moment and the electric field,  $\mathcal{H} = -\hat{\mathbf{d}} \cdot \mathbf{E}$ . The energy shift for a given state  $a$  is then given by

$$\Delta U_a = \sum_b \frac{|\langle \psi_b | \mathcal{H} | \psi_a \rangle|^2}{U_a - U_b} = \sum_b \frac{\langle \psi_a | \mathcal{H}^\dagger | \psi_b \rangle \langle \psi_b | \mathcal{H} | \psi_a \rangle}{U_a - U_b}$$

where the sum runs over all atomic states. We can then use the fact that we are summing over all states, the fact that the states form a complete basis (ie.  $\sum_b |b\rangle \langle b| = I$ ), and the fact that  $U_b$  is simply given by the unperturbed Hamiltonian  $\mathcal{H}_0$  to write out a Hamiltonian specifically for the electric dipole interaction (commonly abbreviated as  $E1$ ):

$$\mathcal{H}_{E1} = \frac{(\mathbf{E}^* \cdot \hat{\mathbf{d}})(\mathbf{E} \cdot \hat{\mathbf{d}})}{U_a - \mathcal{H}_0}$$

This is technically sufficient to describe how atoms interact with electric fields based on the orientation of the atom and fields, but it is not immediately clear how the interaction changes for any given change of the electric field. Mathematically it would be more helpful if the polarizability could be separated into multiple components which clearly transform in certain ways.

We can do this by first rewriting the scalar products in  $\mathcal{H}_{E1}$  as a scalar product between two  $3 \times 3$  tensors,  $\mathbf{E} \otimes \mathbf{E}^*$  for the electric field and  $\hat{\mathbf{d}} \otimes \hat{\mathbf{d}}$  for the dipole operator:

$$\mathcal{H}_{E1} = \frac{1}{U_a - \mathcal{H}_0} \{ \mathbf{E} \otimes \mathbf{E}^* \} \{ \hat{\mathbf{d}} \otimes \hat{\mathbf{d}} \}$$

This allows us to focus on the electric field, as the dipole operator can be treated as a self-contained property of the atom itself. The electric field tensor has the following structure:

$$\{ \mathbf{E} \otimes \mathbf{E}^* \} = \begin{pmatrix} E_x^2 & E_x E_y^* & E_x E_z^* \\ E_y E_x^* & E_y^2 & E_y E_z^* \\ E_z E_x^* & E_z E_y^* & E_z^2 \end{pmatrix}$$

Then we perform what is essentially a change of basis in order to separate our degrees of freedom in a desirable way.  $\mathbf{E} \otimes \mathbf{E}^*$  is an element of a 9-dimensional space, described in terms of complex electric field amplitudes on three orthogonal axes. Without loss of generality, we can assume that the z axis of our spatial coordinate system is the quantization axis for the electron angular momentum.

We can split these 9 dimensions into 3 separate parts, corresponding to three irreducible subspaces which maintain the same symmetry properties regardless of any change of basis. The three parts are multiples of the identity matrix (1 dimension), antisymmetric matrices (3 dimensions), and traceless symmetric matrices (5 dimensions). This change of basis is most useful when done in the same way angular momenta are coupled together, with the appropriate Clebsch-Gordan coefficients:

$$\begin{aligned}
\{\mathbf{E} \otimes \mathbf{E}^*\}_{0,0} &= -\frac{E^2}{\sqrt{3}} \\
\{\mathbf{E} \otimes \mathbf{E}^*\}_{1,0} &= -\frac{i}{\sqrt{2}}(E_x^*E_y - E_y^*E_x) \\
\{\mathbf{E} \otimes \mathbf{E}^*\}_{1,\pm 1} &= \frac{1}{2}(E_z(E_x \pm iE_y) - E_z(E_x^* \pm iE_y^*)) \\
\{\mathbf{E} \otimes \mathbf{E}^*\}_{2,0} &= -\frac{1}{2}(E_x^2 + E_y^2 - 2E_z^2) \\
\{\mathbf{E} \otimes \mathbf{E}^*\}_{2,\pm 1} &= \mp E_z(E_x \pm iE_y) \\
\{\mathbf{E} \otimes \mathbf{E}^*\}_{2,\pm 2} &= \frac{(E_x \pm iE_y)^2}{2}
\end{aligned}$$

We then need to do a similar process with the tensor for the dipole operator. In this case each entry in the tensor couples together each atomic state with nearby states with similar amounts of angular momenta. The effective change of basis we do on the tensor means that we need to add the appropriate Clebsch-Gordan and Wigner 6-j symbols in order to operate on the correct kets. Averaging each individual  $\Delta j$  tensor component over all its allowable  $\Delta m$  values, we produce three different components of the polarizability with some additional numerical prefactors for the sake of later convenience:

$$\begin{aligned}
\alpha_0 &= \frac{2}{\sqrt{3}} \frac{1}{U_a - \mathcal{H}_0} \langle n_a j_a m_a | \{\hat{\mathbf{d}} \otimes \hat{\mathbf{d}}\}_{0,0} | n_a j_a m_a \rangle = \frac{2}{3(2j_a + 1)} \sum_{n'j'} \frac{|\langle n'j' || \hat{d} || n_a j_a \rangle|^2}{U' - U_a} \\
\alpha_1 &= -\sqrt{2} \frac{1}{U_a - \mathcal{H}_0} \langle n_a j_a m_a | \{\hat{\mathbf{d}} \otimes \hat{\mathbf{d}}\}_{1,0} | n_a j_a m_a \rangle \\
&= \sqrt{\frac{6}{j_a(j_a + 1)(2j_a + 1)}} \sum_{n'j'} (-1)^{j'+j_a} \left\{ \begin{array}{ccc} j_a & 1 & j_b \\ 1 & j_a & 1 \end{array} \right\} \frac{|\langle n'j' || \hat{d} || n_a j_a \rangle|^2}{U' - U_a} \\
\alpha_2 &= -\frac{4}{\sqrt{6}} \frac{j_a(2j_a - 1)}{3m_a^2 - j_a(j_a + 1)} \frac{1}{U_a - \mathcal{H}_0} \langle n_a j_a m_a | \{\hat{\mathbf{d}} \otimes \hat{\mathbf{d}}\}_{2,0} | n_a j_a m_a \rangle \\
&= \sqrt{\frac{40j_a(2j_a - 1)}{3(2j_a + 3)(2j_a + 1)(j_a + 1)}} \sum_{n'j'} (-1)^{j'+j_a} \left\{ \begin{array}{ccc} j_a & 1 & j_b \\ 1 & j_a & 2 \end{array} \right\} \frac{|\langle n'j' || \hat{d} || n_a j_a \rangle|^2}{U' - U_a}
\end{aligned}$$

$\alpha_0$  is the scalar polarizability,  $\alpha_1$  is the vector polarizability, and  $\alpha_2$  is the tensor polarizability, named as such because they relate to electric field polarizations analogously to

how general rank-2 tensors are decomposed into spherical tensor operators. Notice that  $\alpha_0$  is an equal energy shift depending on the magnitude of the field,  $\alpha_1$  is an energy shift for circularly-polarized light (which only occurs when  $\mathbf{E}$  and  $\mathbf{E}^*$  are non-parallel), and  $\alpha_2$  is a state-dependent shift which contributes no net shift when averaged over all states. With these particular choices of prefactors, the total energy shift of a state (in CGS units) due to a linearly polarized applied electric field is

$$\Delta U = -\frac{E^2}{2}\alpha_0 + \frac{E^2 - 3E_z^2}{4} \frac{3m^2 - j(j+1)}{j(2j-1)}\alpha_2$$

where  $j$  and  $m$  are the typical electron angular momentum quantum numbers and  $E_z$  is the component of the field projected onto the same axis as the angular momentum. In particular this leads to a much simpler expression of

$$\Delta U = -\frac{E_z^2}{2}(\alpha_0 + \alpha_2)$$

when  $E = E_z$  and  $m = j$ .

Since the vector polarizability corresponds to antisymmetric tensors, it is necessarily nonzero if and only if the electric field tensor has off-diagonal elements. This only occurs for circularly polarized light, and the above definition of vector polarizability results in an AC Stark shift of

$$\Delta U = -\frac{1}{4}\alpha_1 q m_j |E_q|^2$$

where  $q$  is the electric field projection onto a spherical basis where  $q = \pm 1$  corresponds to right-hand and left-hand circular polarization and  $q = 0$  is linear polarization.

### 3.3.2 Calculating Holmium's Polarizability

In most cases, the dipole matrix element cannot be calculated from first principles. To do so would require the ability to calculate the radial matrix element of the atomic wavefunction, which is known exactly only for hydrogen and very approximately for some states of alkali atoms. Any more complicated, non-hydrogenic electron structures preclude any realistic

possibility of determining the full electron wavefunction and thus any way to analytically calculate the matrix element.

Instead, the matrix element can be calculated from other atomic properties which are more easily measurable. This is commonly done by using the radiative lifetime of a state. From the lifetime we can calculate the transition's oscillator strength, a quantity describing how strong the transition is compared to a classical electron oscillator with the same resonant frequency:

$$\gamma = \frac{1}{4\pi\epsilon_0} \frac{2e^2\omega^2}{m_e c^3} \frac{2j_a + 1}{2j_b + 1} f$$

where  $\gamma$  is the transition's lifetime,  $e$  and  $m_e$  are the mass and charge of the electron,  $\omega$  is the angular frequency of the transition,  $j_a$  and  $j_b$  are the angular momenta of the lower and upper states, and  $f$  is the oscillator strength. The oscillator strength itself is related to the reduced radial matrix element squared:

$$f = \frac{2m_e\omega}{3\hbar(2j_a + 1)} |\langle n_b j_b || \hat{r} || n_a j_a \rangle|^2$$

In spectroscopic data, the oscillator strengths are often cited as values of  $\log_{10}(gf)$  where  $g = 2j_a + 1$  is the degeneracy of the lower energy level.

For holmium, the polarizability of the ground state can be seen in Figure 3.2. It is largely dominated by the scalar polarizability, except near some transitions where the tensor polarizability sometimes has a minor contribution. The vector polarizability is relatively negligible, which is approximately a factor of 20-50 smaller than the scalar polarizability across nearly the entire range of feasible trapping wavelengths.

### 3.3.3 Trap Depth

The atomic polarizability gives a way to calculate the response of a trapped atom to an external AC electric field, but a uniform field would result in a uniform potential. The local minimum in potential energy required to localize and trap atoms comes from the spatial structure of the electric field - that is, from the optical shape of the laser beams forming the trap itself.

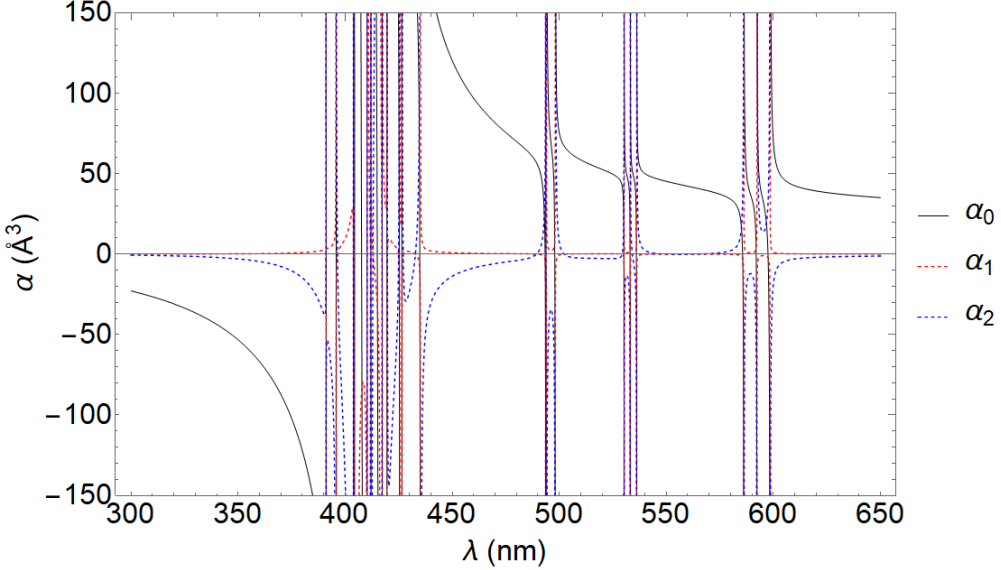


**Figure 3.2** Plot of holmium’s polarizability over most of the visible light range. The total polarizability farther away from transitions is primarily determined by the scalar and tensor components.

With a positive polarizability, we can see that a higher field intensity corresponds to a more negative potential energy. Therefore the atom would be drawn to the location of the highest field intensity; this situation is called a *red-detuned* dipole trap. Conversely, an atom with a negative polarizability would be forced away from areas of higher intensity and towards places with low field intensity; this is a *blue-detuned* dipole trap.

Optically speaking, red-detuned traps are easier to experimentally realize as simply focusing down a beam to a small spot produces a local maximum in intensity where the trap can be formed. Blue-detuned traps are more difficult as they usually require multiple beams in careful alignment or specialized optical setups to create the appropriate beam cross-section [46][47]. However, despite the extra experimental overhead blue traps may be desirable as the atoms are trapped in a volume with minimal trapping light.

For the holmium experiment, we use a red-detuned trap at 532 nm. The trap depth of a FORT formed from a focused Gaussian beam is calculated from

$$\Delta U = \frac{1}{k_b} \frac{4P\alpha}{cw^2}$$

where  $k_b \approx 1.38 \times 10^{-23} \text{ J/K}$  is the Boltzmann constant,  $P$  is the total power in the trap

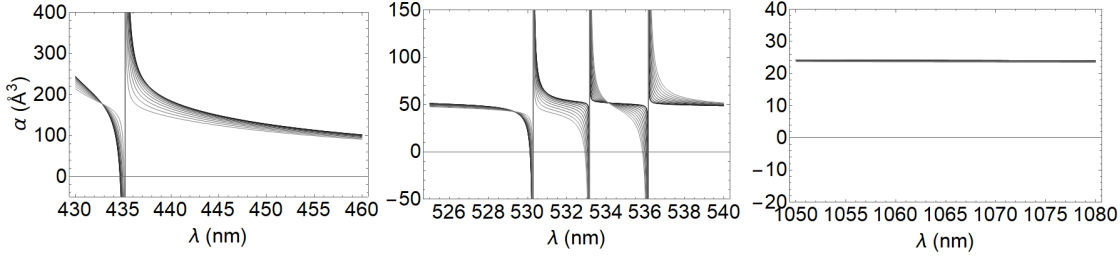


**Figure 3.3** Atomic polarizability of holmium near 445 nm, 532 nm, and 1064 nm. Each set plot is a family of curves corresponding to the polarizability of each separate  $m_F$  state within the  $F = 11$  states. All of these states have slightly different polarizabilities in general due to a nonzero  $\alpha_2$ .

beam,  $\alpha$  is the atomic polarizability,  $c$  is the speed of light, and  $w$  is the trap beam waist (radius). This gives a result in units of temperature, which can be directly compared to the kinetic temperature of the atoms themselves. In practice, a good trap depth is at least an order of magnitude larger than the temperature of the atoms themselves, in order to keep most of the atoms in the high-velocity tails of the distribution confined as well.

### 3.3.4 Photon Scattering Rate

A good dipole trap has a deep trap depth, but also a low photon scattering rate. This is because photons scattering off of the atoms acts as a heating mechanism, giving the atoms extra momentum as they interact with the light. Essentially, photon scattering is an undesired side effect of using the laser field to produce the potential which we want to minimize. The total photon scattering rate is given by a sum over the contributions from all atomic transitions to that particular state, similarly to the polarizability

$$r_{sc} = \sum \frac{\gamma}{2} \frac{I/I_{sat}}{1 + 4(\Delta/\gamma)^2 + I/I_{sat}} \quad (3.1)$$

where  $\gamma$  is the linewidth of the transition,  $\Delta = \omega - \omega_0$  is the detuning from the transition,  $I$  is the intensity of the light in the trap, and  $I_{sat}$  is the transition's saturation intensity given by

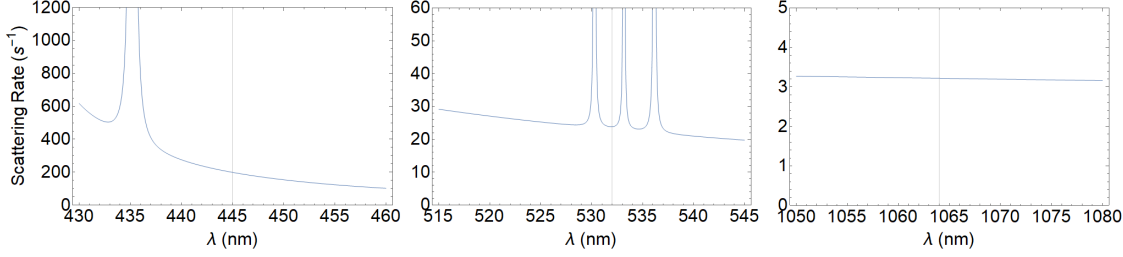


**Figure 3.4** Scattering rates of light at 445 nm, 532 nm, and 1064 nm. The difference in magnitude between the different wavelengths compared to their respective differences in polarizability comes from the  $1/\Delta^2$  dependence. Calculated using a 640 mW beam with a 4.6 micron focus.

$$I_{sat} = \frac{\hbar\gamma\omega^3}{12\pi c^2}$$

Note that asymptotically the contribution from each transition falls off more quickly as a function of  $\Delta$ , following a  $(\gamma/\Delta)^2$  scaling rather than a  $\gamma/\Delta$  scaling. Therefore, to minimize the effect of photon scattering a dipole trap should be far away from any nearby transitions relative to their respective linewidths.

### 3.4 AC Stark Shift

Initial attempts at creating a Holmium FORT at 532 nm were unsuccessful due to the ground and excited states of the MOT transition being shifted due to the AC Stark Effect, which causes the energy of atomic states to be shifted by an amount proportional to the intensity of the light:

$$\Delta U = -\frac{1}{4}\alpha|\mathcal{E}|^2 \quad (3.2)$$

The effect of the AC Stark shift can clearly be seen *in situ* by forming and imaging a MOT on the trap camera, and then turning on the trap beam while keeping all of the other parameters to form a MOT the same. The result is a MOT which has a "hole" where the trapping beam overlaps it (see Figure 3.5). While it looks like the atoms are being "blown

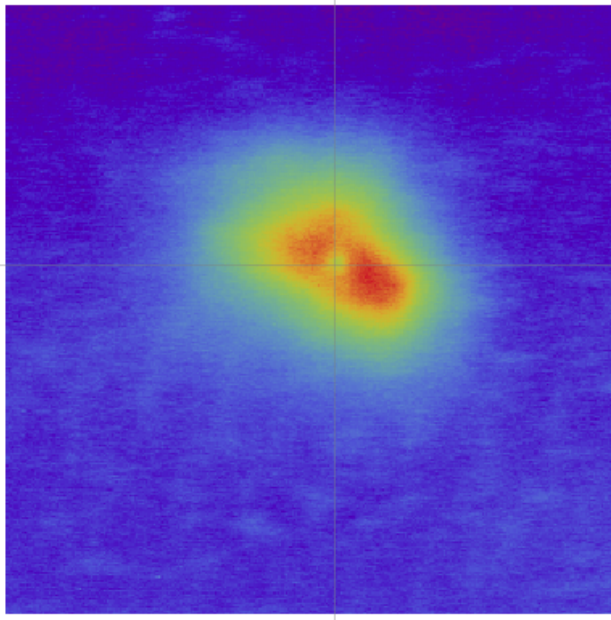


**Figure 3.5** False-color image of the "hole" in the MOT caused by the trapping beam.

"away" by the trapping beam, they are in reality still there but simply fluorescing more weakly. The magnitude of the shift is large enough that the atoms at the trap are shifted multiple linewidths further away from resonance, which causes them to scatter much less light than the other nearby atoms.

This visible "hole" in the MOT also serves as a very useful alignment tool for our setup, since our combined trapping and imaging optics means that it always remains in the same location on the CCD. Therefore, aligning the trap and MOT only requires moving the camera around on its translation stage until the trap spot overlaps the MOT.

### Polarizability Measurement

A measurement of the AC Stark shift experienced by atoms simultaneously in the MOT and trap beams allows us to measure the polarizability of holmium's ground state. This can be done in the following way, rewriting Eq. 3.2 using the properties of electric fields and Gaussian beams:

$$\Delta\omega' = -\frac{1}{4\hbar}\alpha|\mathcal{E}|^2 = -\frac{\alpha I_0}{2\hbar c\epsilon_0} = -\frac{\alpha}{\pi w^2 \hbar c \epsilon_0} P \quad (3.3)$$

where  $\alpha$  is the polarizability at the wavelength in question (532 nm),  $w$  is the radius of the trap beam,  $P$  is the power of the trap beam, and  $\hbar$ ,  $c$ , and  $\epsilon_0$  are all the typical familiar physical constants. The negative sign tells us we should expect the ground state to shift downward. In an ideal two-level system, the excited state of the transition should shift by the same amount but in the opposite direction, resulting in a total shift of twice this value. Previous spectroscopic data on holmium [32] suggests that there are no transitions from the ground state close enough to 532 nm to have any substantial effect, so viewing the system as approximately two-level should be acceptable for a ground state polarizability measurement.

In order to measure how strongly the atoms are being affected by the trap beam, we need to quantify the relationship between the observed MOT brightness and the brightness of the "hole" as observed in Figure 3.5. We use Eq. 3.1, but noting that we are very close to the 410.5 nm transition, only one term remains relevant in the sum. For all other transitions, the far detuning  $\Delta \gg \gamma$  means they together contribute a fractional change of  $\approx 10^{-4}$ . Now, we modify the expression by adding an additional detuning  $\Delta\omega'$  from Eq. 3.3:

$$r_{sc} = \frac{\gamma}{2} \frac{I_{MOT}/I_{sat}}{1 + 4/\gamma^2(\Delta - \Delta\omega')^2 + I_{MOT}/I_{sat}}$$

We still expect the shift to be linear with the intensity, so we let  $\Delta\omega' = kI_t$  where  $I_t$  is the intensity of the trapping light and  $k$  is a value which we can extract from fits applied to experimental data.  $I_t$  is a spatially-varying function, containing all the free parameters of a Gaussian laser beam which in this case are set to the values of the trap beam itself via other measurements we have taken.  $I_{MOT}$  is approximately constant over the volume of the MOT, which we can directly measure from the shape of the MOT beams. Finally we need to superimpose an overall density profile for the MOT, but this is well approximated by a simple Gaussian function. This results in a fitting function of

$$f = \frac{\gamma}{2} \frac{I_{MOT}/I_{sat}}{1 + 4/\gamma^2(\Delta - kI_t)^2 + I_{MOT}/I_{sat}} \cdot A \exp\left(-\left(\frac{r - r_0}{w}\right)^2\right)$$

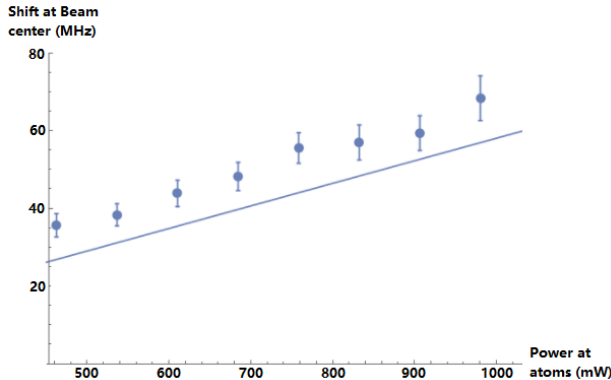


**Figure 3.6** Scaling of the AC Stark shift as a function of the trap beam power. The solid line is not a linear fit to the data, but rather an expected trend based on the calculated polarizability and treating the transition as an ideal two-level system.

where  $A$ ,  $r_0$ , and  $w$  are free parameters which are used to fit the MOT density profile appropriately. The last fitting parameter  $k$  is equal to  $\alpha/\hbar c \epsilon_0$  from our derivation, which allows us to fit a value for the measured polarizability.

Performing this fit gives us a value of  $57.9 \pm 4.5 \text{ \AA}^3$  for the ground state polarizability of holmium. This value is roughly 24% larger than the calculated polarizability of the ground state, which we think is due to the excited state having a larger polarizability (see Figure 3.6). Therefore, treating the transition between the two states as an ideal two-level system may not be a valid approximation.

### Chopped Trap Loading

Loading the atoms from a MOT into a FORT requires the atoms to be affected by both beams during the loading process. This is due to the fact that the force the atoms experience in a FORT is conservative, and therefore any atoms which are drawn towards the center of the trap will simply fall through the effective potential from the FORT and exit the other end with the same velocity it started with. Having the MOT beams active during loading provides a non-conservative drag force to remove any energy gained by the atoms being accelerated toward the center of the trap.

In order to get around the effects of the AC Stark Effect, we load the FORT by modulating

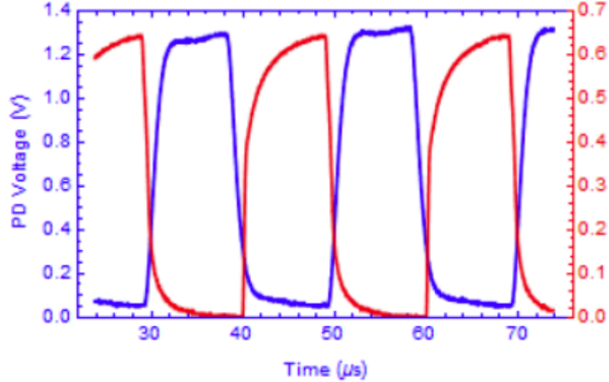


**Figure 3.7** Measured power of the MOT (blue) and FORT (red) beams from pick-off photodiodes during the chopping sequence. The finite rise time of the switching AOMs limits how quickly we can chop the beams.

the powers of the MOT and FORT lasers such that the atoms were never illuminated by both beams simultaneously. The dynamics of the atoms during this chopped loading is a repeated alternating sequence of being sped up as the trap beam pulls them to the center, followed being cooled down by the optical molasses force given by the MOT beams. This allows the MOT beams to remove some of the kinetic energy gained by atoms as they are drawn toward the center of the trapping potential, without being shifted too far away from resonance to be effective, eventually resulting in the atoms at the center of the trap but without significant additional energy gained from going to a lower potential.

## 3.5 Trap Frequency Measurements

### 3.5.1 FORT Trap Frequency

The bottom of the effective potential created by our FORT beam can be well-approximated by a harmonic oscillator through a series expansion of the effective potential the atom sees due to the AC Stark effect. The potential an atom in a red-detuned optical dipole trap formed by a focused beam is the same in any direction perpendicular to the beam's propagation direction,

$$\begin{aligned}
U &= -\frac{1}{4}\alpha|\mathcal{E}|^2 \\
&= -\frac{\alpha}{2\epsilon_0 c} I \\
&= -\frac{\alpha}{2\epsilon_0 c} I_0 \exp\left(-\frac{2r^2}{w^2}\right) \\
&= -\frac{\alpha}{2\epsilon_0 c} \frac{2P}{\pi w^2} \exp\left(-\frac{2r^2}{w^2}\right) \\
&= -\frac{\alpha}{2\epsilon_0 c} \frac{2P}{\pi w^2} \left(1 - \frac{2r^2}{w^2} + \frac{1}{2} \left(\frac{2r^2}{w^2}\right)^2 - \dots\right) \\
&\approx -\frac{\alpha}{2\epsilon_0 c} \frac{2P}{\pi w^2} \left(1 - \frac{2r^2}{w^2}\right) \\
U &= U_0 + \frac{2P\alpha}{\pi\epsilon_0 c w^4} r^2
\end{aligned}$$

from which we define the resonance frequency

$$\omega_0 = \sqrt{\frac{4P\alpha}{\pi m \epsilon_0 c w^4}}$$

in analogy to a quantum harmonic oscillator. The potential along the direction of beam propagation has a similarly defined value as well, which we can derive in a similar way to arrive at

$$\omega_0 = \sqrt{\frac{2P\alpha\lambda^2}{m\pi^3\epsilon_0 c w^6}}$$

These are both measurable in experimental setups and allow for another method to measure the atomic polarizability.

### 3.5.2 Parametric Heating Model

The typical way to measure the trap frequency  $\omega_0$  is to modulate the depth of the potential at some specified frequency  $\omega$ , and to observe the loss of atoms from the trap as a function of this frequency. When the modulation occurs at  $\omega = 2\omega_0$ , the initial kinetic energy of the atoms grows approximately exponentially until they are in the regime where the harmonic

potential is no longer a good approximation [48]. Thus, we expect to see the maximum atom loss at a modulation frequency equal to twice the trap frequency.

Due to limitations of the AOM which we use to switch the trap beam on and off and our control hardware, we are unable to perform the ideal long-duration small-amplitude sinusoidal modulation in order to heat the atoms out of the trap. Instead, our intensity modulation more closely resembles a square wave.

This should have approximately the same effect as a sinusoidal modulation as we can consider decomposing the square wave into its Fourier series, the higher harmonics of which should have a negligible effect on heating the atoms. In order to verify if this approach was accurate, we ran some simulations using our specific chopping intensity profile.

The simulation was done classically with no considerations for quantum behavior, which we think should be valid considering that all references to  $\hbar$  cancel out in the theoretical analysis [48]. We only considered the motion of individual atoms, neglecting collisional effects as our measured two-body loss coefficient suggests that they should be negligible at this time scale.

Our simulation initialized atoms with a specific starting velocity in a random direction corresponding to the temperature parameter, modulated the trap according to our experimental intensity profile for 100 ms, and then classified any particles which were more than 10 times the beam waist in any dimension as lost. For various chopping conditions and atom temperatures, we were able to produce plots showing under what conditions atoms are lost from the trap (see Figure 3.8). The parameters of our simulation were scaled to be dimensionless for particle energy (1 mK corresponding to the full depth) and modulation depth (0 corresponding to no modulation and 1 corresponding to a full on-off intensity profile).

The result of the simulation was that we should expect maximum atom loss at a modulation frequency only roughly 1.6 to 1.7 times the actual trap frequency, not at the expected doubled frequency. We suspect that this is because our chopping parameters may cause a non-negligible drop in the average trap depth, which effectively lowers the trap frequency below its value at full trap power.

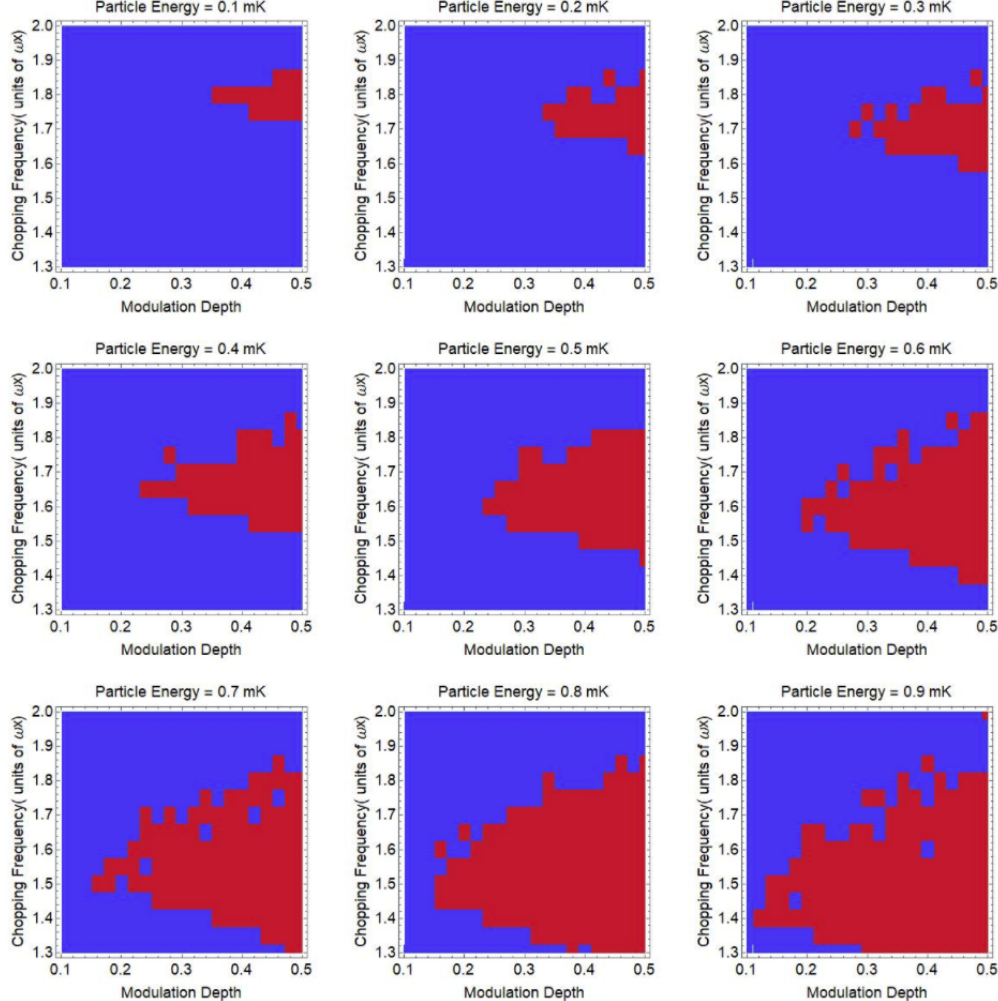


**Figure 3.8** Plots showing results of our simulations for our square-wave trap modulation. Blue cells correspond to the atom staying in the trap, and red cells correspond to atoms being lost from the trap after the modulation. Atoms appear to be lost more readily at modulation frequencies which are less than the theoretical factor of 2 larger than the trap frequency.

### 3.5.3 Radial and Longitudinal Trap Frequencies

Our focused-beam ODT has azimuthal symmetry, which gives us two distinct trap frequencies based on which axis we are considering. We measured the two different trap frequencies in two different ways, due to how our experiment is set up.

The radial frequency was measured using the method described above - we modulated the depth of the trap at various frequencies and observed the atom loss as a function of the modulation frequency.

The longitudinal frequency is harder to measure in our configuration, as its corresponding axis is perpendicular to our trap imaging plane. Additionally, the shape of a focused Gaussian beam means that this frequency is also much lower than the radial frequency. We made measurements to observe it by dropping the trap very briefly in order to excite a breathing mode in the trap along that axis. As the atoms move in and out of focus in our images, a sinusoidal dependence of brightness as a function of time since the excitation should have been seen [49], but unfortunately we never observed such a trend ourselves due to instability of our experimental setup over the span of a single experiment (roughly 20-30 minutes).

### 3.5.4 Tensor Shift Effects

Since no optical pumping has been done, the atoms in the ODT are in a mixture of  $m_F$  states. The different  $m_F$  states have slightly different atomic polarizabilities, as the total polarizability is based on both the scalar polarizability  $\alpha_0$  and the tensor polarizability  $\alpha_2$  with a state-dependent prefactor. Assuming linearly-polarized light, we have a total polarizability of

$$\alpha = \alpha_0 + C(F, M_F)\alpha_2$$

where

$$C(F, M_F) = \frac{[3M_F^2 - F(F+1)][3X(X-1) - 4F(F+1)J(J+1)]}{F(2F-1)(2F+2)(2F+3)J(2J-1)}$$

and  $X = F(F+1) + J(J+1) - I(I+1)$ , with  $F$ ,  $I$ , and  $J$  being the typical quantum

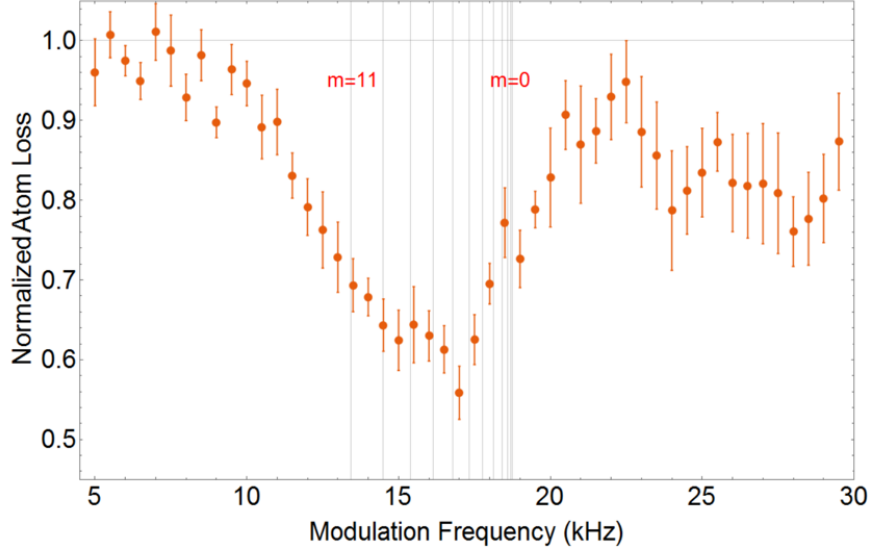


**Figure 3.9** Atom loss from the trap when modulated at various frequencies, with an overlay of calculated trap frequencies for separate  $m_F$  levels in the  $F = 11$  set of states.

numbers associated with various atomic angular momenta. The state-dependent polarizability leads to the different states experiencing different trapping potentials, and therefore also having different trap frequencies. This effectively amounts to a broadening in the dip observed in the trap modulation, shown in Figure 3.9.

## 3.6 Atom Loss Mechanisms

### 3.6.1 Atom Temperature

The depth of our trap is 1.70 mK at maximum power, while the Doppler temperature of the broad MOT is  $780 \mu K$ . The actual atom temperature tends to be significantly lower due to additional sub-Doppler cooling mechanisms [50]. Our best estimate of the actual MOT temperature is  $150 \mu K$ , which was measured by modeling the cloud using a model of free ballistic expansion (see Appendix C).

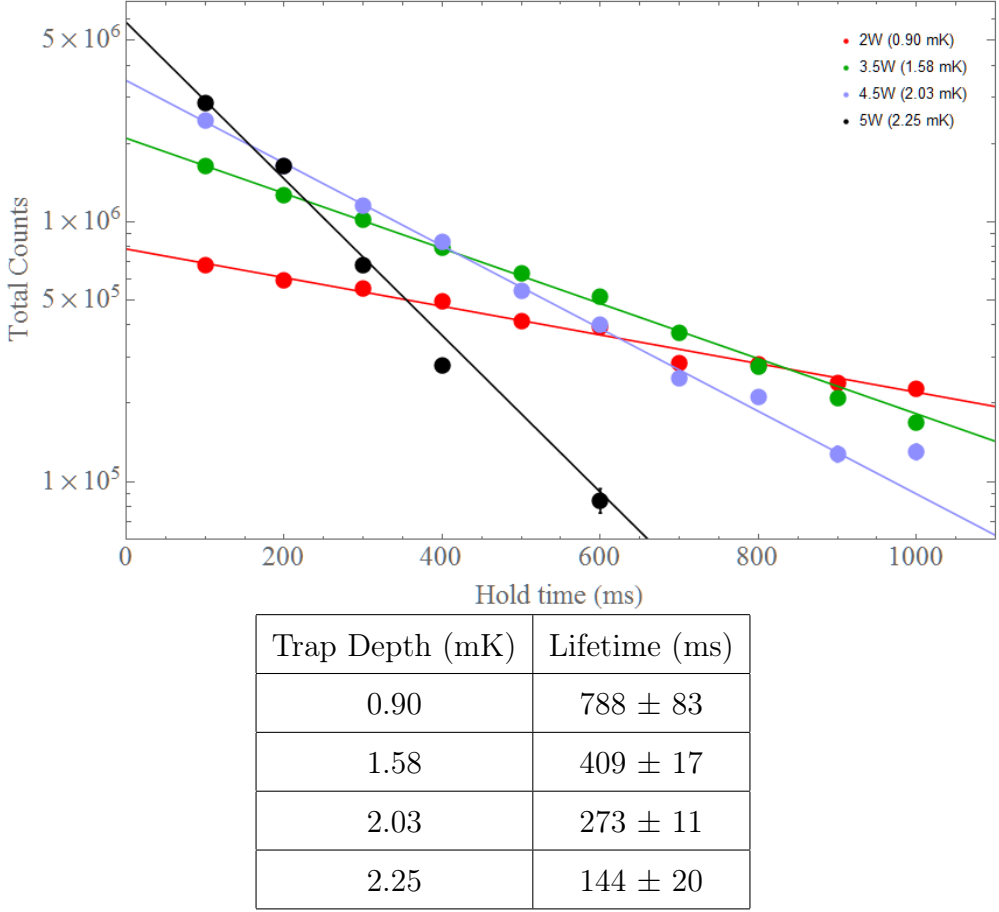


**Figure 3.10** Trap population decay over time for various trap powers. The shallower, low-power traps start out with less atoms, but the atoms have a longer decay time.

### 3.6.2 Dependence on Trap Power

Experimentally we initially observed that the trap has a longer lifetime with lower trap powers, but this may be an artefact of the limited chopping speed we can use during the trap loading and readout. Initial measurements on our trap showed a strong dependence of the lifetime on the trapping power, with the lifetime ranging from 788 ms at a trap depth of 0.9 mK to only 144 ms with a deeper 2.25 mK trap (see Figure 3.10).

After some experimental improvements, most notably an increase in our chopping speed from 50 kHz to 250 kHz, we took another measurement of this dependence and found that the trend was much weaker (see Figure 3.11). We are unsure about the mechanism which is

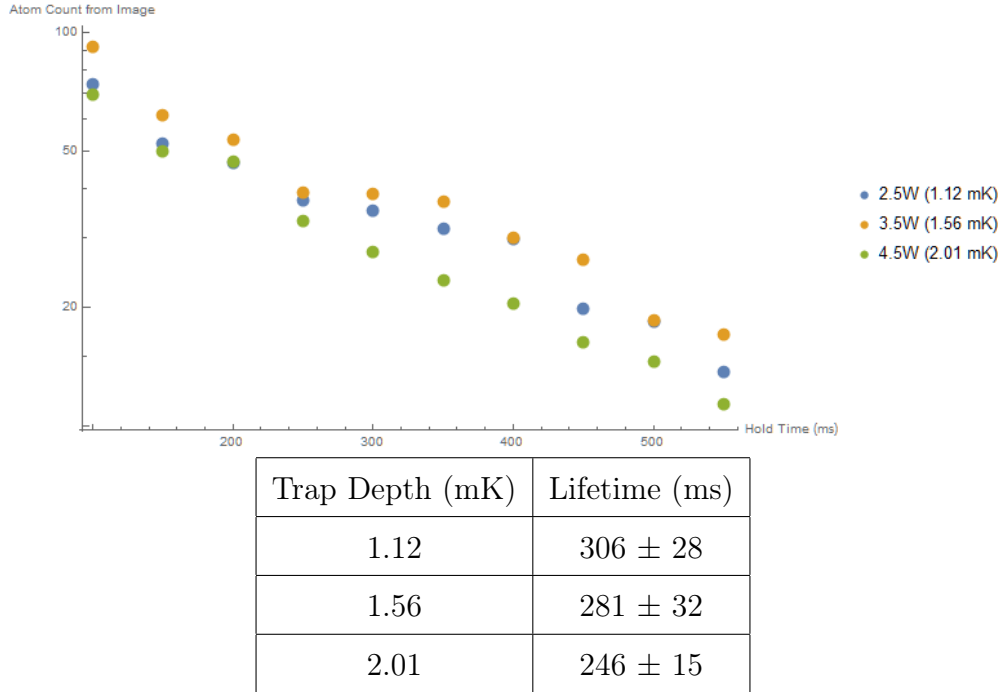


**Figure 3.11** Trap population decay over time for various trap powers after some experimental improvements.

causing this, but suspect it might be due to collisions between the atoms within the trap.

### Trap Beam Heating

While the trapping beam primarily serves the purpose of creating an effective potential minimum which holds the cold atoms, it still scatters a nonzero number of photons off the atoms. Over time and many scattering events, this gradually gives energy to the trapped atoms and leads to a temperature change of

$$\Delta T(t) = \frac{(\hbar k)^2}{2k_b m} \cdot r_{sc}$$

In the limit of far detuning from all transitions, the scattering rate is linear with intensity and therefore linear with trap depth:

$$\Delta T(t) = \frac{(\hbar k)^2}{2k_b m} \sum \frac{\gamma}{2} \frac{I}{I_{sat}} \frac{\gamma^2}{4\Delta^2}$$

At 532 nm, the scattering rate of photons from the trap beam is  $37.33 \text{ s}^{-1}$  per Watt of trap beam power. Using the rest of our experimental parameters, we expect a heating rate of approximately  $7.66 \mu\text{K}/\text{s}$  per Watt, which is much smaller than both the trap depth and the kinetic temperature of the atoms. Thus heating from the trap beam should not be a factor for even the longest-lived traps we have observed, which have lifetimes on the order of a second.

### Collisional Losses

In order to make our model more accurately reflect the trap's behavior, we can model the atom count in the trap with the following differential equation, with terms for single-body loss (leading to the typical exponential decay) and two-body loss from collisional effects [51]

$$\frac{dN}{dt} = -\alpha N - \beta N^2$$

where  $\alpha$  and  $\beta$  are one-body and two-body loss coefficients, respectively.  $\alpha$  primarily depends on collisions with background atoms in the vacuum chamber if only the trapping light is present, as dipole trap beams are typically chosen such that the scattering from the trap light itself is relatively minimal. The two-body loss  $\beta$  scaling with  $N^2$  reflects the fact that higher densities lead to more loss based on atom-atom collisions.

The atoms within the trap cannot exchange enough energy through linear momentum transfer alone to be lost from the trap, especially if the trap is sufficiently deep. Instead what is occurring during these collisions is that there is a transfer of angular momentum which makes one of the atoms drop from the  $F = 11$  hyperfine state to  $F = 10$ , emitting a photon of 8.28 GHz in the process. Considering the commonly-used figure of  $20 \text{ MHz} \approx 1 \text{ mK}$ , this photon contains about three orders of magnitude more energy than our trap is capable of holding; any atoms it interacts with will be certainly lost from the trap.

As two-body losses depend on the density of the atom cloud and have been observed to scale linearly with laser intensity [51], we took measurements of the trap at various powers to try to measure a two-body loss coefficient to characterize the degree these hyperfine-changing collisions were occurring. However, we saw what appeared to be the opposite of

Trap Power	Trap Depth	Single Exponential Fit	Two-body Loss Model	
		$\alpha (s^{-1})$	$\alpha (s^{-1})$	$\beta (s^{-1})$
2 W	450 $\mu$ K	19.8 $\pm$ 2.4	8.42 $\pm$ 2.10	55.7 $\pm$ 7.4
2.5 W	560 $\mu$ K	19.5 $\pm$ 1.3	12.9 $\pm$ 0.9	32.0 $\pm$ 3.1
3 W	670 $\mu$ K	21.1 $\pm$ 1.2	8.42 $\pm$ 2.10	27.2 $\pm$ 4.2

**Table 3.2** Table of fitted values for loss coefficients in the loss models we considered.

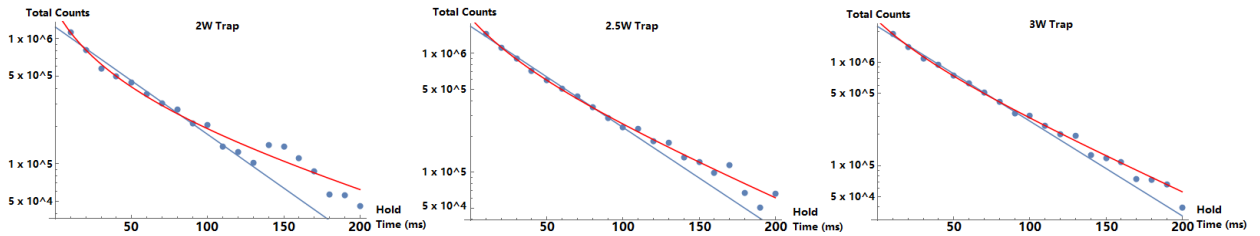


**Figure 3.12** Loss curves from the dipole trap with different trap power settings.

The blue curves are a single-body loss model which is a simple exponential decay, while the red curve is the two-body loss model. The data indicate that the two-body loss seems to be higher at lower power.

the expected trend - that deeper traps and correspondingly denser atom clouds seemed to have lower two-body loss coefficients.

### 3.7 Conclusion

In this chapter we have shown the first successful holmium optical dipole trap and have taken steps towards measuring some of its atomic properties using the trap. We have additionally examined some collisional properties of holmium within the dipole trap, although the results were inconclusive. The dipole trap is an important first step towards using cold holmium atoms for further experiments, as it allows for tighter localization of a small number of very cold atoms than a MOT allows.

# Chapter Four

## Narrow Line Transition

In order to produce colder atoms, we had to characterize another nearby, narrower transition to the 410.5 nm MOT transition. The chosen transition is one at 412 nm, with electron configurations  $4f^{11}(4I^\circ)6s^2$  ( $J = 15/2$ ) to  $4f^{10}(5I^\circ)5d^2(3P)(7H)6s$  ( $J = 17/2$ ), which has an energy gap of  $24263.96\text{ cm}^{-1}$ . As can be seen from the electron configurations, this is actually a two-electron transition where a  $6s$  and  $4f$  electron are excited together to  $5d^2$ . Therefore, this transition would be classically forbidden as a single-photon transition. Due to the very high degree of state mixing within holmium's energy levels, it is nonetheless actually possible to excite this transition with a single, monochromatic source.

This narrower 412 nm line is not very well-studied, with relatively very few prior references compared to more commonly studied atoms [32][52][53]. In this chapter, we discuss the measurements we have taken to characterize the relevant properties of this transition, namely the properties of the excited state as the ground-state properties are generally much more well-understood. In the first section, we give a brief derivation of the hyperfine interaction and construct a model for our data. In the second section, we outline the particular configuration for our saturated absorption spectroscopy on this transition. In the third section, we discuss the process of fitting the hyperfine constants to the data we have taken. Characterizing this transition opens up the possibility of using it for a second stage of cooling within a MOT, which is discussed in more detail in the end of this chapter.

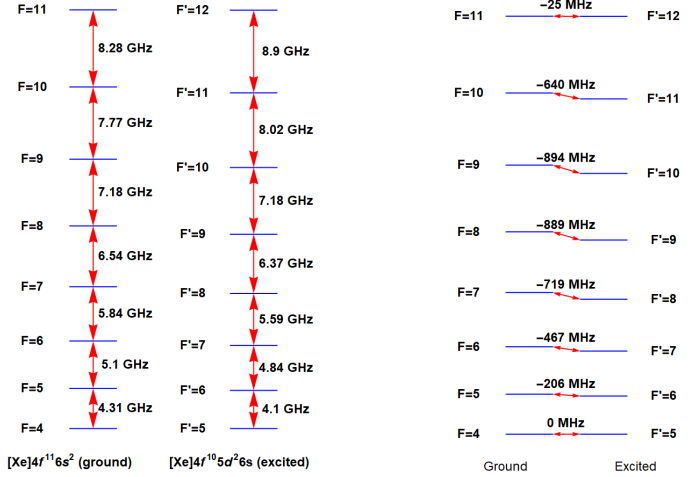


**Figure 4.1** Energy gaps between successive hyperfine states (left) for the ground state and excited states for the 412 nm line. The relative gaps between states based on a set of  $F \rightarrow F' = F + 1$  transitions is also shown (right), showing the nontrivial mapping between the order of the spectroscopy peaks and the hyperfine states. The ground state values were calculated from previous literature [54] while the excited state values are our measurements.

## 4.1 Hyperfine Structure

The interaction between the angular momentum of the electrons in the partially-filled  $4f^{11}$  shell and the angular momentum of the atomic nucleus leads to a splitting of energy levels based on the relative orientations of the two angular momenta. This interaction leads to the non-degenerate energy levels which comprise an atom's hyperfine structure.

### 4.1.1 Mathematical model

The Hamiltonian for the hyperfine interaction can be written as a sum of spherical tensor operators:

$$\mathcal{H}_{hfs} = \sum_k \mathbf{T}^{(k)} \cdot \mathbf{M}^{(k)}$$

where  $\mathbf{T}^{(k)}$  and  $\mathbf{M}^{(k)}$  are spherical tensor operators of rank  $k$ , each representing the electronic and nuclear parts of the hyperfine interaction. The  $k = 0$  term is the interaction

between the spherical part of the nuclear charge and the electric field, which is neglected here as it shifts all hyperfine levels equally. The  $k = 1$  term represents the coupling between the nuclear magnetic moment and the magnetic field produced by the electrons. We examine this part first using the states  $|I, J, F, m_F\rangle$ , which are eigenstates to first order. Thus, the energies of the states are given by

$$\begin{aligned} U_1 &= \langle I, J, F, m_F | \mathbf{T}^{(1)} \cdot \mathbf{M}^{(1)} | I, J, F, m_F \rangle \\ &= (-1)^{I+J+F} \left\{ \begin{matrix} I & J & F \\ J & I & 1 \end{matrix} \right\} \cdot \langle I || \mathbf{M}^{(1)} || I \rangle \cdot \langle J || \mathbf{T}^{(1)} || J \rangle. \end{aligned}$$

where the numbers in brackets are Wigner 6-j symbols. If we introduce the hyperfine constant  $A$  with the definition

$$A = g_I \mu_N \frac{\langle J || \mathbf{T}^{(1)} || J \rangle}{\sqrt{J(J+1)(2J+1)}} = \frac{\langle I || \mathbf{M}^{(1)} || I \rangle}{\sqrt{I(I+1)(2I+1)}} \frac{\langle J || \mathbf{T}^{(1)} || J \rangle}{\sqrt{J(J+1)(2J+1)}}$$

and  $K = \frac{1}{2}\mathbf{I} \cdot \mathbf{J} = F(F+1) - I(I+1) - J(J+1)$ , then we can rewrite the hyperfine energy shifts as follows:

$$U_1 = A(-1)^{I+J+F} \left\{ \begin{matrix} I & J & F \\ J & I & 1 \end{matrix} \right\} \sqrt{I(I+1)(2I+1)} \sqrt{J(J+1)(2J+1)} = A \frac{K}{2}.$$

The  $k = 2$  term is the electric quadrupole hyperfine constant  $B$ , defined as

$$B = 2eQ \left( \frac{2J(J-1)}{(2J+1)(2J+2)(2J+3)} \right)^{\frac{1}{2}} \langle J || \mathbf{T}^{(2)} || J \rangle$$

where  $Q$  is the nuclear quadrupole moment defined by

$$Q = \frac{2}{e} \left\{ \begin{matrix} I & 2 & I \\ -I & 0 & I \end{matrix} \right\} \langle I || \mathbf{M}^{(2)} || I \rangle.$$

From this, we can write out the energy shifts due to the electric quadrupole interaction:

$$U_2 = B \frac{\frac{3}{2} \mathbf{I} \cdot \mathbf{J} (2\mathbf{I} \cdot \mathbf{J} + 1) - \mathbf{I}^2 \mathbf{J}^2}{2I(2I-1)J(2J-1)}.$$

Lastly, we can use the definition of  $K$  above to write out the energy shifts due to both the magnetic dipole and electric quadrupole interactions in the same expression:

$$H = U_1 + U_2 = \frac{1}{2} AK + B \frac{3K(K+1) - 4I(I+1)J(J+1)}{8I(2I-1)J(2J-1)}.$$

These two constants are both related to the atom's internal structure and also measurable parameters in a lab. There are higher-order N-pole interactions corresponding to higher-rank tensors as well, but these are smaller by ever-increasing powers of the fine structure constant  $\alpha \approx \frac{1}{137}$  and thus not experimentally relevant in many cases.

#### 4.1.2 Constructing an analytic function to fit

Assuming that transitions follow the selection rule of  $F \rightarrow F' + 1$ , a theoretical saturated absorption signal would contain 8 separate peaks for the 412 nm transition we are interested in - one peak for each hyperfine level. Each of these transitions have slightly different relative strengths, which can be quantified by the relative magnitude of their dipole matrix elements. We can relate all the matrix elements together to the reduced matrix element via a Wigner 6j symbol:

$$\langle I, J', F' | \hat{d} | I, J, F \rangle = (-1)^{1+I+J'+F} \sqrt{(2F+1)(2F'+1)} \left\{ \begin{matrix} J & I & F' \\ F' & 1 & J' \end{matrix} \right\} \langle J' || \hat{d} || J \rangle$$

so the relative strengths of the transitions are simply the squares of the above coefficient to the reduced matrix element. This corresponds to a height and linewidth proportional to the transition probability, which is the matrix element squared. The values of A and B simply move the locations of the peaks relative to each other in frequency space.

The lineshape of each transition itself follows a Lorentzian profile, which means that the analytic function being used to fit the data has for form

$$I(\omega) = \sum_{F=4}^{11} \frac{2}{\pi\gamma(F)} \frac{I_0}{1 + \left(\frac{2(\omega - \omega_0(F))}{\gamma(F)}\right)^2}$$

where  $\omega_0(F)$  is the frequency of the transition between the hyperfine levels  $F$  and  $F' = F + 1$  (which depends on the hyperfine coefficients), and

$$\gamma(F) = (2F + 1)(2F' + 1) \left( \begin{Bmatrix} J & I & F' \\ F' & 1 & J' \end{Bmatrix} \right)^2 \gamma_0$$

is the state-dependent linewidth scaled using the same prefactor from above.

There are additional sets of transitions for  $F \rightarrow F'$  and  $F \rightarrow F' - 1$ , but they are 4-8 GHz away while the spectrum itself only spans a range of 0.8 GHz. Additionally, their matrix elements are smaller on average by a factor of 12.2 and 539 respectively - well below the noise floor of our measurement hardware.

## 4.2 Saturated Absorption Spectroscopy

Due to the aforementioned low vapor pressure and high melting point of holmium, we use a hollow cathode lamp to produce the free holmium atoms required for the spectroscopy. The hollow cathode lamp we use is a Hamamatsu L2783, which operates at up to a maximum voltage of 1 kV and current of 10 mA to produce a holmium discharge plasma. At this temperature Doppler broadening is very significant, with the full-width half-maximum of the Doppler-broadened curve being on the order of a few GHz, given by the following expression

$$\Delta f_{FWHM} = \sqrt{\frac{8k_B T \log 2}{mc^2}} f_0$$

As the measured spectrum was expected to span roughly 1 GHz based on rough previously-measured values [32], directly measuring atomic absorption from transmission through the cathode cell is infeasible. Instead, we measured the spectrum of the 412 nm transmission using Doppler-free saturated absorption spectroscopy [55].

We tuned our primary Ti:Sa laser over to 412 nm to produce the light for the spectroscopy, as it is capable of producing more power at a narrower linewidth than the system we built in-house. The Ti:Sa laser was then referenced to a ULE cavity for a precise frequency reference

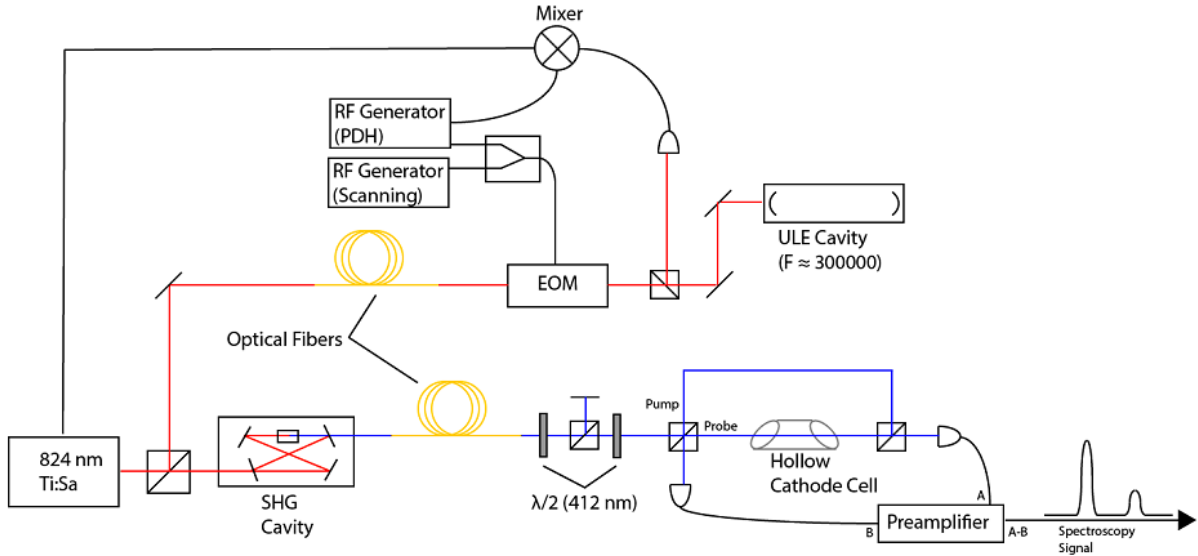


**Figure 4.2** Schematic of the optical setup we used for measuring the 412 nm spectrum.

on the locations of absorption peaks (see Appendix D). Since our signal was very small, the absorption from the pump and probe photodiode signals were sent to a Stanford Research Systems SR560 low-noise pre-amplifier to be subtracted and then subsequently amplified before measurement.

The experimental setup near the hollow cathode cell itself is a relatively standard saturated absorption spectroscopy setup (see Figure 4.2), where the atomic sample is in the center of a glass cell and two counter-propagating laser beams ensure that the atomic population which is being measured is one such that the Doppler shift from thermal motion is minimized. There are additional half waveplates and a polarizing beam splitter in order to control the relative powers of the pump and probe beams. The relevant experimental parameters to produce the spectroscopic data were the following:

- Pump beam:  $w = 4.02, 3.45 \text{ mm}$ ,  $P = 41 \text{ mW}$ ,  $I/I_{sat} = 5.25$
  - Probe beam:  $w = 4.63, 3.48 \text{ mm}$ ,  $P = 2.5 \text{ mW}$ ,  $I/I_{sat} = 0.30$
  - Preamp filter settings: Band-pass filter from 10 Hz to 10 kHz, 6 dB/8ve roll-off

- Sampling: Laser ramp speed 25 Hz, 20 seconds measurement time, 500 ramps per run
- Frequency: Measured relative to the ULE cavity peak at 363.7080 THz pre-SHG (doubled: 727.416 THz)
- Cathode cell: 5 mA at 250 V

### 4.3 Fitting Hyperfine Constants

When fitting a theoretical absorption spectrum to an experimentally-measured one, a simple least-squares fit between the two curves does not suffice. This is because the peaks are relatively narrow compared to the frequency span of the entire spectrum, which may result in the fitting process weighing the behavior of the curves between the peaks too strongly and not fitting the actual peaks properly.

In order to fit the curve, we must introduce a few more parameters in order to properly match the scale of the theory curve and the measured data. There is a vertical scaling factor, as well as a horizontal shift. Along with the transition linewidth and the two hyperfine coefficients this gives us five parameters, three of which are physically interesting and two of which are experimental artifacts.

The fitting process becomes less straightforward when looking at experimental data since instead of the expected 8 peaks, only 6 clear peaks are observed. With sufficiently high resolution, one of the peaks appears as though it is actually two separate but closely-spaced peaks. This hints at why we observe fewer peaks; some of the peaks in the experimental data actually consist of multiple peaks too closely-spaced to be separately resolvable. There are multiple ways to choose the peak degeneracy, so we performed the fitting routine with every reasonable pairing and then chose the pairing which resulted in the best overall fit.

Depending on how we "choose" which peaks are degenerate, we can end up with the first hyperfine constant A changing by up to 10 MHz as well as producing qualitatively different looking spectra both in peak spacing and relative height. Luckily, as the hyperfine constants have been measured previously, we have a decent initial value to start at for an iterative least-squares fitting process.

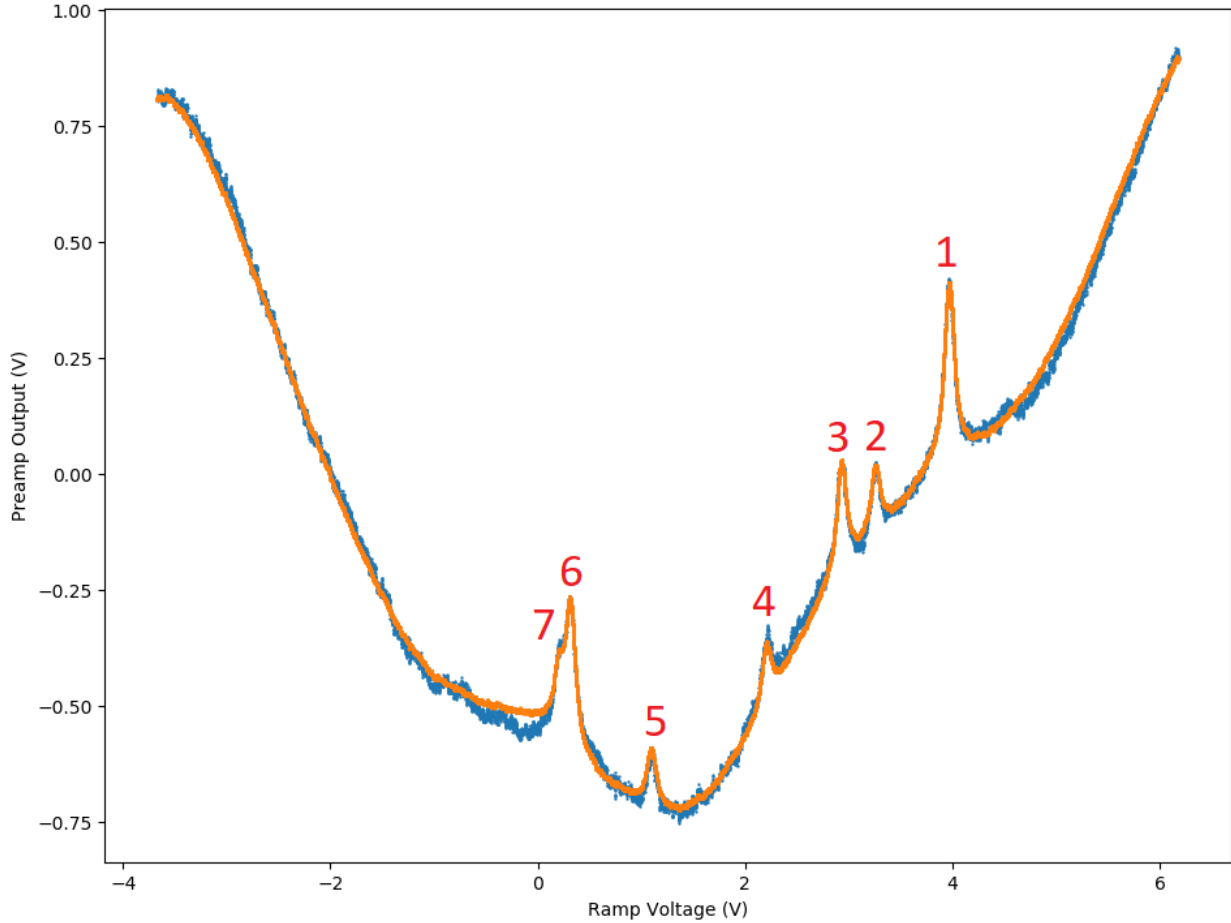


**Figure 4.3** Sample data set where we indicate the peak indexing for our data table containing measured transition frequencies. The blue trace is the raw data from a single sweep, and the orange trace is an average of 13 separate sweeps after some data filtering which rejects scans with signs of clear laser instability.

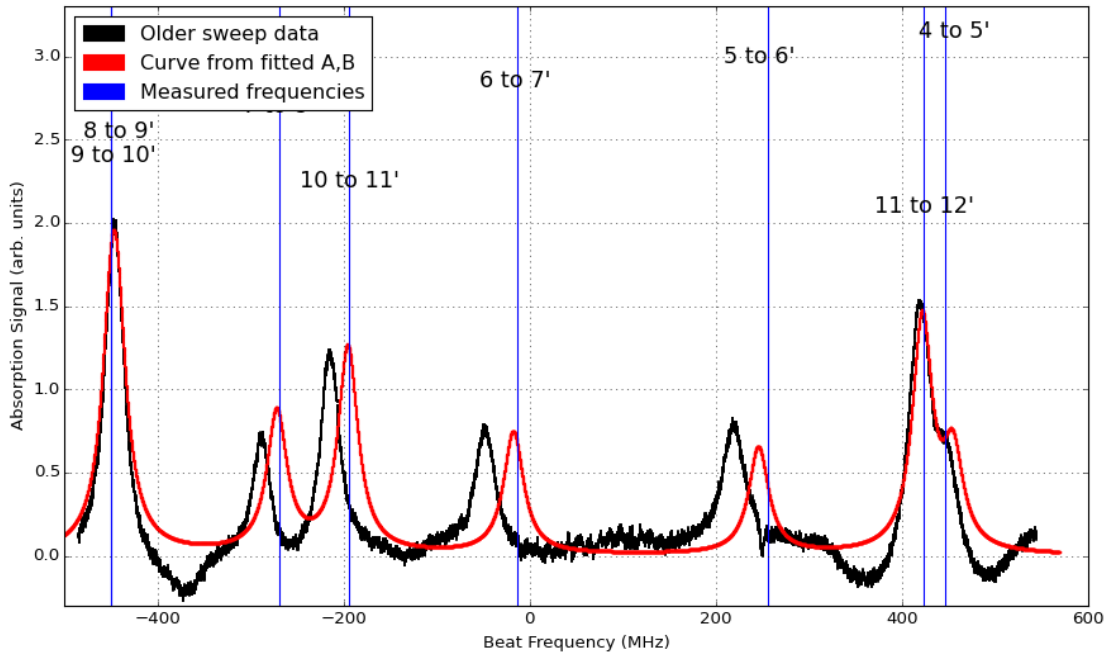


**Figure 4.4** Plot of an average of a few hundred scans of the spectrum (black), with measured reference frequencies (blue) overlaid. The nonlinear relationship between the voltage sent to the laser and the actual frequency results in the blue lines not coinciding with where the black peaks are. The red curve is a theoretically calculated spectrum based on the fit to the blue frequencies, which we expect are more free of systematic errors than the black trace. This figure also shows that the predicted heights based on relative matrix elements are approximately correct as well.

Instead of fitting a theoretical curve to the entire measured spectrum, we extract the measured frequencies of the peaks using our ULE frequency reference (see Appendix D). This is mostly due to an observed systematic mismatch between the voltage sent to the laser and the actual frequency the laser outputs, leading to nonlinear behavior despite a linear voltage ramp.

The frequency reference allows us to determine the relative spacing between the peaks. The fitting process we used, with a gradient descent method, is as follows:

- Use the current values of the hyperfine A and B coefficients to produce a set of frequencies where peaks are expected.
- Find the optimal frequency shift which, when applied to all elements of this set of frequencies, minimizes the total mean-squared error between this set and corresponding measured frequencies.
- Calculate the total mean-squared error for some nearby values of A and B to estimate a gradient for the cost function, which here is equal to the total mean-squared value.
- Change the current values of A and B in accordance with the magnitude and direction of the calculated gradient.
- Repeat until convergence.

The code used for this analysis is available on <https://github.com/cyip92/sat-abs-holmium> and <https://github.com/QuantumQuadrate/HolmiumCode>.

We measured values of  $A = 715.85 \pm 0.09$  MHz and  $B = 1015 \pm 9$  MHz for the two hyperfine coefficients. The linewidth of the transition allows us to determine an effective minimum uncertainty in the least-squares fit, which we calculated by assuming that the measured frequencies have independent and normally-distributed errors with uncertainty equal to the linewidth. Combining these errors in quadrature gives an expected minimum fitting error of  $15.0$  MHz $^2$ , not much lower than the  $17.8$  MHz $^2$  found in our data. To determine the uncertainty in our fit, we examine the fitted mean-squared error in the neighborhood of the point to which the gradient descent method converged. The uncertainty is calculated based

Peak index	Meas. Freq. (MHz)	$F \rightarrow F'$	Fit Freq. (MHz)	Fit Linewidth (MHz)
1	$801.90 \pm 0.28$	$8 \rightarrow 9'$	802.97	$6.13 \pm 0.28$
		$9 \rightarrow 10'$	800.49	
2	$715.63 \pm 0.38$	$7 \rightarrow 8'$	715.42	$5.85 \pm 0.86$
3	$675.40 \pm 0.36$	$10 \rightarrow 11'$	676.22	$6.73 \pm 0.79$
4	$589.21 \pm 0.26$	$6 \rightarrow 7'$	589.39	$5.17 \pm 0.50$
5	$458.65 \pm 0.36$	$5 \rightarrow 6'$	459.02	$6.33 \pm 0.76$
6	$369.27 \pm 0.248$	$11 \rightarrow 12'$	368.61	$5.37 \pm 0.50$
7	$356.11 \pm 1.27$	$4 \rightarrow 5'$	355.95	$12.93 \pm 1.93$

**Table 4.1** Measured and fitted frequencies for the different hyperfine transitions on the 412 nm line. Linewidths were fitted by closely measuring each peak individually, and thus deviate slightly from the expected ratios based on matrix elements.

on how much the hyperfine values would need to change in order to quadruple the total mean-squared error, corresponding to an average of all the fitted values being twice as far away from their best fit values.

## 4.4 Narrow-line Cooling

This 412 nm transition has many properties which make it desirable to study and use over the broad 410 nm line in our experiment. In particular, it may provide us with cooler atoms within our MOT.

### 4.4.1 Advantages

This transition has a much narrower linewidth of  $\gamma/2\pi = 2.3$  MHz, corresponding to a much lower Doppler cooling limit of  $56 \mu K$  (to be contrasted with the MOT transition's 32.5 MHz and  $780 \mu K$ , respectively). This is particularly relevant for us as our current relatively high atom temperature appears to be one of our main limiting factors for progress.

The same optics can be used for both beams since the wavelength difference is small

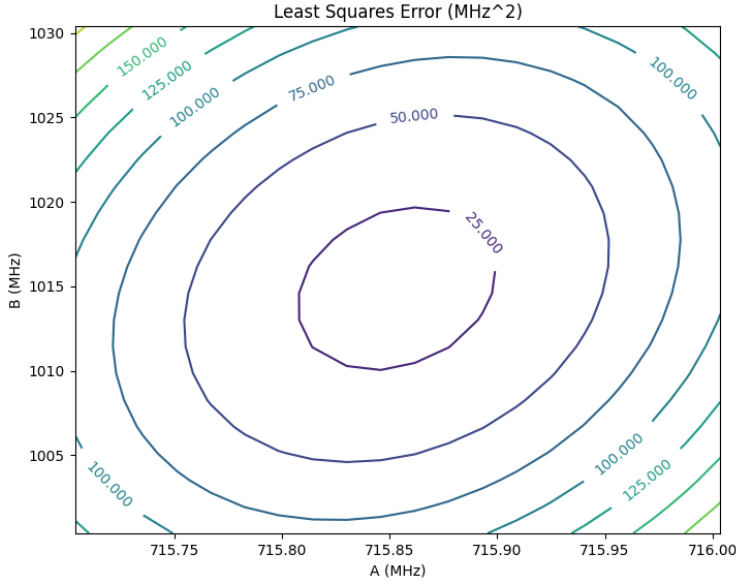


**Figure 4.5** Value of the least-squares error metric near the fitted hyperfine constants. The cited errors are the values of the hyperfine constants at which the error increases to quadruple of its minimal value.

enough to be irrelevant. Thorlabs E02 dielectric mirrors have  $>99.7\%$  reflectance, differing by less than 0.1% between 410.5 nm and 412 nm. The waveplates we use from Tower Optical can be used in  $410 \pm 2$  nm, which covers both beams.

#### 4.4.2 Disadvantages

It is likely that the 412 nm does not have the same self-repumping property as the 410.5 nm line, due to the different hyperfine constants in the excited state and the much narrower linewidth. The  $10 \rightarrow 11'$  line is 310 MHz away from the  $11 \rightarrow 12'$  line we would use to form the MOT (Figure 4.1), which means that the repump transition is shifted more than a hundred linewidths blue instead of only 18.7 linewidths red in the broad 410.5 nm MOT. For a hypothetical case of forming a MOT with a detuning of 5 MHz from the narrow transition, the relative off-resonant repumping rate compared to the broad transition is a factor of 50 smaller. This suggests that unlike the broad MOT transition, we may need an additional repumping beam for a MOT formed on this transition.

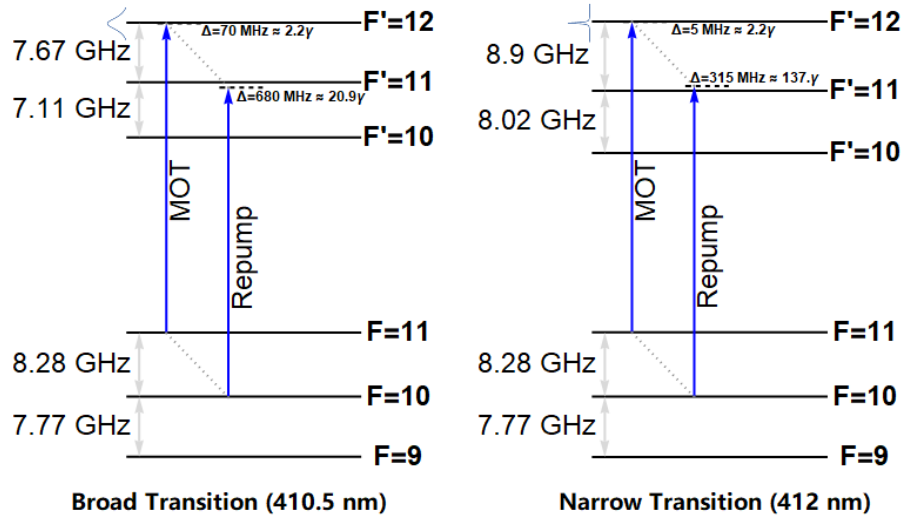


**Figure 4.6** Energy level diagram examining potential self-repumping on the broad and narrow transitions, not necessarily to scale. The narrow transition is only half as far away from resonance in terms of absolute frequency, but is seven times farther away in terms of linewidths.

Using the parameters for the 412 nm transition in our slowing simulations shows that slowing on the narrow transition is almost entirely ineffective even after adjusting the detuning and intensity within experimentally reasonable values. This is largely due to the fact the strength of the interaction between the atoms and the slowing beam is strongly based on the detuning in terms of the number of linewidths, while the velocity class of atoms which is affected by the slower is based on the absolute detuning. Using the slower on the narrow transition with a linewidth approximately 14 times narrower means slowing the atoms 200 times less effectively at the same absolute detuning, as the interaction scales with  $(\Delta/\gamma)^2$ . Alternatively we could choose to stay at the same number of linewidths detuned, but since the velocity distribution scales as  $v^2$  this also results in the same reduction factor due to there being less atoms traveling at that velocity. As a result, it is likely infeasible to remove 410 nm beams from the setup and use entirely 412 nm beams in order to produce the desired colder MOT. We would need to slow on the broad transition in order to capture enough atoms.

#### 4.4.3 Two-stage Cooling

Producing a MOT from the narrower transition allows a colder trap to be produced, which contributes to reduced atom loss during imaging and therefore better noise characteristics when attempting to measure single atoms. We can get around many of the disadvantages of the narrower transition by forming our narrow-line MOT with a two-stage approach [56] [57] - we first form a MOT on the broad 410 nm transition, and then load a MOT on the narrow 412 nm transition from this MOT. This has the advantage of the atoms already being cooled, as they would have a temperature of a few hundred micro-Kelvin instead of over a thousand Kelvin (having come from the hot effusion cell).

### 4.5 Conclusion

In this chapter we presented our process of precisely measuring of the excited-state hyperfine constants for the narrow-line 412 nm. Our measured values of  $A = 715.85 \pm 0.09$  MHz and  $B = 1015 \pm 9$  MHz are more precise than the previously-measured values of  $A = 719.5 \pm 21.0$  MHz and  $B = 935.4 \pm 179.9$  MHz [52]. We also briefly examine the prospects of using this transition to perform two-stage cooling within a MOT to produce atoms roughly an order of magnitude cooler than previously. This has allowed us to characterize the transition to a degree that shows promise for an experimental implementation.

# Chapter Five

## Single Atom Imaging

### 5.1 Introduction

We use a EMCCD camera to produce images of our atom clouds, combined with the FORT beam using the cage-mount system above. We have attempted to use two different cameras to observe single atoms - a Princeton Instruments ProEM 512 and a Hamamatsu C9100-13. We initially used the ProEM 512, but then switched to the C9100-13 after the ProEM had an equipment failure. The optical setup remained the same between both camera installations.

The process of measuring single atoms is very indirect and requires proper characterization of noise sources in order to make sure that a proper signal will be visible. To take single atom measurements, we perform the same trap loading sequence described in Chapter 3 in order to localize a small could of few atoms, hold the trap long enough that most of the atoms are lost from the trap, and then pulse the MOT beams to cause any atoms present to fluoresce.

If we were to sum all the individual images taken all together like for other data we have produced, we would produce a dim image of the trap with no particular information about the atom count. Instead, the individual images are aggregated into a histogram with the data bins corresponding to the data value which was read out on the camera. Ideally we should expect most of the images to be one of two categories of images; either a low number of camera counts when they do not contain an atom, or a higher number of counts due to the presence of a fluorescing atom.

## 5.2 Photon Scattering Rate

The scattering rate of photons per atom is given by the expression

$$r_{sc} = \sum \frac{\gamma}{2} \frac{I/I_s}{1 + 4\Delta^2/\gamma^2 + I/I_s}$$

which has a contribution from all transitions from the state that the atom is currently in. For many cases, the atom is near resonance for one of the transitions, causing the the scattering rate to be dominated by that particular transition.

In a MOT, there is a mixture of different  $m_F$  states with slightly different values of  $I_s$ . This dependence can be taken into account by noting the lifetime of the excited state depends on the dipole matrix element (squared) between the states of interest. We can take the ratio of these quantities, which also happens to be the Clebsch-Gordan coefficients between those states, and use them to produce state-dependent and polarization-dependent saturation intensities  $I_{s,M,q}$ . For the  $F = 11$  to  $F' = 12$  transition of interest:

$$I_{s,M,q} = \left( \frac{1}{\langle 11 M 1 q | 12 M + q \rangle} \right)^2 I_s$$

For randomly polarized light, we should therefore expect an  $M$ -dependent saturation intensity of the form

$$r_{sc} = \frac{1}{3} \sum_q \frac{\gamma}{2} \frac{I/I_{s,M,q}}{1 + 4\Delta^2/\gamma^2 + I/I_{s,M,q}}$$

and (assuming a uniform distribution of  $M$  states) an overall average scattering rate per atom of

$$r_{sc} = \frac{1}{11} \sum_M \frac{1}{3} \sum_q \frac{\gamma}{2} \frac{I/I_{s,M,q}}{1 + 4\Delta^2/\gamma^2 + I/I_{s,M,q}}$$

Using  $\gamma/2\pi = 32.5 \text{ MHz}$  and  $I_s = 614 \text{ W/m}^2$ , and measured values of  $\Delta = -70 \text{ MHz}$  and  $I = 1610 \text{ W/m}^2$ , this gives an averaged scattering rate of  $4.62 \text{ MHz}$ .

## 5.3 Experimental Factors

Given this scattering rate, we can calculate the total number of photons scattered by multiplying by the exposure time  $t_{exp}$ . In our case we also need to include an additional chopping

factor of  $\frac{1}{2}$  due to the fact that we are chopping the beams when imaging, effectively only scattering light half of the time. Imaging with chopped beams is important because it keeps the atoms localized to the trap volume instead of letting them freely expand outward. Given the temperature of our atoms, this outward expansion without chopping effectively limits the exposure time to roughly a millisecond before the atoms are too diffuse to be seen.

Photons emitted from the atomic cloud still need to reach the camera, so there are a few additional potential sources of loss that need to be considered. First the photon needs to be emitted in the right direction, which is accounted for by taking the appropriate fraction  $\Omega/4\pi$  of the solid angle that the collection optics subtends. The collection optics themselves aren't perfect, so there is some loss  $1 - \eta_{opt}$  associated with them as well. For the current Ho setup, we measured  $\Omega/4\pi = 0.0487834$  and  $\eta_{opt} = 0.5$ .

The photon impinging on the CCD is converted into a photoelectron, but this conversion is imperfect and has an associated quantum efficiency  $\eta_{QE}$ . At 410 nm, this is 80% for Princeton Instruments camera and 56% for the Hamamatsu camera.

These photoelectrons go through an electron-multiplying (EM) gain stage (gain  $G_{EM}$ ) which can effectively increase the number of electrons per photon. There is also an analog gain stage (gain  $G_{ana}$ ) which can increase the voltage produced by the photoelectrons. The quoted figure for High analog gain is 2.74 photoelectrons per count, and we almost always run with the maximum EM gain of 1000 to produce the brightest atom signal.

This voltage then goes into an Analog-to-Digital converter for the camera, which generally would result in some scaling (by some factor  $f$ ) between this voltage and the actual counts read off by the software. For the PICam software used on our experiment for the ProEM 512, there is no rescaling done ( $f = 1$ ) and thus whatever values that are read by the A-to-D converter are directly passed to the software that reads the data off from the camera. This also appears to be the case with the Hamamatsu C910-13.

Analog Gain	Measured e <sup>-</sup> /count	Dark counts/sec
Low	10.91	$6.4 \times 10^{-4}$
Medium	6.71	$1.0 \times 10^{-3}$
High	2.74	$2.9 \times 10^{-3}$

**Table 5.1** Dark counts per second for various analog gain settings. EM gain also linearly amplifies noise from dark current, so the maximum expected dark count rate can be as high as a factor of 1000 larger.

## 5.4 Camera Noise Statistics

### 5.4.1 Dark Current

Even when the camera shutter is closed and no light reaches the CCD, there is still a non-zero count which increases with exposure time. This is the dark current noise, which is primarily due to thermal noise in the electronics causing a charge buildup on the CCD. The Certificate of Performance on the ProEM states a maximum dark current of 0.007 electrons/pixel/sec. Even at the highest gain settings, where the dark current noise is the largest, we expect a negligible contribution of 2.55 counts/sec. The Hamamatsu C9100-13 has a similarly low dark count of 0.01 electrons/pixel/sec.

In either case, the dark current counts are negligible due to our exposure times remaining relatively short, on the order of milliseconds.

### 5.4.2 Read Noise

When taking repeated images of the same phenomenon, the counts on each frame have some variance due to how the camera amplifies the signal. This noise primarily comes from the electrical noise within the EM and analog gain stages, as well as noise in the analog-to-digital converter. As this type of noise gets added during the CCD read-out process, this contribution is independent of exposure time. It does, however, depend on the various gain settings on the camera. For our maximum gain settings of 1000 EM gain and high analog gain, this contribution is normally distributed with a standard deviation of roughly 18 counts

Readout Speed	Clock Rate	Noise electrons
Low	0.69 MHz	8 electrons
Medium	2.75 MHz	20 electrons
High	11 MHz	25 electrons

**Table 5.2** Noise electron counts for the Hamamatsu C9100-13 camera at various readout speeds. Reading the images out slower vastly decreases the spurious electrons generated from CIC noise.

on the ProEM 512.

Clock induced charge (CIC) is a specific type of read noise produced by the camera during the readout process, coming primarily from the clock to which all the camera's internal electronics are synchronized. In particular, high clock speeds and clock voltages can cause additional electrons to become mobile when each pixel is read out. CIC noise can be reduced by slower image readout speeds. This was negligible for the ProEM camera, but contributes a potentially non-negligible electron count on the Hamamatsu as noted in Figure 5.2.

The appearance of CIC noise resembles random pixels being much brighter than the rest of the frame (see Figure 5.1), with the brightness following an one-sided exponential distribution (see Figure 5.2). Since the contribution to the count histograms falls off exponentially, this typically is not an issue unless either the counts per atom are very small or the loading efficiency of single atoms is very poor.

### 5.4.3 Non-Ideal Gain Characteristics

EM gain is in principle a one-to-one relationship; an EM gain setting of  $G$  should result in the number of photoelectrons being multiplied by  $G$ . This is calculated from relating the EM gain to the number of gain stages  $N$  and probability of generating an extra electron  $g$  at every gain stage via the relationship  $G = (1 + g)^N$ .  $g$  is typically small, around 1% to 2%, while the number of gain stages is typically on the order of a few hundred.

The physical mechanism for electron-multiplying gain is based on using a high voltage (30-50 V) to accelerate the photoelectrons into each successive gain stage with enough kinetic

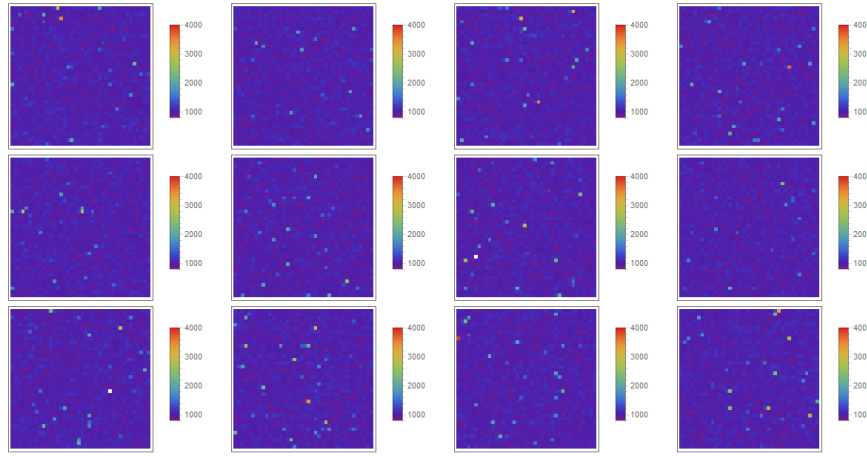


**Figure 5.1** A sample of a few images taken from the camera with the shutter closed, so no ambient light reaches the CCD. With ideal readout these images would all be identical and uniform, but what we are left with is any additional measurement artifacts related to the readout electronics. The random brighter pixels are due to CIC noise, while the nonuniform background color comes from other sources of readout noise.

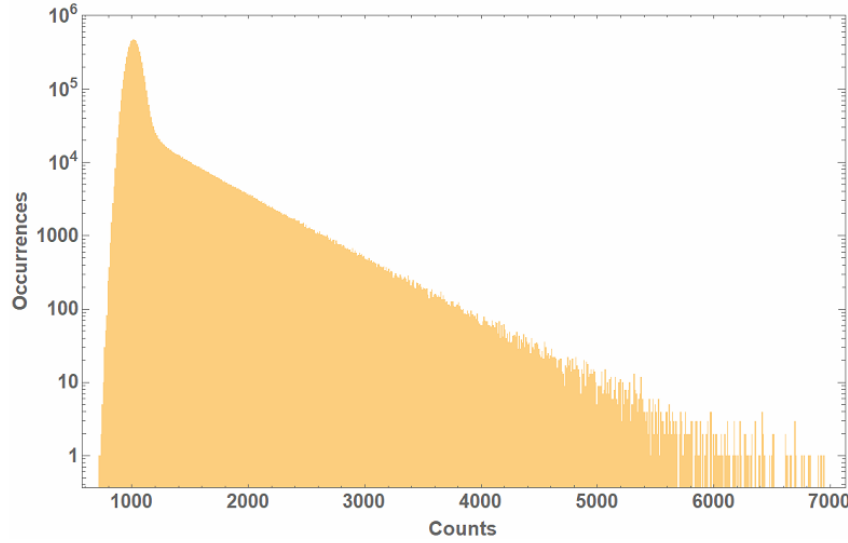


**Figure 5.2** A histogram generated from all the pixel values read out over a few thousand distinct images. As the extent of the noise is only apparent on a logarithmic scale, this is only an issue for very weak signals.

energy to generate an electron-hole pair in an impact ionization event. This is highly dependent on the temperature of the electronics [58]; for example with the Hamamatsu camera, each increase of 20 degrees C reduces the gain by about a factor of 1.2 [59].

The EM gain factor is linear (eg. an EM gain of  $G$  results in a multiplication of the photoelectron count by  $G$ ) as long as the camera is properly calibrated, which typically needs to be done every few months. There is also a gradual "gain aging" process wherein the effectiveness of EM gain tends to degrade over time as a function of how much charge has passed through the electronics. The primary way around this is to adjust gain so that it is just high enough to see the intended signal (over the readout noise) in order to reduce long-term degradation over time.

#### 5.4.4 CCD Active Bias

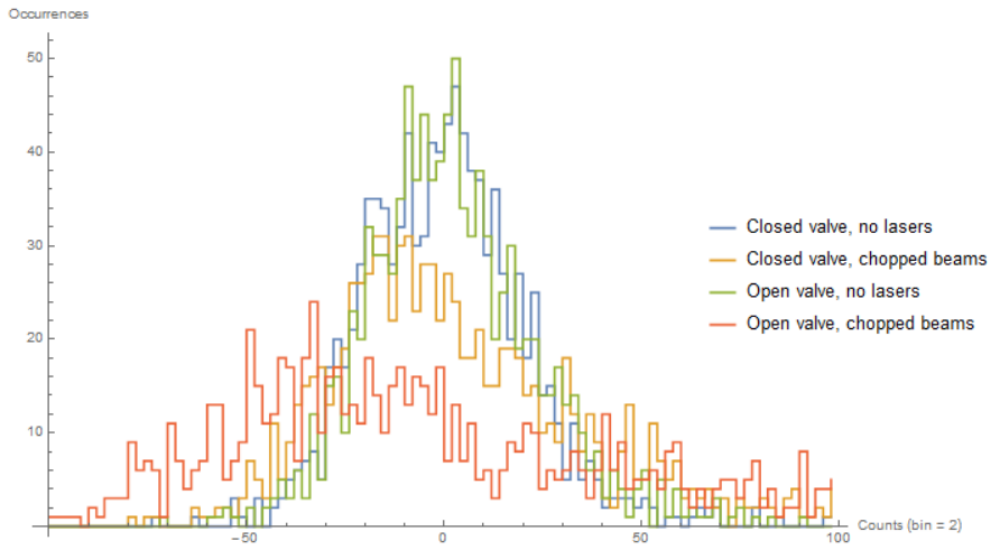
Both cameras have an active positive bias on all frames, in order to allow for various types of noise with a zero average to be properly measured, as having a zero-count baseline does not allow for negative values to be read out on the CCD [60]. The spatial structure of this bias frame may change based on various other experimental parameters, as well as the camera settings (primarily gain and exposure time), so it is important to take a background shot for the purpose of subtracting it out.

#### 5.4.5 External Noise Factors

There are multiple sources of noise unrelated to the camera electronics which can be present in our images for single atoms, and due to the small size of our single-atom signal, it is important to properly characterize every source individually. The presence or absence of the atomic beam from the oven and laser beams for imaging causes additional noise counts due to additional light being scattered towards the CCD which is not coming from the trap itself. We find that with no lasers going into the chamber, the noise counts are effectively the same regardless of whether or not the atomic beam is present.

## ProEM Light Scatter

When there is laser light going into the chamber we find that the observed noise is significantly higher, in fact almost an order of magnitude higher with all beams during imaging active (see Figure 5.3). We measured this increased noise under the same conditions as imaging the trap - the MOT and trap beams were chopped out of phase with each other.

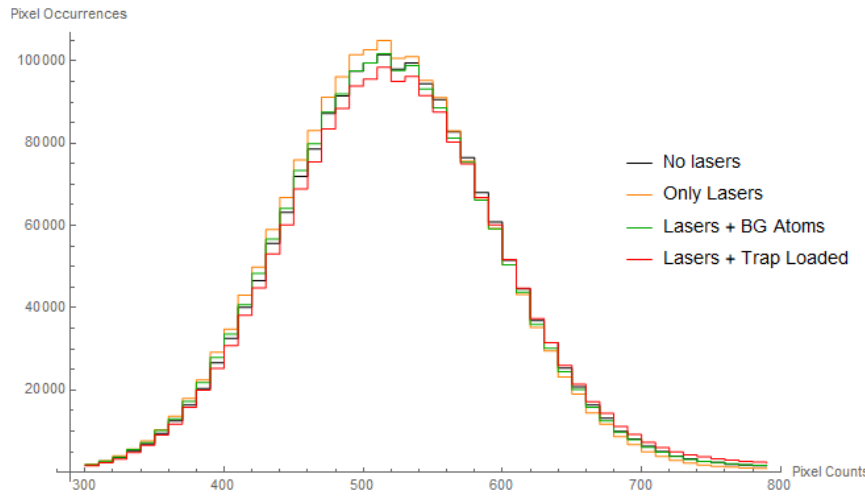


Imaging Condition	Noise counts (standard deviation)
No atoms, no lasers	17.6
Atoms, no lasers	18.7
No atoms, chopped lasers	44.1
Atoms and chopped lasers	102.2

**Table 5.3** Data showing the noise contributions from the lasers and atoms in various conditions for the ProEM camera. To take these measurements, the atoms were controlled via the gate valve in the vacuum chamber and the laser beams were controlled by a beam block farther upstream so no leakage from the AOMs would reach the camera. These were taken with a 4.5 ms exposure time.

## Hamamatsu Light Scatter

After switching the cameras, recalibrating the optical setup, and installing some improved spatial filtering to remove scatter from background light, we took the same background scatter measurements with the Hamamatsu C9100-13. The largest improvements came from the spatial filtering, resulting in a reduction in the counts contributed from the scatter by roughly a factor of three.



Imaging Condition	Mean counts	Noise counts (standard deviation)
No atoms, no lasers	529.8	147.4
No atoms, all lasers	546.7	191.2
BG atoms, all lasers	546.3	195.9
Trapped atoms, all lasers	567.9	244.9

**Table 5.4** Noise counts from the Hamamatsu C9100-13 camera, taken with the same conditions as in Figure 5.3. The read noise is generally higher, likely lending to a difference in the internal camera electronics, but the gain characteristics of the Hamamatsu were generally more stable than the ProEM 512 over longer time spans. The higher variance in counts shows up primarily in the exponential tail of CIC noise.

### 5.4.6 Overall Signal-to-Noise Ratio

Given the prior calculations, we expect roughly 6500 counts from the light scattered from a single atom per millisecond of exposure. Adding the various sources of noise above in quadrature, the total noise is roughly 260 counts/pixel for the Hamamatsu C9100-13. This suggests a SNR of roughly 25, but only if single atoms emit all of their light in a way that gets imaged onto a single pixel.

There are however two problems which threaten to reduce the signal to a low enough level that it cannot be seen over the camera noise. The first is the fact that experimentally our trap is imaged onto a group of 5-8 pixels with our current imaging setup. If the atom signal is spread across  $N$  pixels then the SNR is also divided by  $N$ , due to the fact that photons emitted can hit one of many pixels and the fact that all of the relevant noise sources for our experiment are per pixel.

The other problem is that the atoms appear to be too hot to stay around in the trap during the imaging process. Even with the chopped imaging, we find that the atom population in the trap as we perform our imaging pulse decays exponentially with a time constant of 1 ms. As a result, there is a balancing act that needs to be played for the exposure time - too small and read noise dominates over the signal, but too large and the noise counts from the additional scattered light dominates over the single atom which has long since left the image.

With our noise model, taking all the previously-mentioned figures and examining the signal-to-noise ratio for single-atom fluorescence spread over varying numbers of pixels, we get a signal-to-noise ratio as shown in Figure 5.3.

## 5.5 Measurement Process

To observe single atoms, we start with the regular procedure of loading the dipole trap as outlined in Chapter 3. Then, we hold the trap for a fixed amount of time corresponding to the amount of time we would expect to need to hold it for the atom count to decay down to a single atom. Finally we flash the MOT beams on the atom to cause it to fluoresce, and

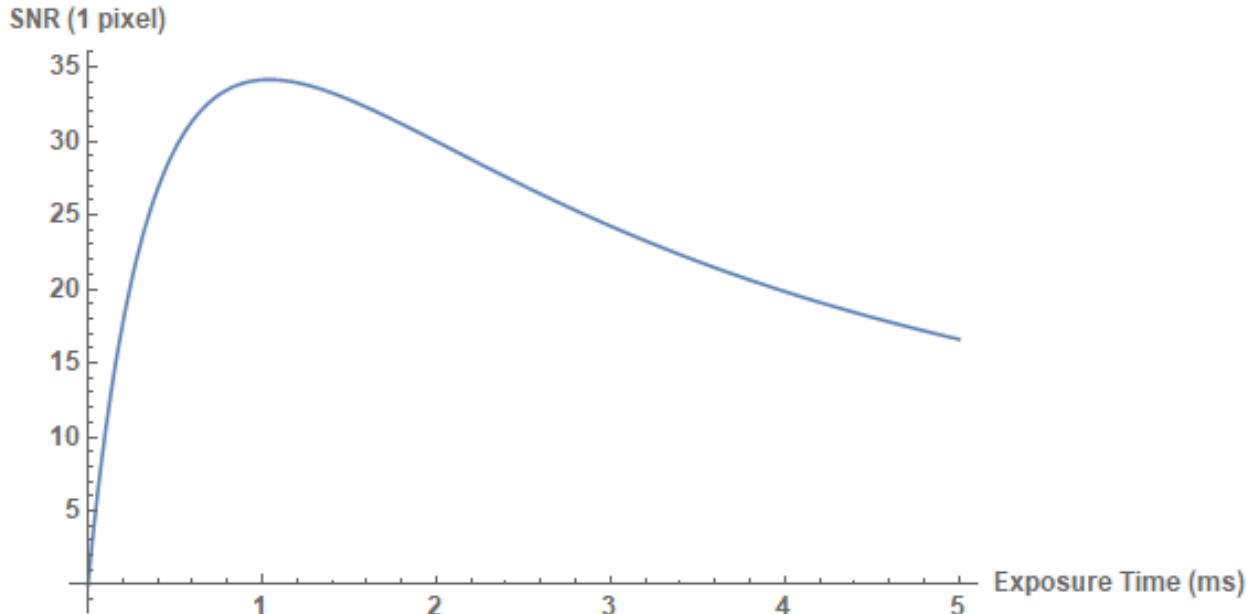


**Figure 5.3** Plot of the expected signal-to-noise ratio for single atom measurements, given our noise model and measurements. The optimal exposure time for our setup is 1 ms in order to maximize our SNR. If the trap is spread across too many pixels, the SNR is marginal at best and may result in the single atom signal not being seen.

simultaneously expose the camera to capture the fluorescence.

Each individual frame has a background subtracted away from it, which is produced by taking an averaged background over an equal number of separate frames (usually a few hundred) with the only difference in the experimental procedure being that the trap light is never turned on. This is in order to produce the background image with all the same external noise properties mentioned in Section 5.4, which is an acceptable background as we have found that the presence or absence of the trap light does not noticeably affect noise counts.

This results in a set of images which, if summed together pixel-by-pixel, would produce something which looks similar to the initial dipole trap with hundreds of atoms. The aggregate image of all the frames together tells us where the atoms are present in the image frame, so we use it to determine which pixels we would expect a single atom to be present within. Then, on each frame we sum the counts over those specified pixels, producing a value for

the total counts present from the atom's fluorescence.

Taking all of these individual-frame total counts and combining them together in a histogram results in a distribution which has peaks with center locations corresponding to the number of atoms present, and widths corresponding to a combination of all camera noise contributions.

## 5.6 Ideal Histograms

The peaks in a histogram for observing single atoms have a structure given by the combination of multiple separate processes. The photon count scattered off of the atom(s) in the trap follows a Poisson distribution with a very large mean. All of the previously-mentioned camera noise processes can also be modeled as independent Poisson distributions over the number of camera counts. The noise processes can be combined together in order to produce a single Poisson function corresponding to the camera. The expected distribution corresponding to a single atom in the trap would then be a combination of these Poisson functions.

This can be vastly simplified by noting that the sum of independent Poisson processes is itself another Poisson process, and that the convolution of different Poisson processes with different means is a Poisson process with the sum of the means of the individual processes. With care to convert the scattered photon count to an analogous number of camera counts, the combined distribution is then a single Poisson distribution with a mean calculated by the sum of all the means of the individual processes.

Additionally the number of atoms in the trap also follows a Poisson distribution. This is however a Poisson distribution over the number of atoms, rather than the number of camera counts. In order for single atoms to be feasibly observable, the number of camera counts per atom should be larger than the mean of the combined Poisson from the scattering and camera counts. Such conditions would correspond to a high signal-to-noise ratio.

In this regime the resultant single-atom data would look like multiple Poisson distributions - one for zero atoms, one shifted horizontally for a single atom, one for two atoms, and so on. Other experimental conditions would be configured so that the average atom count in the trap is such that the first two peaks are the largest and any others with two or more

atoms are negligible. Under good experimental conditions, the two would have a horizontal separation well above the width of each individual peak, making them clearly distinguishable [61]. A few example histograms constructed from this model with different signal-to-noise ratios can be seen in Figure 5.4.

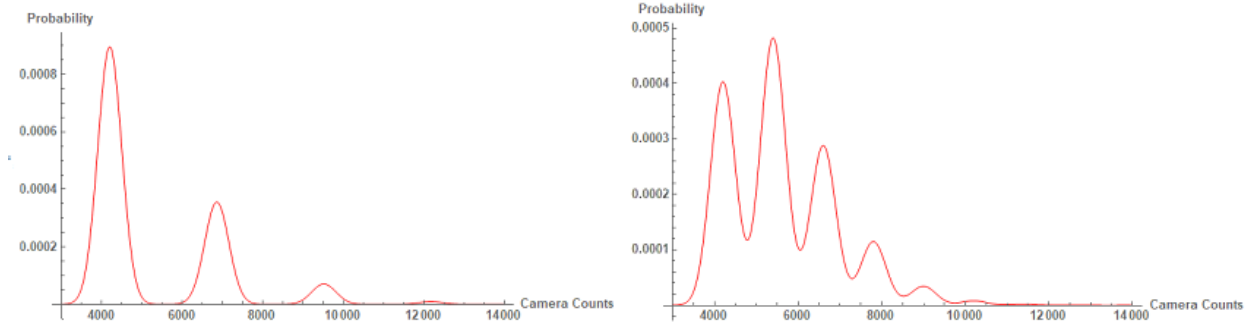


**Figure 5.4** Two theoretical histograms of single atom data, based on our noise model. The left plot is with a mean atom count of 0.4 and SNR of 4, leading to several spatially well-separated peaks. The right plot has a mean atom count of 1.2 and SNR of 2, showing the Poissonian shape of the relative peak heights and the poorer peak separation.

## 5.7 Single Atom Attempts for Holmium

After characterizing all the noise figures for the Hamamatsu camera, we started taking single atom measurements in our dipole trap. Due to a large number of experimental parameters having been changed due to some equipment failures after a temporary shutdown due to COVID-19, we produced a very weak trap which was only able to load a very small number of atoms. However observing single atoms does not require being able to load large amounts of atoms into the trap, only cold atoms, so our experimental process was simply to load the trap, hold it for 10 ms to let the MOT drop away, and then image the trap.

We were able to see a very weak single atom signal, just barely visible above the read noise and CIC noise. Figure 5.5 shows a single atom histogram we generated from our data, overlaid with a fitted theoretical signal based on our noise model. The fitted values suggest

that our mean atom count is 0.2, corresponding to a single atom loading efficiency of  $\approx 16\%$ .

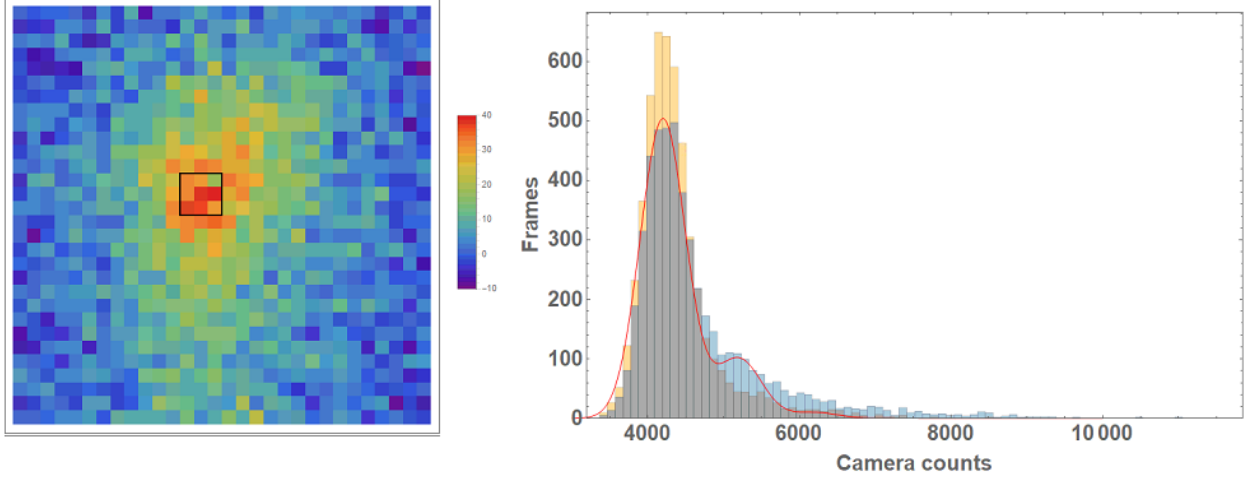


**Figure 5.5** An image of the trap (left) and a histogram (right) generated by summing the counts in the black box indicated on the trap image. The red curve is a fitted theoretical single atom signal. This data consists of 5000 separate frames.

The fitted model we use does not account for the CIC noise, which was managed by performing the fit on the data only out to 6000 counts in order to prevent overfitting to the CIC noise. The CIC noise in our data has the noticeable effect of partially obscuring the one-atom peak and completely hiding any peaks corresponding to more atoms. Based on the theoretical fit, the camera noise counts have a mean of 600 and the counts per atom are 920, suggesting a poor SNR of only about 1.5.

## 5.8 Explanation for low SNR on single atom signal

The signal to noise ratio for our single atom data is very low, and we have a few reasons which may be the case that we have tried and failed to successfully resolve.

### 5.8.1 Imaging Loss

The primary issue is due loss of the atoms during the imaging process. We have observed that the atoms leave the trapping region with a  $1/e$  time of roughly 0.8 ms, which we were

unable to improve by any means we tried. This is effectively a hard limit on how strong we can make our signal, and was the main problem we attempted to address in order to properly measure single atoms.

The really short time scale for the imaging loss is approximately consistent with the atoms in the trap expanding freely outward with no trapping potential at all. Our initial attempt at keeping the atoms around by chopping the beams in the same way they were chopped during the loading showed no noticeable improvement to the imaging loss. We then attempted to image with the trap beam entirely off, shining the MOT beams continuously to keep the atoms around using only the effect of optical molasses. In the past, we have measured the lifetime of the MOT due to the molasses to be on the order of 5 ms, but this also seemed to show no noticeable improvement.

Since holmium is very highly magnetic, we are also more experimentally susceptible to variations in the ambient magnetic field than many other AMO experiments. We set up a home-built magnetic field sensor board near our vacuum chamber and found that the ambient field is stable to within 5 mG over the time span of a day, which should be small enough to be irrelevant. Nevertheless we have observed that the optimal shim settings change over the course of a few days with a magnitude consistent with the fields changing by hundreds of milli-Gauss, likely attributed to other sources of experimental instability which we were unable to diagnose. This affects the day-to-day loading of our MOT and FORT but has no effect on the imaging loss, which we demonstrated by seeing that the loss time scale remained unaffected even when the shim fields were intentionally tuned in the wrong direction by as much as 3 Gauss.

### 5.8.2 Optical Setup

An additional factor which decreased the quality of our signal is the fact that the trap is imaged onto a large number of pixels on the EMCCD, resulting in an already low SNR being worsened due to the signal being spread across multiple pixels. We suspected this was because the trap focal plane and imaging focal plane were misaligned. The focal plane alignment was then carefully done and characterized multiple times (see Appendix A), but

the only insight this offered was that the trap beam was slightly astigmatic. This leads to a slightly lower trap depth than we expect, reducing it by about 11%. The separation of the focal planes is well within the trap's Rayleigh length of 100 microns and as a result generally did not noticeably affect the overall profile of the beam.

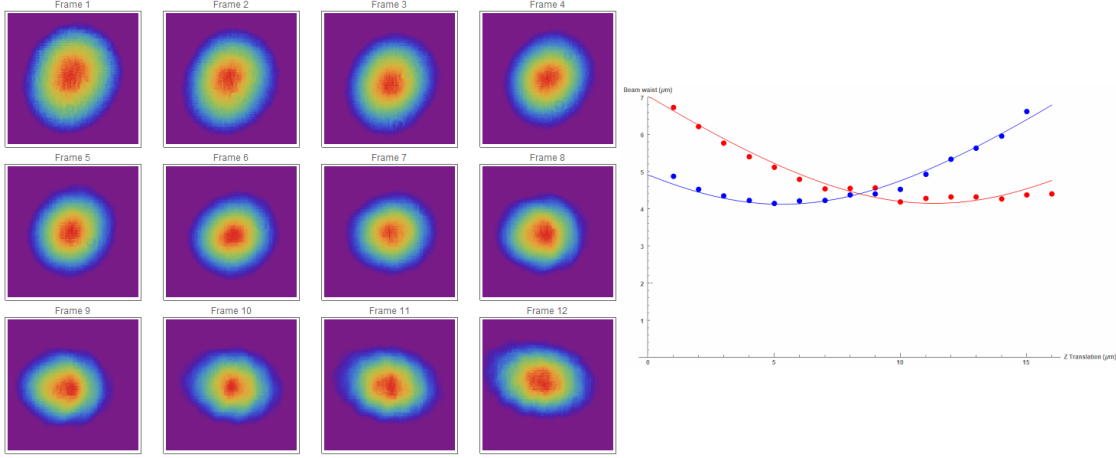


**Figure 5.6** Images and plots of the measured beam widths of our trap beam, fitted to the principal axes of the beam. The fitted waists are 4.11 and 4.14 microns, with the focal planes of the two axes being 6.0 microns apart.

### 5.8.3 Experimental Issues

Besides measurement-related problems, we also had additional issues with the equipment itself. Much of it can be attributed to needing to make multiple changes to our experimental configuration due to equipment failure, without getting adequate time in between to characterize how individual changes affected the quality of our trap. There was a long period of nearly two years between needing to replace the vacuum hardware for our atomic source and seeing successful optical trapping again. We performed the narrow-line spectroscopy and some upgrades to our laser stabilization electronics in the interim, but then the COVID-19 pandemic and a serious personal injury occurred which prevented substantial in-lab work from being done for much of the second year.

By the time we had trapped atoms again, the trap lifetime was very short (on the order of 30 ms, roughly a factor of 20 shorter than before) and we were unable to noticeably

improve it. This was likely due to degradation in our pump laser for our Ti:Sa, resulting in lower available optical power in our MOT beams. In order to produce a MOT we had to retroreflect the MOT beams, which then results in poorer sub-Doppler cooling due to less control over the power and polarization of the retroreflected beam.

There is the prospect of the chopped imaging working more effectively with colder atoms which we think should be possible once cooling on the narrow 412 nm transition is properly set up, but our current 412 nm system is very marginal on power and may not be able to provide sufficient cooling to have a noticeable effect without potential experimental upgrades.

## 5.9 Conclusion

In this chapter, we performed an in-depth characterization of the EMCCD camera and optical system we used for our single atom measurements. We have some early results for a very weak single atom signal and have examined multiple issues which may be contributing to the small signal, as well as possible solutions to those issues.

# Chapter Six

## Magnetic Trapping

Holmium is one of the most magnetic elements in the periodic table, second only to dysprosium. This allows it to be used for some purposes in AMO experiments much more easily than the more commonly-used alkali atoms.

### 6.1 Magnetic Moment of Holmium

The magnetic moment of an atom comes from a combination of its total electron angular momentum and the Landé g-factor for that particular state, a dimensionless quantity which appears when examining the energy shift of an atomic state in a weak magnetic field using first order perturbation theory. The Landé g-factor  $g_J$  is given by

$$g_J = g_L \frac{J(J+1) - S(S+1) + L(L+1)}{2J(J+1)} + g_S \frac{J(J+1) + S(S+1) - L(L+1)}{2J(J+1)}$$

where  $g_L = 1$  and  $g_S \approx 2$  are the g-factors for the electron orbital and spin angular momentum, respectively. To include the nuclear angular momentum, we couple  $I$  and  $J$  together to form  $F$  similarly to above where  $L$  and  $S$  form  $J$ . Since  $g_I \ll g_J$ , we can make approximate Landé g-factor  $g_F$  for the total atomic angular momentum as

$$g_F = g_J \frac{F(F+1) - I(I+1) + J(J+1)}{2F(F+1)}$$

The magnetic moment of an atomic hyperfine state is equal to  $\mu_B g_F \sqrt{F(F+1)}$ . In Figure 6.1 we note that the magnetic moment of rare earths is much higher than the magnetic

Element	Magnetic Moment
Rb	$\mu_B$
Cs	$\mu_B$
Er	$7\mu_B$
Tm	$4\mu_B$
Ho	$9\mu_B$
Dy	$10\mu_B$

**Table 6.1** Magnetic moments for the ground states of select atoms used in various atomic physics experiments.

moment of the more commonly used alkali atoms, which makes rare earths more viable for magnetic traps. In particular, it allows us to produce magnetic traps with the same depth in potential energy, but without the need for laser power and all the associated experimental overhead. The larger sensitivity of holmium to magnetic fields also means that cold atoms can be held against gravity with a modest 3.1 G/cm gradient, only a tenth of the gradient produced by our MOT coils during our regular experiment cycle.

## 6.2 Magnetic Trapping

In order to magnetically trap atoms, we note that the energy from the Zeeman interaction is the same as the energy of a magnetic dipole inside of a magnetic field. Thus, states with  $g_F m_F > 0$  are drawn to local minima in the magnetic field magnitude and  $g_F m_F < 0$  are drawn to local field maxima. We can remove many states from consideration as they are not useful for magnetic trapping. The  $g_F m_F < 0$  states (high-field seekers) cannot be used, as Earnshaw's Theorem forbids a local field maximum in free space [62]. States with  $g_F m_F = 0$  (clock states) are normally desirable for their insensitivity to external fields, but in this case is the exact opposite of what we want since they remain unaffected. They also act as a channel for atom loss via Majorana spin-flip transitions due to an ambiguous spin quantization axis [63]. We are left with 60 out of the 128 available states as magnetically

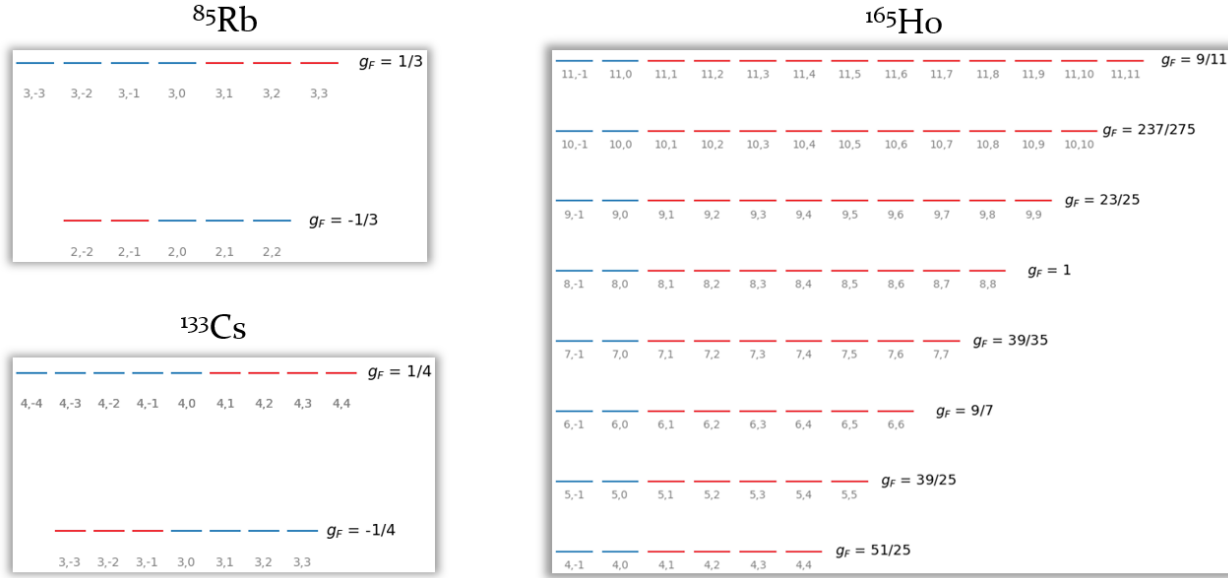


**Figure 6.1** Diagram showing magnetically trappable states for Rb, Cs, and Ho. Due to the placement of the states, the alkalis require multiple photons to transition between trappable states.

trappable.

The geometric setup is thus necessarily a configuration that produces a local minimum in the magnetic field magnitude. The simplest way to produce such a geometry is in fact already naturally produced by our MOT coils, as their anti-Helmholtz configuration produces a quadrupole field with a zero-crossing in its center. In order to eliminate the spin-flip losses, a small constant bias field can be applied via our shim coils to ensure that the magnitude does not reach zero but still has a local minimum.

There is an additional advantage of using holmium over the more commonly-used rubidium and cesium for this approach. All of the g-factors  $g_F$  in Ho are positive, whereas in Rb/Cs different hyperfine levels have different signs for  $g_F$ . This causes the magnetically trappable states to be arranged in a much more optically accessible way in holmium than in alkalis (see Figure 6.1).

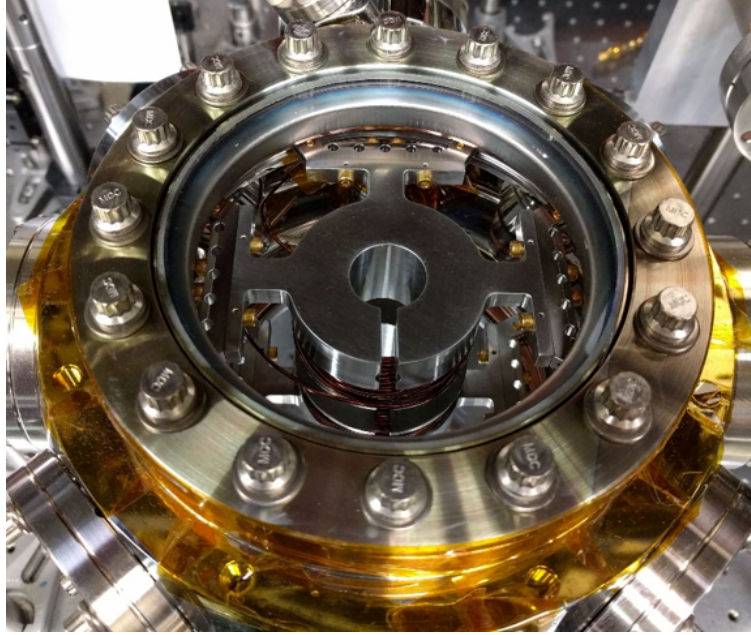


**Figure 6.2** Image of the in-vacuum MOT coils

### 6.3 Trapping in a Quadrupole Gradient

For a magnetic trap formed in the quadrupole field generated from a pair of MOT gradient coils, the potential the atoms experience is to first order linear with respect to the distance from the minimum. Therefore, the only necessary figure to determine the depth of the trap in this configuration is the steepness of the B-field gradient, commonly measured in units of Gauss/cm.

The magnetic field produced by a pair of anti-Helmholtz coils on-axis is an elementary physics problem, but the field off-axis is nontrivial and involves hypergeometric functions. To first order with a numerical approximation of the aforementioned hypergeometric functions, the fields for a pair of anti-Helmholtz coils with average radius  $R$  and distance  $D$  from the origin is

$$B_z = \mu_0 I \frac{3DR^2}{(D^2 + R^2)^{5/2}} z \quad (6.1)$$

$$B_\rho \approx \mu_0 I \frac{0.429}{R^2} \rho \quad (6.2)$$

With these approximations and the assumption that  $D = R$ , the magnitude of the

magnetic field near the center of the coils has a magnitude given by

$$|B| \approx \frac{\mu_0 I}{R^2} \sqrt{(0.530z)^2 + (0.429\rho)^2} \quad (6.3)$$

which always points outward, away from the center. The similar prefactors of  $z$  and  $\rho$  also tell us that we do not need to worry about substantial anisotropic effects, as the atoms experience largely the same potential in every direction.

### 6.3.1 MOT Coil Configuration

Our in-vacuum MOT coils are held in place by coil holders made from 304L stainless steel, with holes to allow for proper venting of gas when the system is pumped down to UHV. Additionally, the coil holder itself has a slot in order to reduce any eddy currents induced when the current in the coils changes. The coils are in a standard anti-Helmholtz configuration with an inner radius of 1.6 cm, outer radius of 2.75 cm, height of 0.8 cm, and designed separation distance of 1.6 cm. This allows a total of 60 turns of Kapton-coated 18 gauge wire, 10 radially and 6 vertically. Using the Equation 6.3 with these coil dimensions gives a calculated gradient of 13.87 G/cm/A, and during installation we used a magnetic probe to directly measure the gradient as 13.75 G/cm/A.

In Figure 6.3 we see a comparison between the potential due to our dipole trap and the on-axis magnetic potential. At a distance equal to the size of our dipole trap the trap depth is only  $10.9 \mu K$ , roughly two orders of magnitude smaller than the potential from the optical trap. We can obtain a magnetic trap depth equal to the optical trap depth if we go out to a distance of  $\approx 400 \mu m$ , and the total depth of the magnetic trap in our configuration is 25 mK out to a distance of 10 mm.

## 6.4 Magnetic Trap Lifetime

While magnetic traps generally have much shallower potentials, their total depth from their minimum out to their edges in this quadrupole field are extremely deep. As a result, in many cases a good magnetic trap has a decay lifetime which is mostly limited by collisions

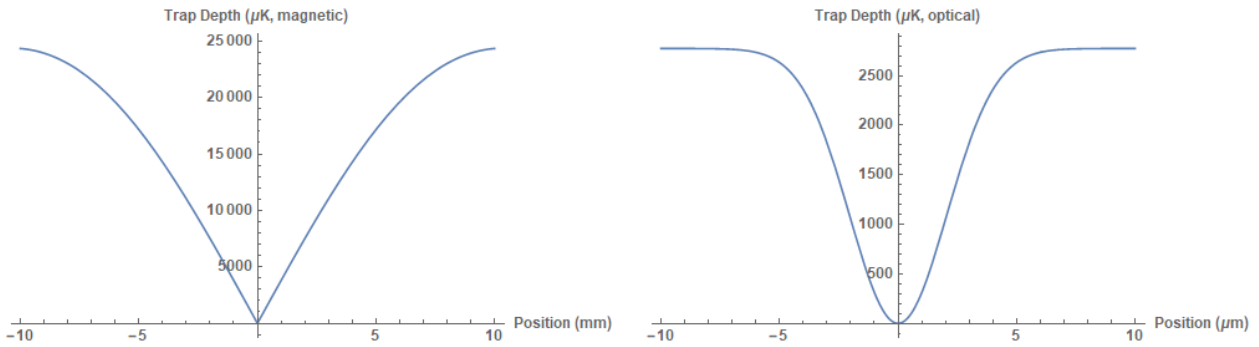


**Figure 6.3** Potential energy structure near the center of the MOT coils, compared to our current optical dipole trap. Note the difference in both scales, which is significant enough that they cannot be meaningfully plot together on the same set of axes.

with residual background atoms in the vacuum chamber. The vacuum-limited lifetime of a trap is then inversely proportional to the pressure of these residual atoms, being around a second at  $2.3 \times 10^{-9}$  Torr [45]. In typical atomic physics experiments vacuum hardware often allows even lower pressures, making this figure on the order of tens of seconds or even many minutes.

Older data on magnetically trapping holmium in the quadrupole field shows that we were able to produce a magnetic trap with a lifetime of  $1.63 \pm 0.08$  seconds. The atom count within the trap initially increases over approximately the first second of loading, suggesting that there is a large population of atoms being loaded into the MOT from dark metastable states as seen in other rare earth MOTs [25].

## 6.5 Magnetic Trap Array

While our current experimental configuration does not currently allow for further examination of magnetic trapping beyond trapping in the center of a quadrupole gradient field, there are potential future developments to be done in terms of using magnetically-trapped single holmium atoms in an array of multiple qubits.

Atom arrays are commonly produced with an optical lattice formed by multiple beams

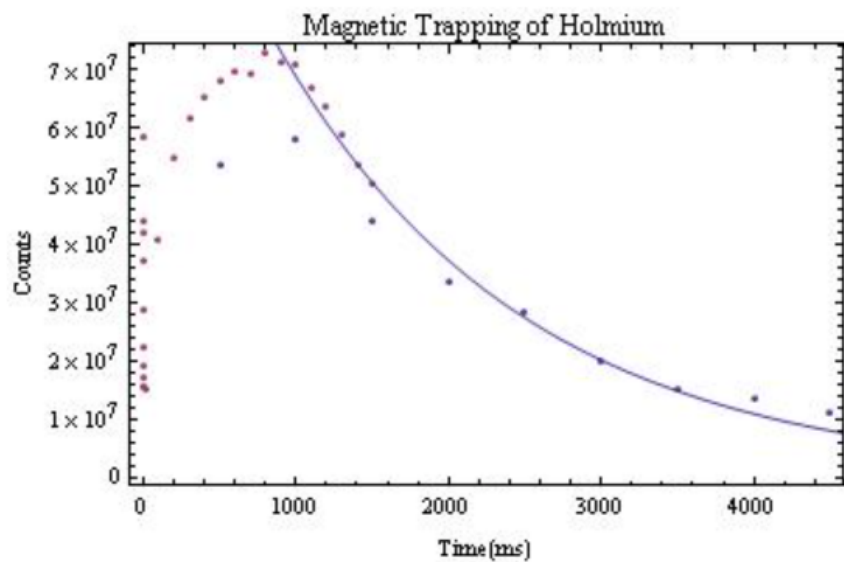


**Figure 6.4** Old data of magnetic trapping of holmium within the quadrupole gradient field from the MOT coils. The population falls quickly and then loads from the dark magnetically-trapped states.

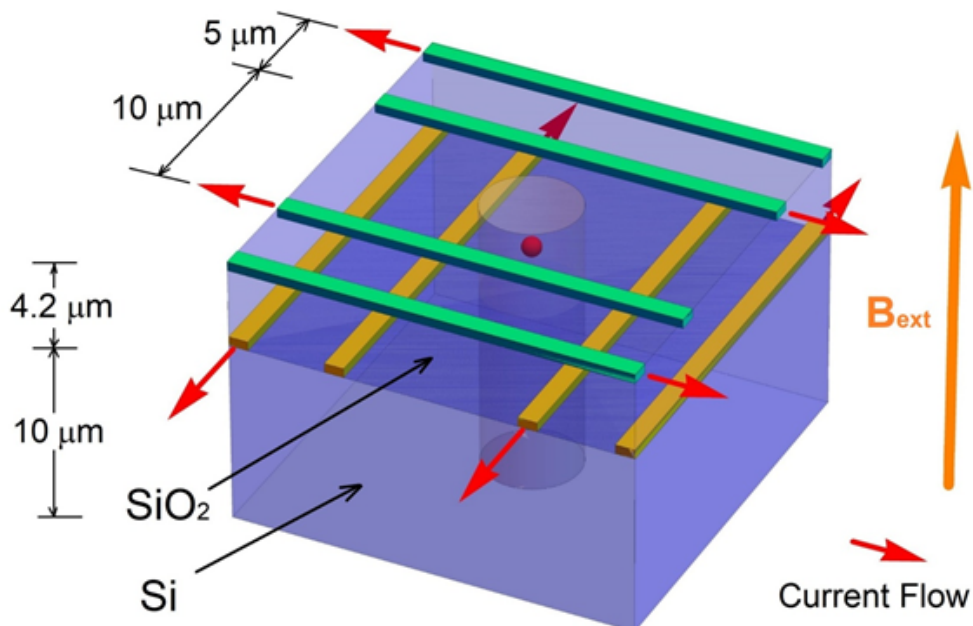


**Figure 6.5** Layout for a unit cell of the magnetic trap array

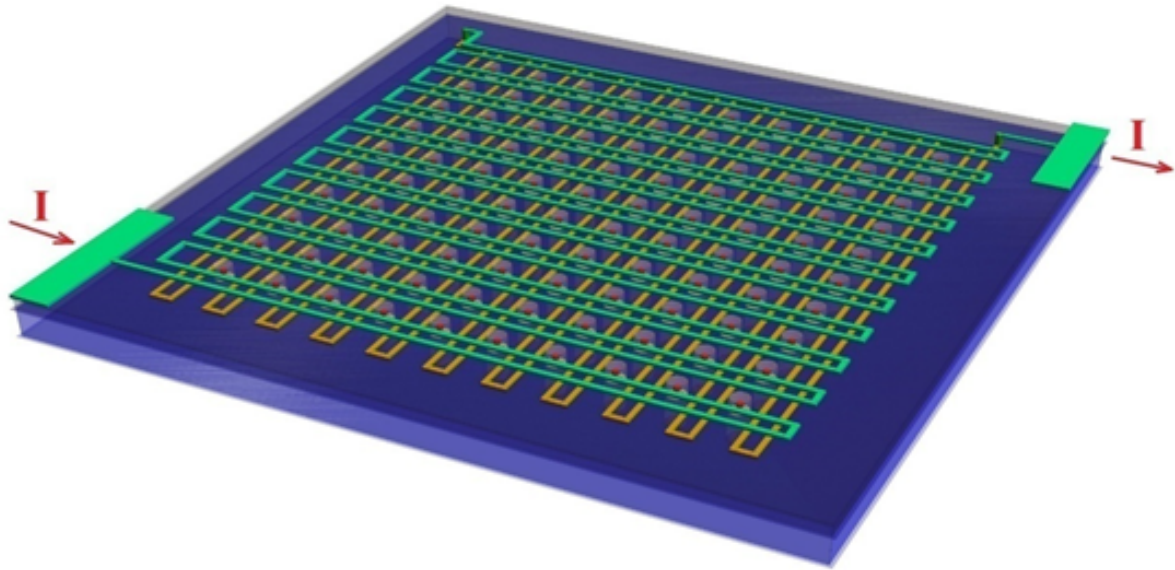


**Figure 6.6** View of the overall structure of the magnetic trap array

which spatially overlap to form a grid where each site is able to hold a single atom [10][14]. One major disadvantage to this approach, however, is that it does not scale well. The number of available atom sites will generally scale linearly with the available laser power, and in practice experimental overhead often increases nonlinearly with respect to laser power.

Magnetic trapping is a different approach to producing an atom array, where instead of producing the trapping potential with an array of optical dipole traps, it is produced by an array of magnetic traps. Magnetic trapping potentials are produced by nearby current-carrying wires, which are much easier to scale up compared to optical traps. Thus, a magnetic trap array would involve designing a single such magnetic trap, and then tiling the design in 2D to produce the array.

### 6.5.1 Wire Material

Our design would use wires to carry a current to create the desired magnetic potential structure, which would be patterned out on a silicon substrate. On top of the substrate

would be an insulating layer and then another set of wires running perpendicularly in the other horizontal axis. The cross section of the wires for the magnetic trap design is 0.5 microns by 1 micron and would carry a current of 50 mA. Calculations for ohmic heating due to the high current density are relatively straightforward, where the power dissipated per unit length is

$$P = \frac{\rho I^2}{A}$$

where  $\rho$  is the resistivity of the wire material,  $I$  is the wire current, and  $A$  is the cross-sectional area of the wire. For most commonly used wire materials,  $\rho \approx 2 \times 10^{-8} \Omega \cdot m$ , which results in a figure of approximately 100 mW of power being dissipated per mm of wire length. If we were to fabricate a chip capable of making an 11 by 11 array of traps, we would have close to 1 W of power being sunk into a chip only approximately 200 microns in each dimension. Based on empirical models, this would result in an equilibrium temperature for the chip well in excess of 100 °C [64].

This makes it clear that the required current density within the wires leads to typical materials having too high of a resistivity to work. Thus the wires would need to be a superconducting material. Furthermore, as room-temperature superconductors still do not currently exist, this would also require the additional experimental overhead and cost of installing the existing setup inside of a cryostat and cooling it with liquid helium.

### 6.5.2 Potential Energy Structure

To create each individual trap, holes would be cut through both layers and the atom would reside within each hole. The calculated magnetic potential due to our design is well approximated by a harmonic potential in all three axes, but only at low energy. The calculated trap frequencies in this geometry are 336 kHz, 336 kHz, and 185 kHz, suggesting a more isotropic trapping potential than what is normally produced from optical traps.

An applied external bias field of 40 Gauss produces a field of 3.5 G at the center of the trap, which is a magic field condition for the pair of states  $|F, m_F\rangle = |5, 5\rangle$  and  $|7, 7\rangle$ . The implications of this are explored more in Chapter 7.

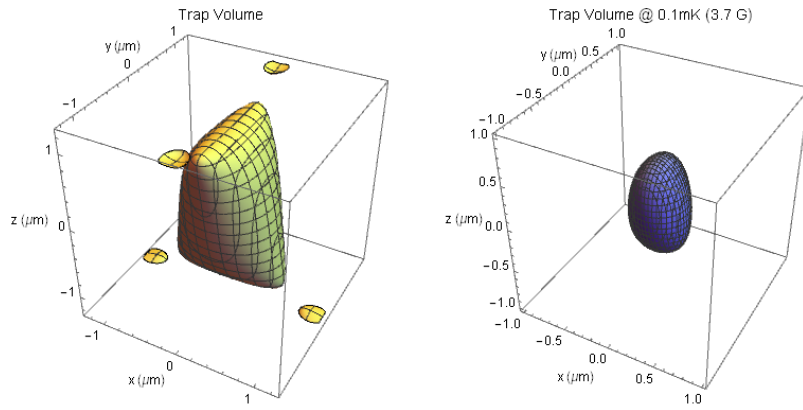


**Figure 6.7** Two equipotentials for the magnetic trapping potential, one at one tenth of the total trap depth (right) and one of the highest energy which remains trapped, showing shape distortion when examining a larger scale. Note the factor of ten difference in the length scales.

### 6.5.3 Disadvantages

Using magnetic traps is not without its disadvantages. In our case one of the more obvious disadvantages is that our design would add the additional experimental complexity of a cryostat, hardware which is otherwise not needed and often less commonly used in atomic physics labs in general.

Additionally, while the increased magnetic response of holmium is desirable for a deeper magnetic potential, it also means that the noise control requirements are stricter by the same factor - nearly an order of magnitude. This noise is also able to cause qubit state decoherence as well, but we can estimate the coherence time based on how much the qubit frequency  $\Delta\nu(B)$  changes over noise of magnitude  $\epsilon$ :

$$\tau = \left| \frac{1}{\Delta\nu(B + \epsilon) - \Delta\nu(B - \epsilon)} \right|$$

In general these coherence times are on the order of  $10^3$  seconds. Tuning the magic field conditions can significantly increase the lifetime by decreasing how much  $\Delta\nu$  changes over the span of the noise. For the  $|5, 5\rangle$  to  $|7, 7\rangle$  qubit in particular, this coherence time is  $\approx 94000$  seconds with  $\epsilon = \pm 10mG$  B-field noise.

## 6.6 Conclusion

In this chapter we analyzed the theoretical prospect of using holmium in a magnetic trap, in order to take advantage of its highly magnetic nature. We also present a possible design for an array of magnetic traps, in contrast to the more commonly used arrays of optical traps, and examine its potential advantages and disadvantages. Additionally we found that indeed the high magnetic moment of holmium leads to a very long-lived magnetic trap in the lab, which shows promise for a future experimental realization of a more scalable magnetic trapping architecture.

# Chapter Seven

## Future Directions

In this final chapter, we discuss the next steps for the experiment. We discuss primarily theoretical directions towards which the experiment can progress.

### 7.1 Magnetic State Dressing

Holmium's very large magnetic moment makes it generally very sensitive to external fields, which makes it crucial to work in a regime where the gaps between energy levels do not change significantly if the magnetic field changes.

#### 7.1.1 Magic Field Conditions

To first order, at low fields the Zeeman effect causes an energy shift proportional to the projection of the total angular momentum,

$$\Delta U = \mu_B g_F m_F |B|$$

where  $\mu_B$  is the Bohr magneton,  $g_F$  is the Lande g-factor for that hyperfine level,  $m_F$  is the projection of the total angular momentum onto the magnetic field axis, and  $|B|$  is the magnitude of the magnetic field at the atom.

We can determine the energy levels of a quantum system by writing out the Hamiltonian of the system and then diagonalizing it, as the eigenvalues of a system's Hamiltonian correspond to its energy eigenstates. For holmium, the Hamiltonian consists of 128 on-

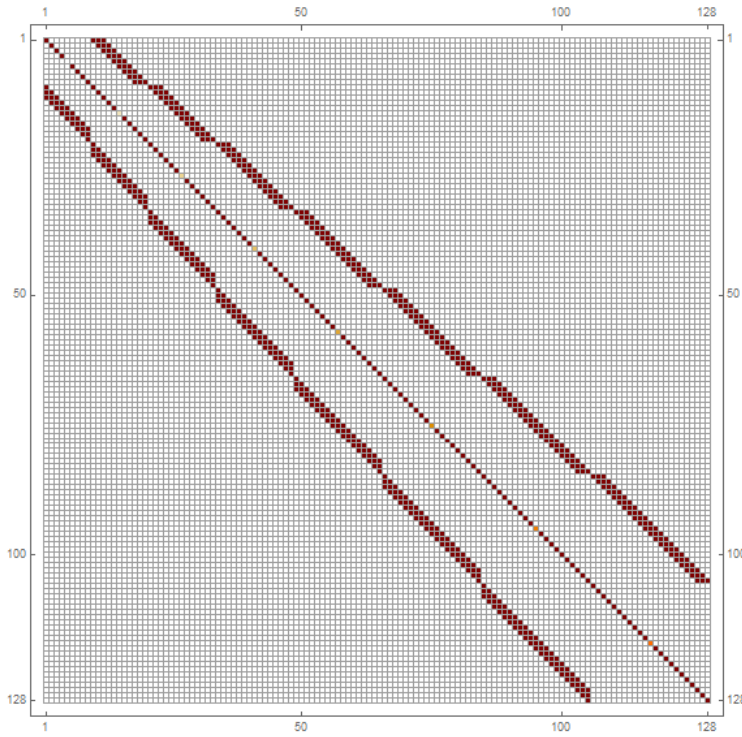


**Figure 7.1** Image showing the location of nonzero elements in the Zeeman Hamiltonian. The elements are very sparse, allowing the usage of more efficient sparse matrix diagonalization methods. This sparseness property still holds true for the Floquet matrix as well.

diagonal elements corresponding to the energy levels at zero external magnetic field and 252 off-diagonal elements from the Zeeman interaction.

Magic field conditions occur when the gap between two energy levels in an atomic system becomes insensitive to first order - that is, when  $\frac{dU}{dB} = 0$ . The magnitude of the magnetic field at which these occur are inherent to the atom itself, but can be influenced by external factors which affect the different states of the atom to different degrees. The approach we use here is by applying a microwave-frequency external field to the atoms, which causes coupling between different states and shifts their energies as a function of a static external magnetic field.

$B_{magic}$ (G)	$ F, m_F\rangle$	$ F', m'_F\rangle$	$\frac{dU}{dB}$ (MHz/G)	$\frac{d^2U}{dB^2}$ (MHz/G <sup>2</sup> )
231	$ 4, 1\rangle$	$ 5, 1\rangle$	2.03	6.27
319	$ 5, 5\rangle$	$ 6, 6\rangle$	10.4	14.4
408	$ 5, 1\rangle$	$ 6, 1\rangle$	1.92	8.75
454	$ 4, 2\rangle$	$ 5, 2\rangle$	4.10	13.6
646	$ 4, 4\rangle$	$ 5, 5\rangle$	9.68	4.71
662	$ 4, 3\rangle$	$ 5, 3\rangle$	6.27	6.69
698	$ 6, 1\rangle$	$ 7, 1\rangle$	2.00	9.93
802	$ 5, 2\rangle$	$ 6, 2\rangle$	3.88	11.3
845	$ 4, 4\rangle$	$ 5, 4\rangle$	8.63	5.42
1011	$ 5, 5\rangle$	$ 6, 5\rangle$	8.65	15.2
1140	$ 7, 1\rangle$	$ 8, 1\rangle$	2.26	19.9
1164	$ 5, 3\rangle$	$ 6, 3\rangle$	5.94	13.1
1180	$ 6, 6\rangle$	$ 7, 6\rangle$	8.99	5.75
1308	$ 6, 2\rangle$	$ 7, 2\rangle$	4.00	12.9
1348	$ 7, 7\rangle$	$ 8, 7\rangle$	9.52	7.87
1470	$ 5, 4\rangle$	$ 6, 4\rangle$	8.25	7.91

**Table 7.1** List of magic magnetic field conditions for states connected by single-photon transitions, up to 1500 Gauss. The sensitivity of the states at the magic field condition is also noted.

### 7.1.2 Approximation from Floquet Theory

Using microwaves to dress states in such a way to tune their magnetic field conditions is a well-known method and has been done before [65].

The term in the Hamiltonian for an external oscillating field is explicitly time-dependent

$$\hat{H} = 2\pi\sqrt{\frac{2\mu_0 I}{c}}\mu_B\langle F'm'_F|(g_I\hat{I} + g_J\hat{J})|Fm_F\rangle \cos(\omega t), \quad (7.1)$$

but the explicit time dependence is undesirable and generally harder to work with. Therefore, the general method is to get rid of the explicit time dependence in some way, and in most cases it is done using the Rotating Wave Approximation to simplify the Hamiltonian. For holmium though, we cannot use the RWA because the spread of energy gaps amongst all the hyperfine states means that the assumption that one term of the Hamiltonian is near resonance no longer holds true for all the states. To get rid of the explicit time-dependence, we used a method from Floquet Theory in order to approximate the behavior of dressing fields on the 128 Zeeman substates without using the RWA or other perturbative methods [66].

Floquet Theory is a branch of mathematics which examines solutions of linear differential equations of the form

$$\frac{dF(t)}{dt} = A(t) F(t),$$

where  $A(t)$  is a periodic function. In our case, all the functions involved are matrices with time-dependent entries.

Floquet's Theorem states that for these types of equations, a solution must exist of the form

$$F(t) = \Phi(t)e^{-iQt},$$

where  $\Phi(t)$  is a matrix of periodic functions and  $Q$  is a diagonal matrix. Floquet's Theorem effectively amounts to a coordinate transform into a coordinate system where the coordinates themselves are time-varying with the same periodicity as the function  $A(t)$ . We will show that the eigenvalues of  $Q$  are actually the eigenvalues we want to find.

We can rewrite  $A(t)$  in a similar manner to the time-evolution operator  $U(t; t_0)$ . We do this by viewing  $A(t')$  at any given  $t'$  as a transfer matrix from its state at some  $t = 0$  to  $t = t'$ :

$$U(t; t_0) = A(t)A^{-1}(t_0),$$

This allows us to relate  $A(t)$  to  $Q$ , given that the system is periodic with period  $T$ :

$$A(t + T) = A(t)e^{-iQT}.$$

On the other hand, we can still solve the Schrödinger Equation directly for the time-evolution operator

$$\det U(t_1; t_0) = \exp \left( -i \int_{t_0}^{t_1} \text{Tr}[\mathcal{H}(t)] dt \right),$$

which must have the same eigenvalues as they are just different ways of expressing the same operator. Equating these together and evaluating over one period from  $t = 0$  to  $t = T$ , we arrive at

$$\sum_{\alpha} q_{\alpha} = \frac{1}{T} \int_0^T \text{Tr}[\mathcal{H}(t)] dt$$

which tells us that  $Q$  does indeed represent a time-averaged Hamiltonian with the eigenvalues we are interested in.

To actually find  $Q$ , we express both the Hamiltonian and the Floquet solution  $F(t)$  in terms of their Fourier series,

$$F_{\alpha\beta}(t) = \sum_n F_{\alpha\beta^n} e^{in\omega t} e^{-iq_{\beta}t}$$

$$\mathcal{H}_{\alpha\beta} = \sum_n \mathcal{H}_{\alpha\beta^n} e^{in\omega t}$$

where  $\alpha$  represents matrix indices and  $\beta$  is an index for Fourier components. Then we substitute them back into the Schrödinger Equation, resulting in an eigenvalue equation for  $Q$ :

$$\sum_{\gamma\delta} (\mathcal{H}_{\alpha\gamma^{n-k}} + n\omega\delta_{\alpha\gamma}\delta_{kn}) F_{\alpha\beta^n} = q_{\beta} F_{\alpha\beta^n}$$

where  $\delta$  is the Kronecker delta.

Since Fourier series are infinite, this results in an eigenvalue problem for an infinite-dimensional matrix. All the additional states are an infinite sequence of virtual "copies" of

$$\begin{pmatrix} \cdot & \cdot & \cdot & \cdot & \cdot & \cdot \\ \cdot & \mathbf{H} - 2\mathbf{F} & \mathbf{C} & \mathbf{0} & \mathbf{0} & \mathbf{0} \\ \cdot & \mathbf{C} & \mathbf{H} - \mathbf{F} & \mathbf{C} & \mathbf{0} & \mathbf{0} \\ \cdot & \mathbf{0} & \mathbf{C} & \mathbf{H} & \mathbf{C} & \mathbf{0} \\ \cdot & \mathbf{0} & \mathbf{0} & \mathbf{C} & \mathbf{H} + \mathbf{F} & \mathbf{C} \\ \cdot & \mathbf{0} & \mathbf{0} & \mathbf{0} & \mathbf{C} & \mathbf{H} + 2\mathbf{F} \\ \cdot & \cdot & \cdot & \cdot & \cdot & \cdot \end{pmatrix} \quad \mathbf{F} = \begin{pmatrix} \cdot & \cdot & \cdot & \cdot \\ \cdot & \hbar\omega & \mathbf{0} & \mathbf{0} \\ \cdot & \mathbf{0} & \hbar\omega & \mathbf{0} \\ \cdot & \mathbf{0} & \mathbf{0} & \hbar\omega \\ \cdot & \cdot & \cdot & \cdot \end{pmatrix}$$

**Figure 7.2** Block matrix structure of the Floquet matrix to diagonalize.  $\mathbf{H}$  represents the 128x128 matrix for the hyperfine and Zeeman interactions and  $\mathbf{C}$  represents the off-diagonal microwave coupling Hamiltonian (Equation 7.1) but without the time dependent  $\cos(\omega t)$ .

the original 128 Zeeman states but separated by an energy equal to  $N$  microwave photons. In a similar vein to Feynman diagrams, the Floquet states corresponding to ever more photons interacting are essentially higher and higher order corrections to the main underlying interaction which occurs with only one photon. As a result, it is sufficient for numerical calculations to truncate the infinite matrix at a point which only contains 3-4 pairs of additional states and diagonalize the resulting finite matrix instead.

### 7.1.3 State Dressing Results

We have some preliminary results from the calculation which show the effects of state dressing on a particular set of states within the hyperfine manifold. In particular, we found that applying a dressing field detuned 30 MHz red of the  $F = 6$  to  $F = 7$  gap results in three sets of states which each have nearly the same magic field condition within each set, as seen in Figure 7.3. Furthermore each set of states have the magic conditions occurring between states which are connected by single-photon transitions, making them of potentially practical use as well.

These sets seem like promising candidates for qudits with three or four states at a first glance, and looking at the behavior of the magnetic field sensitivity of all four states near the magic field condition gives more insight into the states' behavior (see Figure 7.4). The derivative of the energy as a function of the magnetic field ( $dU/dB$ ) needs to be equal for two states for the magic field condition to hold, and we indeed observe three separate magic

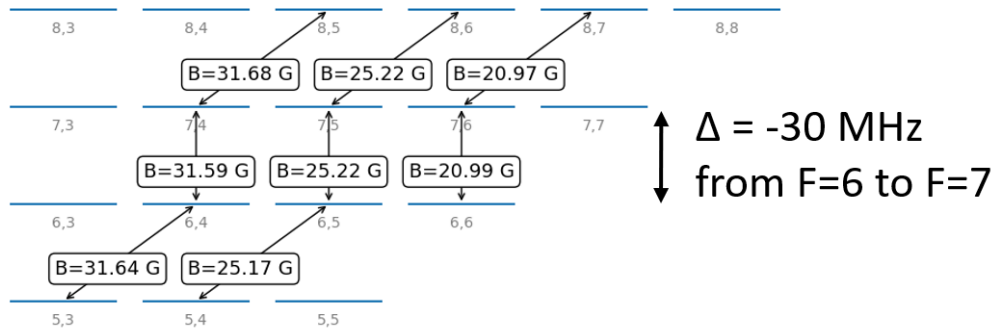


**Figure 7.3** Some states within holmium’s ground state which have the indicated magic field conditions between them when a dressing field detuned 30 MHz from the  $F = 6$  to  $F = 7$  gap is applied.

conditions occurring over this range at nearly the same field value. The underlying cause of the magic condition is due to the fact that two of the states undergo an avoided crossing, during which magic conditions with two other nearby states coincidentally happen. Similar behavior can be seen in the other two sets of states as well.

The presence of the avoided crossing means that the two states involved are strongly mixed in this range of fields. This strong mixing means that  $|F, m_F\rangle$  is a poor basis for the states, which is the basis we use for our qubit states, so using them for quantum information would require a careful change of basis. We plan to revisit these calculations at some point in the future when more progress towards an experimental realization is made. The code for the state dressing calculations was written in Python and is available at <https://github.com/cyip92/microwave-dressing> and <https://github.com/QuantumQuadrate/HolmiumCode>.

## 7.2 Qudits

While most experiments working on quantum information manipulate superpositions on pairs of quantum states, there is potential insight to be gained from working with more than two states at a time. As the qubit’s name derives from the *bit* being a unit of information which can be in one of two states, there are also quutrits (from the more obscure *trit*) which

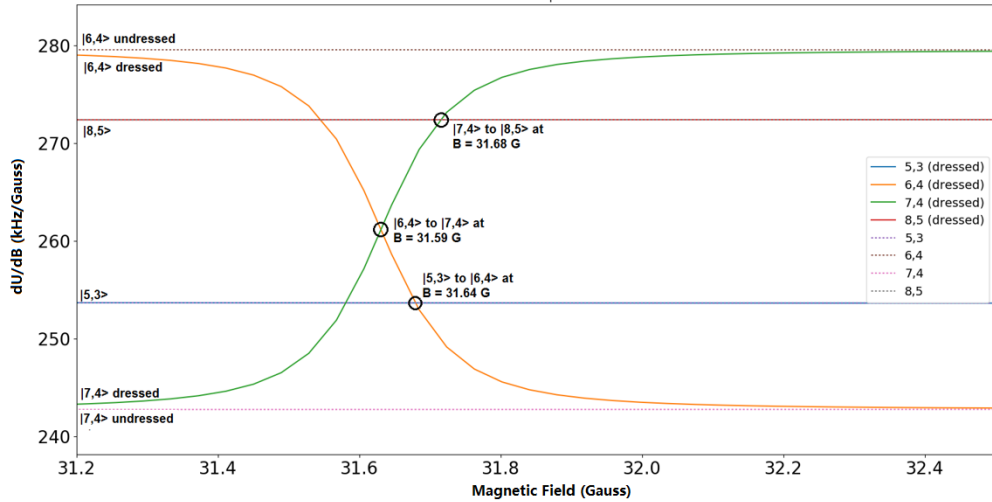


**Figure 7.4** Magnetic field sensitivities for states in one of the sets shown in 7.3.  $|6,4\rangle$  and  $|7,4\rangle$  have an avoided crossing which causes the presence of the magic conditions in the first place, but the avoided crossing means these magic conditions are not useful for quantum information.

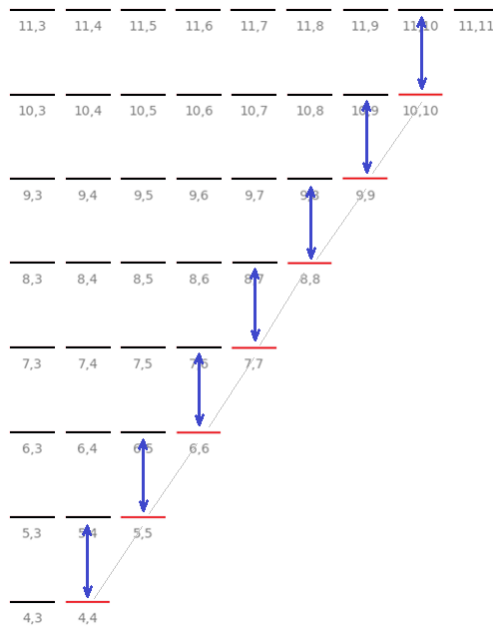


**Figure 7.5** 7-state qudit within holmium's hyperfine states, showing the positioning of the states (red) with arrows (blue) showing transitions which could be used for state dressing in a way that lets us independently tune out each state's magnetic sensitivity.

describe superpositions amongst three orthogonal states and - more generally - *qudits* for  $d$  orthogonal quantum states.

As holmium has such a large number of Zeeman substates, it is a good testbed for potential qudit experiments. Additionally, the aforementioned state dressing procedure would allow for multiple different states to be individually dressed such that all of the qudit states satisfy the same magic field condition simultaneously.

One potentially attractive option is a 7-state qudit using the all of the stretched states of  $|F, m_F\rangle = \{|4, 4\rangle, |5, 5\rangle, \dots, |10, 10\rangle\}$ , where the uppermost  $|11, 11\rangle$  state would be used as a readout state for the qudit. The fact that all the spacings between the hyperfine levels are different opens up the possibility to individually dress any particular qudit state to be magnetically insensitive while having a negligible effect on the others.

### 7.3 Conclusion

In this chapter we have examined the necessary calculations for future steps of the experiment, which require more involved approaches due to holmium's complex electronic structure.

# Chapter Eight

## Concluding Statements

In this thesis we continue the progress made towards quantum information processing with collective holmium ensembles. Cooling and trapping holmium in a MOT was previously shown, but we have now also demonstrated the first optical dipole trap of holmium. The production of a successful dipole trap opens up many possibilities for future work on studying holmium's atomic properties.

As a necessary step to make our atoms colder, we also performed some measurements on a largely previously unstudied transition which we would use for second-stage cooling in our MOT. The values for the hyperfine constants of this particular excited state improve on the uncertainty in previous literature by approximately a factor of 20, and are an important step towards an experimental implementation of narrow line cooling in holmium using this transition.

We have also made significant progress towards measuring single holmium atoms, the first step towards performing qubit operations. Additionally, we have performed some calculations which further suggest holmium's usefulness for alternate approaches to quantum information which take advantage of its complex energy level structure and high magnetic moment.

There still remains lots of research to be done on holmium, but its complicated atomic structure and large hyperfine manifold holds lots of promise for future work.

# REFERENCES

- [1] T. Ladd, F. Jelezko, R. Laflamme, Y. Nakamura, C. Monroe, and J. O'Brien. "Quantum computers". In: *Nature Phys.* 464 (2010), pp. 45–53.
- [2] P. Kok, W. Munro, K. Nemoto, T. Ralph, J. Dowling, and G. Milburn. "Linear optical quantum computing with photonic qubits". In: *Rev. Mod. Phys.* 79.135 (2007).
- [3] H. Haffner, C. Roos, and R. Blatt. "Quantum computing with trapped ions". In: *Phys. Rep.* 469.4 (2008).
- [4] D. Loss and D. DiVincenzo. "Quantum computation with quantum dots". In: *Phys. Rev. A* 57.1 (1998).
- [5] J. Clarke and F. K. Wilhelm. "Superconducting quantum bits". In: *Nature Phys.* 453 (2008), pp. 1031–1042.
- [6] J. Weber, W. Koehl, J. Varley, A. Janotti, B. Buckley, C. V. de Walle, and D. Awschalom. "Quantum computing with defects". In: *Proc. Natl. Acad. Sci. USA* 107.19 (2010), pp. 8513–8518.
- [7] M. Saffman, T. G. Walker, and K. Mølmer. "Quantum information with Rydberg atoms". In: *Rev. Mod. Phys.* 82 (2010), pp. 2313–2363.
- [8] J. D. Pritchard, J. A. Isaacs, M. A. Beck, R. McDermott, and M. Saffman. "Hybrid Atom–Photon Quantum Gate in a Superconducting Microwave Resonator". In: *Phys. Rev. A* 89.010301 (2014).
- [9] D. Jaksch, J. I. Cirac, P. Zoller, S. L. Rolston, R. Cote, and M. D. Lukin. "Fast quantum gates for neutral atoms". In: *Phys. Rev. Lett.* 85 (2000), pp. 2208–2211.
- [10] D. Yavuz, P. Kulatunga, E. Urban, T. Johnson, N. Proite, T. Henage, T. Walker, and M. Saffman. "Fast ground state manipulation of neutral atoms in microscopic optical traps". In: *Phys. Rev. Lett.* 96 (2006), p. 063001.
- [11] L. Isenhower, E. Urban, X. Zhang, A. Gill, T. Henage, T. Johnson, T. Walker, and M. Saffman. "Demonstration of a neutral atom controlled-not quantum gate". In: *Phys. Rev. Lett.* 104 (2010), p. 010503.
- [12] X. Zhang, L. Isenhower, A. Gill, T. Walker, and M. Saffman. "Deterministic entanglement of two neutral atoms via Rydberg blockade". In: *Phys. Rev. A* 82 (2010), p. 030306.

- [13] K. Maller, M. Lichtman, T. Xia, Y. Sun, M. Piotrowicz, A. Carr, L. Isenhower, and M. Saffman. “Rydberg-blockade controlled-not gate and entanglement in a two-dimensional array of neutral-atom qubits”. In: *Phys. Rev. A* 92 (2015), p. 022336.
- [14] K. Nelson, X. Li, and D. Weiss. “Imaging single atoms in a three-dimensional array”. In: *Nature Phys.* 3 (2007), pp. 556–560.
- [15] M. Saffman and K. Mølmer. “Scaling the neutral-atom rydberg gate quantum computer by collective encoding in holmium atoms”. In: *Phys. Rev. A* 78.012336 (2008).
- [16] M. D. Lukin, M. Fleischhauer, R. Cote, L. M. Duan, D. Jaksch, J. I. Cirac, and P. Zoller. “Dipole blockade and quantum information processing in mesoscopic atomic ensembles”. In: *Phys. Rev. Lett.* 87 (June 2001), p. 037901.
- [17] S. Kim, R. R. Mcleod, M. Saffman, and K. H. Wagner. “Doppler-free, multi-wavelength acousto-optic deflector for two-photon addressing arrays of Rb atoms in a quantum information processor”. In: *Appl. Opt.* 47 (2008), p. 1816.
- [18] J. A. Miles, Z. J. Simmons, and D. D. Yavuz. “Subwavelength Localization of Atomic Excitation Using Electromagnetically Induced Transparency”. In: *Phys. Rev. X* 3 (2013), p. 031014.
- [19] D. Schrader, I. Dotsenko, M. Khudaverdyan, Y. Miroshnychenko, A. Rauschenbeutel, and D. Meschede. “Neutral Atom Quantum Register”. In: *Phys. Rev. Lett.* 93 (2004), p. 150501.
- [20] T. Xia, M. Lichtman, K. Maller, A. W. Carr, M. J. Piotrowicz, L. Isenhower, and M. Saffman. “Randomized Benchmarking of Single-Qubit Gates in a 2D Array of Neutral-Atom Qubits”. In: *Phys. Rev. Lett.* 114 (2015), p. 100503.
- [21] W. Dür, G. Vidal, and J. I. Cirac. “Three qubits can be entangled in two inequivalent ways”. In: *Phys. Rev. A* 62 (2000), p. 062314.
- [22] E. L. Raab, M. Prentiss, A. Cable, S. Chu, and D. E. Pritchard. “Trapping of neutral sodium atoms with radiation pressure”. In: *Phys. Rev. Lett.* 59 (1987), pp. 2631–2634.
- [23] K. Honda, Y. Takahashi, T. Kuwamoto, M. Fujimoto, K. Toyoda, K. Ishikawa, and T. Yabuzaki. “Magneto-optical trapping of yb atoms and a limit on the branching ratio of the  $^1P_1$  state”. In: *Phys. Rev. A* 59 (1999), R934–R937.
- [24] J. J. McClelland and J. L. Hanssen. “Laser cooling without repumping: A magneto-optical trap for erbium atoms”. In: *Phys. Rev. Lett.* 96.143005 (2006).
- [25] M. Lu, S. H. Youn, and B. L. Lev. “Trapping ultracold dysprosium: A highly magnetic gas for dipolar physics”. In: *Phys. Rev. Lett.* 104 (2010), p. 063001.
- [26] D. Sukachev, A. Sokolov, K. Chebakov, A. Akimov, S. Kanorsky, N. Kolachevsky, and V. Sorokin. “Magneto-optical trap for thulium atoms”. In: *Phys. Rev. A* 82 (2010), p. 011405.
- [27] J. Miao, J. Hostetter, G. Stratis, and M. Saffman. “Magneto-optical trapping of holmium atoms”. In: *Phys. Rev. A* 89.041401 (2014).

- [28] K. Aikawa, A. Frisch, M. Mark, S. Baier, A. Rietzler, R. Grimm, and F. Ferlaino. “Bose-Einstein Condensation of Erbium”. In: *Phys. Rev. Lett.* 108 (2012), p. 210401.
- [29] Svetlana Kotochigova and Alexander Petrov. “Anisotropy in the interaction of ultracold dysprosium”. In: *Phys. Chem. Chem. Phys.* 13 (2011), pp. 19165–19170.
- [30] R. Maruyama. “Optical Trapping of Ytterbium Atoms”. PhD thesis. University of Washington, May 2003.
- [31] N.N. Kolachevsky and K.Yu. Khabarova. “Precision laser spectroscopy in fundamental studies”. In: *Phys. Usp.* 57 (2014), pp. 1230–1238.
- [32] G. Nave. “Atomic transition rates for neutral holmium (Ho I)”. In: *J. Opt. Soc. Am. B* 20 (2003), pp. 2193–2202.
- [33] G. F. Wakefield, A. H. Daane, and F. Spedding. “Vapor pressure of holmium”. In: *Journal of Chemical Physics* 47.12 (1967), pp. 4994–4999.
- [34] J. Hostetter. “Laser cooling, Trapping, and Rydberg Spectroscopy of Neutral Holmium Atoms”. PhD thesis. University of Wisconsin-Madison, May 2016.
- [35] K. Liu and M. G. Littman. “Novel geometry for single-mode scanning of tunable lasers”. In: *Opt. Lett.* 6 (1981), pp. 117–118.
- [36] T.W. Hansch and B.Couillaud. “Laser frequency stabilization by polarization spectroscopy of a reflecting reference cavity”. In: *Opt. Comm.* 35 (1980), pp. 441–444.
- [37] J. Miao. “Laser cooling and Magneto-Optical Trapping of Holmium Atoms”. PhD thesis. University of Wisconsin-Madison, Aug. 2013.
- [38] Arroyo. *TECSource 5240 User’s Manual*. 2. 2011.
- [39] J.D. Pritchard, J.A. Isaacs, and M. Saffman. “Long working distance objective lenses for single atom trapping and imaging”. In: *Rev. Sci. Instrum.* 87.073107 (2016).
- [40] M. Lichtman. “Coherent Operations, Entanglement, and Progress Toward Quantum Search in a Large 2D Array of Neutral Atom Qubits”. PhD thesis. University of Wisconsin-Madison, Aug. 2015.
- [41] National Instruments. *User Manual: NI-2163B*, 11. 2007.
- [42] National Instruments. *BNC2090A User Manual*. 1. 2007.
- [43] Analog Devices. *AD9910 Datasheet*. 2007.
- [44] Zhonghua Ji, Jinpeng Yuan, Yanting Zhao, Xuefang Chang, Yonggang Yang, Liantuan Xiao, and Suotang Jia. “Optimization and analysis of experimental parameters for polarization gradient cooling in optical molasses”. In: *Chin. Phys. B* 23 (2014), p. 113702.
- [45] R. Grimm, M. Weidemüller, and Y. B. Ovchinnikov. “Optical Dipole Traps for Neutral Atoms”. In: *Advances in Atomic, Molecular, and Optical Physics* (2000), pp. 95–170.
- [46] L. Isenhower, W. Williams, A. Dally, and M. Saffman. “Atom trapping in an interferometrically generated bottle beam trap”. In: *Opt. Lett.* 34 (2009), p. 1159.
- [47] G. Li, S. Zhang, L. Isenhower, K. Maller, and M. Saffman. “A crossed vortex bottle beam trap for single-atom qubits”. In: *Opt. Lett.* 37 (2012), p. 851.

- [48] T. A. Savard, K. M. O'Hara, and J. E. Thomas. "Laser-noise-induced heating in far-off resonance optical traps". In: *Phys. Rev. A* 56.2 (1997).
- [49] S. Baier. "An optical dipole trap for Erbium with tunable geometry". MA thesis. University of Innsbruck, Oct. 2012.
- [50] J. Dalibard and C. Cohen-Tannoudji. "Laser cooling below the doppler limit by polarization gradients: simple theoretical models". In: *J. Opt. Soc. Am. B* 6 (Nov. 1989), pp. 2023–2045.
- [51] D. Sesko, T. Walker, C. Monroe, A. Gallagher, and C. Wieman. "Collisional Losses from a Light-Force Atom Trap". In: *Phys. Rev. Lett.* 63 (1989), pp. 961–964.
- [52] S. Kröger, J.-F. Wyart, and P. Luc. "Theoretical Interpretation of Hyperfine Structures in Doubly-Excited Configurations  $4f^{10}5d6s6p$  and  $4f^{10}5d^26s$  and New Energy Levels in Neutral Holmium (Ho I)". In: *Physica Scripta*. 5 (1997), pp. 579–585.
- [53] E. A. Den Hartog, L. M. Wiese, and J. E. Lawler. "Radiative lifetimes of Ho I and Ho II". In: *J. Opt. Soc. Am. B*. 16 (1999), pp. 2278–2284.
- [54] B. Burghardt, S. Büttgenbach, N. Glaeser, R. Harzer, G. Meisel, B. Roski, and F. Träber. "Hyperfine structure measurements in metastable states of  $^{165}\text{Ho}$ ". In: *Z. Phys. A*. 307 (1982).
- [55] Daryl W. Preston. "Doppler-free saturated absorption: Laser spectroscopy". In: *American Journal of Physics* 64 (1996), pp. 1432–1436.
- [56] A. Frisch, K. Aikawa, M. Mark, A. Rietzler, J. Schindler, E. Zupanic amd R. Grimm, and F. Ferlaino. "Narrow-line magneto-optical trap for erbium". In: *Phys. Rev. A* 85.051401 (2012).
- [57] A. J. Berglund, J. L. Hanssen, and J. J. McClelland. "Narrow-line magneto-optical cooling and trapping of strongly magnetic atoms". In: *Phys. Rev. Lett.* 100.113002 (2008).
- [58] D. J. Massey, J. P. R. David, and G. J. Rees. "Temperature Dependence of Impact Ionization in Submicrometer Silicon Devices". In: *IEEE Trans. on Elec. Devices* 53 (2006), p. 9.
- [59] Hamamatsu. *EM-CCD Technical Note*. 2009.
- [60] Princeton Instruments. *ProEM+ System Manual*. 2013.
- [61] Z. Hu and H. J. Kimble. "Observation of a single atom in a magneto-optical trap". In: *Opt. Lett.* 19 (1994), p. 1888.
- [62] S. Earnshaw. "On the nature of the molecular forces which regulate the constitution of the luminiferous ether". In: *Trans. Camb. Phil. Soc.* 7 (1842), pp. 97–114.
- [63] D. M. Brink and C. V. Sukumar. "Majorana spin-flip transitions in a magnetic trap". In: *Phys. Rev. A* 74.035401 (2006).
- [64] Applied Thin-Film Products. *Safe Current Limits in Thin-Film Gold and Copper*. 2019. URL: <https://www.thinfilm.com/limits.html> (visited on 01/11/2020).

- [65] L. Sárkány, P. Weiss, H. Hattermann, and J. Fortágh. “Controlling the magnetic-field sensitivity of atomic-clock states by microwave dressing”. In: *Phys. Rev. A.* 90.053416 (2014).
- [66] A. Chakraborty and S. R. Mishra. “A Floquet formalism for the interaction of magnetically trapped atoms with rf-fields”. In: *J. Phys. B: At. Mol. Opt.* 51 (2018), p. 025002.
- [67] R. W. P. Drever, J. L. Hall, F. V. Kowalski, J. Hough, G. M. Ford, A. J. Munley, and H. Ward. “Laser Phase and Frequency Stabilization Using an Optical Resonator”. In: *Applied Physics B* 31 (1983), pp. 97–105.
- [68] J. I. Thorpe, K. Numata, and J. Livas. “Laser frequency stabilization and control through offset sideband locking to optical cavities”. In: *Optics Express* 16.20 (2008), pp. 15980–15990.

## Appendix A

# Aligning optics for combined trapping and imaging

Ensuring the focal plane for the imaging path and the dipole trap beams is important but also nontrivial, as the two beams need to follow the same path, but have wavelengths which differ to a significant enough degree (410.5 nm and 532 nm, respectively) that chromatic aberration is a potential problem. The alignment process was as follows:

1. Mount a cage rod end plate approximately where the trap is expected to be, relative to the imaging optics, in a way that allows free translation on all axes. Clamp down imaging setup on to the table so it cannot move freely.
2. Install an iris onto the cage rod system which allows rough alignment along the axis of the cage rods. The purpose of this iris is to establish a very coarse alignment.
3. Illuminate the from behind with a broadband light source such as a lamp and move the iris around until an edge is found and brought into focus. Iteratively close the iris and move it around so that it remains in focus and centered on the camera. The bandpass filters may need to be removed at this point.
4. Once the iris is closed to the smallest size it can be, make a note of its position on the cage mount system. Reinstall the bandpass filters if they had to be removed in the previous step.
5. Direct a collimated beam of 410.5 nm light through the cage rod system and ensure that the beam is approximately centered on both the cage rod system for the iris and on the cage rod system for the imaging path.

6. Mount a  $10 \mu m$  pinhole at roughly the same spot where the iris was and illuminate it from the back with the 410.5 nm light. This is effectively using the pinhole to simulate the trap as a point source of light with minimal aberration due to the previous steps.
7. Make fine adjustments to the pinhole positioning to bring a backlit image of it into focus on the camera. This should produce a much sharper image than the iris due to the lack of chromatic aberration. At this point, the optics along the imaging path are aligned and should not be touched.
8. Set the trap laser to the lowest available power to minimize scatter during alignment, as the eye is highly sensitive to 532 nm. Use optics before the dichroic to align the trap light through the pinhole, using the path of the 410.5 nm light as a guide after the pinhole. The goal is to get the two beams roughly counter-propagating.
9. Block the 410.5 nm light and place a power meter on the far end of the pinhole. Finely adjust the focus of the fiber launcher for the trap light to maximize the reading on the power meter. This is a deliberate minor defocusing in order to compensate for chromatic aberration along the combined beam path in order to bring their focal planes together.

At low trap power, we had  $800 \mu W$  of trap light going into the pinhole and  $540 \mu W$  through the other side; a 68% transmission corresponding to an ideal Gaussian beam waist (radius) of  $6.6 \mu m$ .

## Appendix B

### Locking to a ULE Sideband

Our method of stabilizing our laser is based on the Pound-Drever-Hall method [67]. However, since the ULE cavity we are using has transmission peaks which cannot be tuned, we use a method which slightly modifies the PDH locking scheme that allows locking to a tunable frequency sideband relative to the ULE peak [68].

In a normal PDH locking scheme, an error signal is produced via the reflected light from the reference cavity. Simply using the reflected intensity on its own is not enough, as that would only produce a dip where the transmission through the cavity is maximized. This is undesirable because there is no way to distinguish between being below resonance or being above resonance.

Instead, the PDH error signal is generated by phase-modulating the beam incident on the cavity at some modulation frequency  $\omega_1$ . Representing the unmodulated electric field as  $E = E_0 e^{i\omega_0 t}$ , a series expansion shows that this modulation effectively adds sidebands to the electric field at frequencies of  $\omega = \omega_0 \pm \omega_1$ :

$$E = E_0 e^{i(\omega_0 t + \beta \sin(\omega_1 t))} \approx E_0 e^{i\omega_0 t} [1 + i\beta \sin(\omega_1 t)] = E_0 e^{i\omega_0 t} \left[ 1 + \frac{\beta}{2} e^{i\omega_1 t} - \frac{\beta}{2} e^{-i\omega_1 t} \right].$$

When this electric field is incident on an optical resonator, the reflected power  $P = E_r * E_r$  becomes a sum of terms which has oscillating components at DC,  $\omega_1$ , and  $2\omega_1$ . We can use a RF mixer to select out just the component at the modulation frequency at  $\omega_1$ . This produces a DC voltage which has odd symmetry as a function of  $\Delta\omega = \omega - \omega_1$ , which is then used as the PDH error signal.

The sideband locking uses the same principle, but in addition to modulating at  $\omega_1$  (the PDH sideband frequency), we also modulate at another frequency  $\omega_2$  (the tunable scanning frequency). Both RF frequencies are combined with a power combiner in order to produce

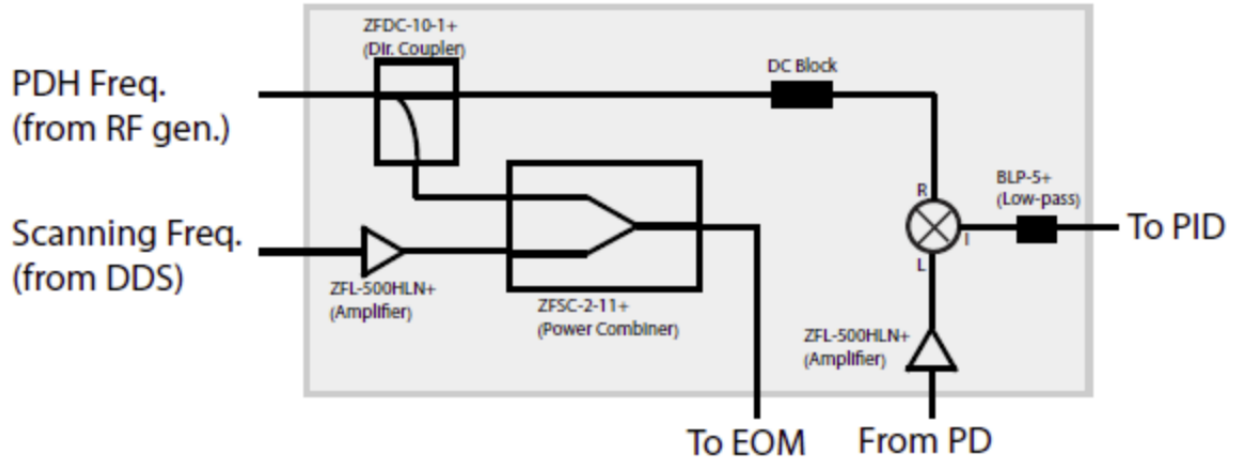


**Figure B.1** Schematic for the RF electronics we used for the ULE sideband lock

independent modulation at the two frequencies. This results in sidebands at  $\omega_0 + \omega_1 \pm \omega_2$  and  $\omega_0 - \omega_1 \pm \omega_2$ . Demodulating using the combined RF frequencies allows the error signal to be pulled out of the highly modulated signal, provided that all the resultant sidebands are sufficiently separated in frequency space.

## Appendix C

# Atom Temperature Measurements

In order to measure how hot our atoms are in our traps, we use a ballistic time-of-flight measurement. This involves forming a MOT, then simply turning off the beams and gradient field and watching how the density of the MOT evolves over time as the cloud expands purely from thermal motion. We start by assuming that the velocity of the atoms follows a typical Maxwell-Boltzmann distribution, the MOT has a Gaussian density profile as a function of distance from the center, and that position and momentum are uncorrelated. This gives us an initial distribution function:

$$f(r, p) = \left( N \left( \frac{2}{\pi w_0^2} \right)^{3/2} e^{-2r^2/w_0^2} \right) \cdot \left( \frac{1}{(2\pi m k_B T)^{3/2}} e^{-p^2/(2m k_B T)} \right)$$

where  $w_0$  is the initial radius of the MOT,  $m$  is the atomic mass,  $k_B$  is the Boltzmann constant, and  $T$  is the kinetic temperature of the atoms. When we turn off the MOT beams and gradient field, the potential keeping the atoms in place vanishes. If we assume that the momentum stays constant ( $p(t) = p(0) \equiv p$ ) and that the the trajectories are constant-velocity ( $r(t) = r(0) + pt/m$ ), then we can integrate the momentum out by evaluating  $f(r) = \int f(r, p) d^3p$  to get the following position distribution function:

$$f(r) = N \left( \frac{2m}{\pi(4k_B T t^2 + mw_0^2)} \right)^{3/2} e^{2mr_0^2/(4k_B T t^2 + mw_0^2)}$$

From this expression, we can draw out an effective width as a function of time,

$$w(t) = w_0 \sqrt{1 + 4k_B T t^2 / (mw_0^2)} \tag{C.1}$$

which can then be used as a fitting function for time-series images for a slowly expanding MOT in order to measure the atom temperature. This width corresponds to the typical  $1/e^2$

width by which all Gaussian functions are characterized, which is also related to simpler-to-measure "full width at half maximum" by a multiplicative constant.

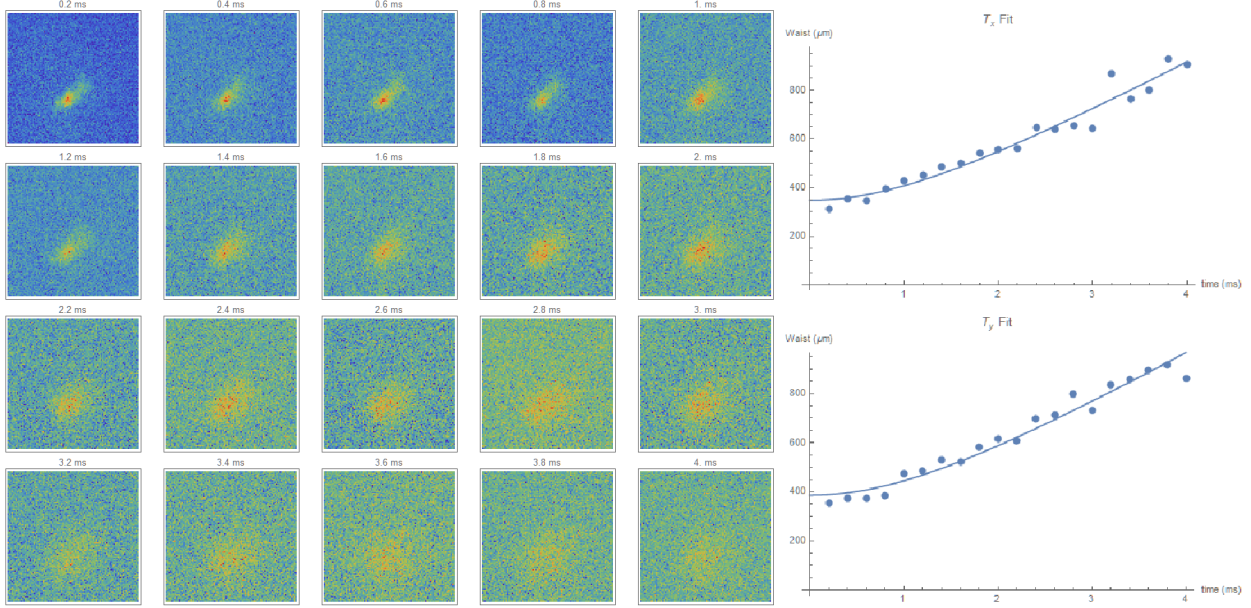


**Figure C.1** Sample data for a MOT temperature measurement, showing images of the MOT expanding over time and curves corresponding to fitted widths on the two different horizontal axes. This particular dataset corresponds to a kinetic temperature of roughly  $230 \mu\text{K}$ . In our experiment these values are typically approximately the same, although in other rare earths the temperature has sometimes been observed to be highly anisotropic [25].

For our dipole trap, this method does not work as well due to our limited field of view and dim signal due to having significantly less atoms. Instead, we perform a drop-and-recapture procedure where we turn off the trap for a few microseconds before turning it back on. We can reuse the above result for the behavior of the atoms as they expand ballistically when the trapping potential is removed.

The key difference for the drop-recapture analysis is that we do not let the atom cloud expand indefinitely and measure its width. Instead, we turn the trap back on and measure the atom population which falls back into the trapping volume. We can approach this theoretically by examining an overlap integral between  $\sqrt{f(r, t = 0)}$  and  $\sqrt{f(r, t = t')}$ , where for the sake of simplifying we suppose that  $w(t') = aw(0) \equiv aw_0$ . Calculating the population

recaptured in the trap as an overlap integral out to infinity in this way allows for a closed-form solution with elementary functions:

$$N \int_{-\infty}^{\infty} \left( \frac{2}{\pi w_0^2} \right)^{3/4} e^{-r^2/w_0^2} \cdot \left( \frac{2}{\pi(a w_0)^2} \right)^{3/4} e^{-r^2/(a w_0)^2} 2\pi r^2 dr = N \left( \frac{2a}{a^2 + 1} \right)^{3/2}$$

Then, from Eq. C.1, we can see that there is a characteristic time scale for the expansion. We can rescale the time variable as  $\tilde{t} = t/\sqrt{mw_0^2/(4k_B T)}$  and then substitute  $a = \sqrt{1 + \tilde{t}^2}$  to produce a formula for the recapture population as a function of the drop time:

$$N(\tilde{t}) = \left( \frac{2\sqrt{\tilde{t}^2 + 1}}{\tilde{t}^2 + 2} \right)^{3/2}$$

This can be fitted to a curve produced by experimental data, and the atom temperature can be inferred based on the value of  $\tilde{t}$  which produces the best least-squares error fit.

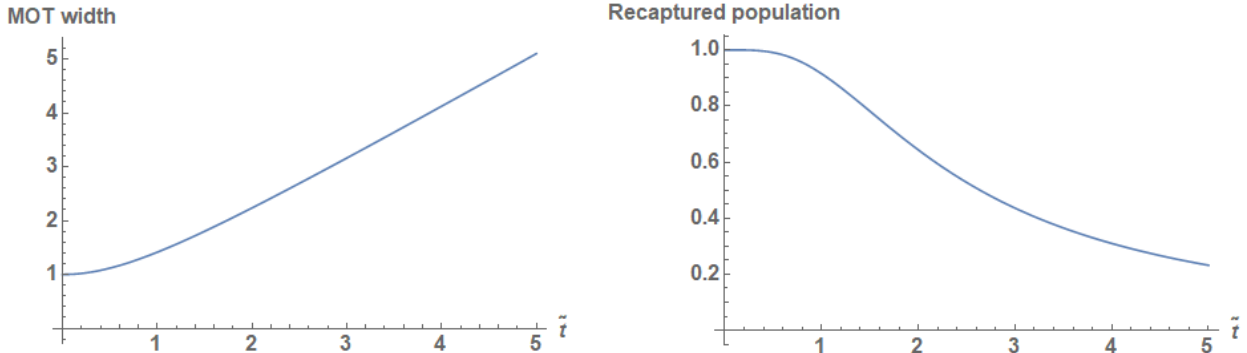


**Figure C.2** MOT expansion and drop-recapture population curves as a function of the scaled time  $\tilde{t} = t/\sqrt{mw_0^2/(4k_B T)}$ . The MOT width during free expansion asymptotically approaches a linear time-dependence, but the recapture curve does not have simple asymptotic behavior.

## Appendix D

# Narrow-line Frequency References

Atomic physics often necessitates very precise measurements of many different forms. In our case, we need to characterize our narrow-line transition by making measurements on the scale of a few MHz, which is already one part in  $\approx 10^8$  compared to the hundreds of THz of the transition itself. While other experiments in the field of AMO require precision of a few more orders of magnitude on top of this, it is still a fairly stringent requirement which requires some care.

Luckily in our case we only need precise *relative* frequencies, and absolute frequency measurements are unnecessary. This simplifies our requirements for our frequency reference significantly. With the same configuration as above, we produce sidebands on the transmission of the ULE cavity which can be tuned to appear at differing frequencies relative to the fundamental ULE transmission peaks.

As noted in section 2.5.1, the ULE cavity has an absolute frequency stability of 14.5 kHz based on its temperature control. While the absolute frequency is unimportant, its stability tells us whether or not we need to be concerned with frequency drifts over time. In this case, any frequency drift due to the cavity itself is a couple orders of magnitude smaller than the quantities we are trying to measure, which is more than sufficient for our applications.

Given a properly referenced RF source, we can use a transmission peak on the ULE cavity as an indicator for a certain frequency. Then, by changing the output frequency of this RF source and keeping everything else the same, we can produce nominally identical data but with a different frequency marked by the ULE transmission peak being in a different location.

Multiple data sets with these frequency markers, when taken together, allow us to translate the data from absorption as a function of laser ramp voltage into absorption as a function

of actual laser frequency. This is important for multiple reasons as the voltage ramp is both unstable and slightly nonlinear over larger ranges and given our equipment setup, is largely controlled in an analog manner.

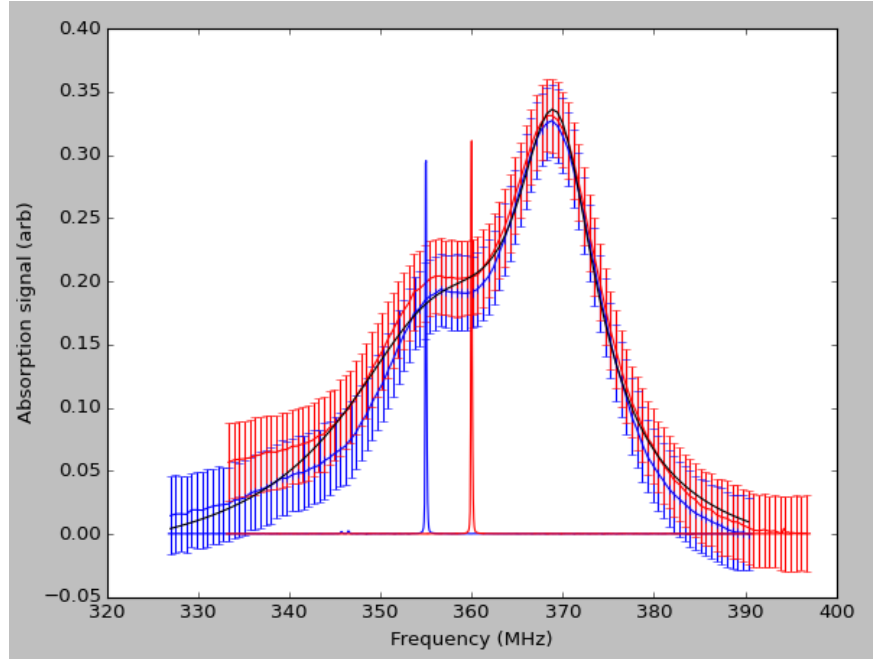


**Figure D.1** Sample data demonstrating how data sets are combined together. The two data sets with error bars are the saturated absorption transmission peaks for the two nearly-degenerate peaks taken under identical conditions. Each individual data set consisted of approximately 50000 raw data points; the error bars indicate the standard deviation of sets of 500 consecutive points being binned together. The sharper peaks are the transmission peaks of the ULE cavity. The two data sets were taken with the ULE sideband tuned to 355 MHz and 360 MHz, which allows the horizontal axis to be properly scaled for the spectroscopy data.

We assume that the relationship between ramp voltage and laser frequency is approximately linear in the middle of the range, which is a reasonable approximation for our setup as the main nonlinear behavior occurs near the turning points of the ramp. For the same reason, the ULE reference peaks were positioned to both be very near to the spectroscopy peaks themselves.